

8-2018

Identification of Intracranial Lesions with Dual-Energy Computed Tomography and Magnetic Resonance Phase Imaging

Megan C. Jacobsen

Follow this and additional works at: https://digitalcommons.library.tmc.edu/utgsbs_dissertations



Part of the [Medicine and Health Sciences Commons](#), and the [Other Physics Commons](#)

Recommended Citation

Jacobsen, Megan C., "Identification of Intracranial Lesions with Dual-Energy Computed Tomography and Magnetic Resonance Phase Imaging" (2018). *The University of Texas MD Anderson Cancer Center UTHealth Graduate School of Biomedical Sciences Dissertations and Theses (Open Access)*. 881.
https://digitalcommons.library.tmc.edu/utgsbs_dissertations/881

This Dissertation (PhD) is brought to you for free and open access by the The University of Texas MD Anderson Cancer Center UTHealth Graduate School of Biomedical Sciences at DigitalCommons@TMC. It has been accepted for inclusion in The University of Texas MD Anderson Cancer Center UTHealth Graduate School of Biomedical Sciences Dissertations and Theses (Open Access) by an authorized administrator of DigitalCommons@TMC. For more information, please contact digitalcommons@library.tmc.edu.

IDENTIFICATION OF INTRACRANIAL LESIONS WITH DUAL-ENERGY COMPUTED
TOMOGRAPHY AND MAGNETIC RESONANCE PHASE IMAGING

by

Megan C. Jacobsen, B.A.

APPROVED:

Dianna Cody, Ph.D.
Advisory Professor

Dawid Schellingerhout, M.D.
Secondary Mentor

Ken-Pin Hwang, Ph.D.

Lucia LeRoux, Ph.D.

Xinming Liu, Ph.D.

Veera Baladandayuthapani, Ph.D.

APPROVED:

Dean, The University of Texas MD Anderson Cancer Center UTHealth
Graduate School of Biomedical Sciences

IDENTIFICATION OF INTRACRANIAL LESIONS WITH DUAL-ENERGY COMPUTED
TOMOGRAPHY AND MAGNETIC RESONANCE PHASE IMAGING

A

DISSERTATION

Presented to the Faculty of

The University of Texas MD Anderson Cancer Center UTHealth

Graduate School of Biomedical Sciences

in Partial Fulfillment

of the Requirements

for the Degree of

DOCTOR OF PHILOSOPHY

by

Megan C. Jacobsen, B.A.

Houston, Texas

August 2018

Acknowledgements

This work would not have been possible without the guidance of my advisors, Dianna Cody and Dawid Schellingerhout. They have spent a significant amount of time and effort guiding my research over the past six years and have been there to impart their knowledge to me through the highs and lows of research. I would also like to thank the rest of my advisory committee for their input throughout my doctoral research. Ken-Pin Hwang has attended nearly every lab meeting since we began developing our trial and has painstakingly guided me through the world of MRI for several years without complaint. Lucia Le Roux has served as a personal mentor who has always taken the time to talk with me about life, agarose gel phantoms, and managed to teach this laboratory-deficient physicist how to use a pipette. I would like to thank Xinming Liu for supporting various CT projects throughout the course of my doctoral work, and Veera Baladandayuthapani for providing input on statistical matters great and small. Thank you all for serving on my committee for the past five years.

I would like to thank all of the additional MD Anderson staff that have made this research feasible, including Kathy Prentice, the staff of the Center for Advanced Biomedical Imaging, the Medical Imaging Technologist team, and the research nurses from Diagnostic Imaging. Michelle, Riya, Cynthia, and Jerica have contacted every one of our patients and met with them one-on-one. Wolfgang Stefan developed fantastic software to enable myself and Dr. Schellingerhout to easily screen patients.

Finally, I would like to thank my support network both at home and at work. My partner, Justin Chen, has been with me through thick and thin for over five years. My parents and sisters have supported this venture from day one. Jessica Nute, my former lab mate, taught me how to use a CT scanner, guided me through the early years of my PhD, and has been an amazing friend and mentor. I would also like to acknowledge my former officemates, Chris MacLellan and Sam Fahrenholtz, for their comradery. Finally, thank you to Cayla Wood and Molly McCulloch for both their companionship and for helping to determine that the optimal number of references for this dissertation must end in the number 9.

IDENTIFICATION OF INTRACRANIAL LESIONS WITH DUAL-ENERGY COMPUTED TOMOGRAPHY AND MAGNETIC RESONANCE PHASE IMAGING

Megan C. Jacobsen, B.A.

Advisory Professors: Dianna Cody, Ph.D. & Dawid Schellingerhout, M.D.

On conventional Single-energy Computed Tomography (SECT), lesions with an attenuation greater than 100 Hounsfield Units (HU) can be definitively diagnosed as calcification. However, low-density calcifications and hemorrhage may have overlapping attenuation ranges between 40 and 100 HU and, therefore, cannot be differentiated with SECT alone. On T2*-weighted Gradient Recalled Echo (GRE) MRI, these lesions appear as “foci of susceptibility” in which their signal is hypointense due to the magnetic susceptibility of the lesions differing from that of the background tissue.

Dual-energy Computed Tomography (DECT) and Phase-Sensitive Magnetic Resonance Imaging (PS-MRI) represent two new imaging paradigms which both have the potential to more accurately identify intracranial calcification and hemorrhage. In DECT, x-ray tomography is acquired at two tube voltages; because x-ray attenuation is energy- and material-dependent, the data can be used to differentiate between materials that may have the same signal level on SECT. PS-MRI utilizes the phase data from T2*-weighted MRI acquisitions to determine how the local magnetic field varies across the image. By applying post-processing algorithms such as Quantitative Susceptibility Mapping (QSM), the phase can be used to calculate the magnetic susceptibility of a lesion. Since calcifications are diamagnetic and hemorrhage paramagnetic, we can make inferences about a lesion’s composition from these algorithms.

The objective of this dissertation work was to characterize brain lesions, discovered with traditional imaging methods, as either hemorrhagic or calcific by using Dual-Energy Computed

Tomography (DECT) and Phase-Sensitive Magnetic Resonance Imaging (PS-MRI). To this end, MRI-compatible phantoms featuring models of both calcific and hemorrhagic lesions were developed and validated. This resulted in two phantoms with biologically similar lesion models that were then used to test the feasibility of differentiating calcific and hemorrhagic lesions with PS-MRI post-processing methods, in which QSM was able to accurately differentiate calcific and hemorrhagic lesion models. Finally, we undertook a patient trial testing the feasibility of identifying calcification and chronic hemorrhage in humans using both DECT and QSM in which the two modalities had accuracies of 99.7% (327/328) and 99.4% (326/328), respectively. The two modalities were concordant for 99.3% (148/149) lesions with SECT attenuation under 100 HU.

Table of Contents

Approval Page.....	i
Title Page	ii
Acknowledgements	iii
Abstract	v
Table of Contents	vii
List of Figures	xii
List of Tables.....	xxi
List of Abbreviations	xxv
1 Introduction	1
1.1 Significance	1
1.2 Objectives and Hypothesis	1
1.3 Specific Aims	2
1.4 Dissertation Organization	3
2 Background.....	4
2.1 Rationale	4
2.1.1 Intracranial Hemorrhage	4
2.1.2 Intracranial Calcification	6
2.1.3 Anticoagulant Use among Cancer Patients	7
2.2 DECT Implementations and Image Reconstruction.....	9

2.2.1	DECT Hardware Implementation.....	10
2.2.2	DECT Software Implementations	13
2.3	DECT Applications.....	17
2.3.1	Virtual Non-Contrast	17
2.3.2	Virtual Monoenergetic Images.....	18
2.3.3	Calcium Identification.....	18
2.3.4	Distinguishing Calcification and Hemorrhage	19
2.4	Magnetic Susceptibility.....	21
2.4.1	Diamagnetism	22
2.4.2	Paramagnetism	22
2.4.3	Superparamagnetism	22
2.5	MRI Phase Basics.....	23
2.5.1	Gradient Recalled Echo Pulse Sequences.....	24
2.5.2	Magnetic Susceptibility and MRI Phase.....	25
2.6	Susceptibility-Weighted Imaging.....	26
2.7	Quantitative Susceptibility Mapping.....	27
2.7.1	Mathematical Derivation of the Inverse Problem	28
2.7.2	QSM Methods	29
2.7.3	QSM Applications.....	31
3	Lesion Differentiation in Magnetic Resonance Imaging Phantoms	33
3.1	Introduction.....	33

3.2	Methods	34
3.2.1	MRI Phantom Materials	34
3.2.2	MRI Phantom Design.....	35
3.2.3	Material Validation Phantoms.....	37
3.2.4	MRI Scan Protocol	46
3.2.5	Image Analysis.....	48
3.3	Results	49
3.3.1	Hydroxyapatite and Iron Oxide Preliminary Phantoms.....	49
3.3.2	Hydroxyapatite and Iron Dextran Phantoms.....	55
3.3.3	Calcium Chloride Phantom (R3).....	63
3.3.4	Iron Oxidation State Phantom (R4).....	65
3.3.5	Final Biological Phantoms.....	68
3.4	Discussion	72
4	Magnetic Resonance Imaging Acquisition and Processing	77
4.1	Introduction.....	77
4.2	Methods	77
4.2.1	Phantoms	77
4.2.2	MRI Scan Prototcol.....	78
4.2.3	Phase-Sensitive MR Post-Processing	79
4.2.4	Image Analysis.....	79
4.2.5	Statistical Analysis.....	80

4.3	Results	80
4.3.1	Phantom RF1 Analysis	80
4.3.2	Phantom RF2 Analysis	84
4.3.3	Statistical Analysis.....	85
4.4	Discussion	88
5	Lesion Differentiation in Human Subjects with DECT and PS-MRI.....	92
5.1	Introduction.....	92
5.2	Methods	92
5.2.1	Study Population	92
5.2.2	Study Design.....	93
5.2.3	SECT and DECT Imaging.....	95
5.2.4	MR Imaging	96
5.2.5	Phase-Sensitive MRI Post-Processing	96
5.2.6	Image Registration and Segmentation	97
5.2.7	Reference Standard	98
5.2.8	SECT Analysis	99
5.2.9	DECT Analysis.....	99
5.2.10	QSM Analysis	100
5.2.11	Statistical Analysis.....	100
5.3	Results	101
5.3.1	Study Population	101

5.3.2	SECT Analysis	102
5.3.3	DECT Analysis	103
5.3.4	QSM Analysis	106
5.3.5	Statistical Analysis.....	110
5.4	Discussion	112
6	Conclusions	119
6.1	Summary of Findings	119
6.2	Advances in Knowledge	121
6.3	Limitations	123
6.4	Future Work.....	125
7	Appendix 1	128
8	Appendix 2.....	129
9	References	135
Vita	166

List of Figures

Figure 2.1: Linear attenuation coefficients for water, cortical bone, and Omnipaque 350 (iodinated contrast agent) demonstrating differences in the material attenuation properties across a range of diagnostic x-ray energies. In this example, cortical bone could be described as a linear combination of water and Omnipaque.	10
Figure 2.2: Schematics of DECT hardware implementations currently available, including a) fast kVp-switching, b) dual-source, c) dual-layer detectors, and d) split-filter systems.	11
Figure 2.3: Linear attenuation coefficients for gold (K-edge at 80.7 keV) and water. When the K-edge falls between 40 and 140 keV, it is possible that the measured attenuation at the low- and high-energies in DECT may return similar attenuation values.	15
Figure 2.4: Schematic of image-based three material decomposition. Point <i>a</i> represents the CT numbers of a measured voxel at the low and high tube voltages. The measured values are then projected onto the line between fat and soft tissue values along the red line. Thus, point <i>b</i> represents the virtual unenhanced CT numbers while <i>i</i> represents the amount of iodine present.	16
Figure 2.5: Attenuation curves for dense calcification (as modeled by low density cortical bone) and whole blood products. Note that blood products have a very similar curve shape as water with a slightly higher overall density.	19
Figure 2.6: Example of a plane of differentiation developed with geometric bisectors for a 1.5cm diameter lesion in the cerebrum, imaged at 132.5 mGy and reconstructed at 5 mm image thickness with a soft filter. Voxel data for the hemorrhagic lesions are shown in red, while voxel data for the calcific lesions are shown in gray.	20
Figure 2.7: DECT reconstructions of a) 68 keV, b) calcium(water), and c) water(calcium) in a phantom image acquired at 132.6 mGy CTDIvol with 5 mm slice thickness and a soft	

reconstruction filter. Lesion models in the phantom were 80 HU at 120 kVp SECT. Solid arrows indicate calcific lesions while unfilled arrows identify iron-based lesion models.....21

Figure 2.8: Diagrammed relationship between the MRI signal (S), the components measured in the real (Re) and imaginary (Im) channels, and the magnitude and phase of the signal.23

Figure 2.9: The MRI phase image displayed depicts phase wrapping at boundaries between $-\pi$ and π . Additionally, noise is amplified in low signal regions of the image.24

Figure 2.10: Susceptibility-weighted imaging (SWI) improves visualization of venous structures, as shown by comparison of a T2*-weighted GRE (a), Susceptibility-Weighted Angiography (b). The high-pass filtered phase image (c) from the SWAN sequence emphasizes the local magnetic field changes near the susceptibility lesion (black arrows).27

Figure 2.11: A multi-echo gradient recalled echo sequence (magnitude image, a) is used to generate a background subtracted phase image (b) and a Quantitative Susceptibility Map (c). Note the pineal calcification (arrow) and a punctate paramagnetic lesion in the globus pallidus (arrowhead) that both appear hypointense in the magnitude image and can be differentiated in the QSM.28

Figure 3.1: Preliminary phantom design demonstrating the vial positioning in the test tube holder (a) and the completed preliminary phantom (b) with the agarose background.....36

Figure 3.2: Schematic of the round phantom design. The cryovials measure 1 cm in diameter, and all vials were greater than 2 cm from the edge of the phantom and 2 cm away from all other vials.37

Figure 3.4: Diagram of the phantom R1. Hydroxyapatite is shown in blue, iron dextran in red, and 1% w/v agarose in gold. The numbers refer to the concentration of material in each vial (iron dextran in units of mg Fe/mL, hydroxyapatite in mg/mL).40

Figure 3.5: Phantom R2 with adjusted iron dextran and hydroxyapatite concentrations. Iron dextran concentration values in the diagram are given in mg Fe/mL while hydroxyapatite concentrations are given in mg/mL.	41
Figure 3.6: Phantom R4 arrangement of iron(III) and iron(II) chloride samples. Units are given in mg Fe/mL.	43
Figure 3.7: Phantom RF1, a calibration phantom, featuring hydroxyapatite, iron dextran, hemoglobin, and iron(III) chloride. The numbers above the vials refer to the concentration in units of mg/mL for hydroxyapatite and mg Fe/mL otherwise.	43
Figure 3.8: Diagram of the biological phantom with mixed materials. Lesion models with diagonal stripes represent mixtures while vials with smaller spots represent regions of differing material and concentration within a uniform background.	45
Figure 3.9: DECT water/calcium decomposition measurements for iron oxide and hydroxyapatite samples with matched SECT HU. Calcium density increases as SECT HU increases for both materials. Note that the use of the calcium/water material decomposition does not indicate that calcium was present within the iron oxide samples (see Section 2.3.4).	50
Figure 3.10: MFGRE magnitude images of the low concentration iron oxide (two bottom rows) and hydroxyapatite (two top rows) phantom for echo times of a) 4.5 ms, b) 14.5 ms, and c) 24.6 ms. At the highest echo time, the 10.47 mg/mL iron oxide sample (white arrow) becomes distorted. Note that very little signal is present in the iron oxide samples, even at low TE. Numeric labels represent the concentration of hydroxyapatite or iron oxide in units of mg/mL.	50
Figure 3.11: Iron oxide MFGRE signal at low concentrations. The signal in all samples dephased within a TE of 30 ms. Lower concentrations featured higher signal levels at lower TEs. The signal normalized to the first echo for each vial shows very little change in signal across the later echoes. The high normalized signal in the 10.47 mg/mL is solely indicative of the very low signal values across all echoes.	52

Figure 3.12: Hydroxyapatite MFGRE signals for low concentrations. The signal decreased steadily with increasing echo time (TE), and higher concentrations generally had lower signal levels. The normalized signal shows that higher concentrations decay at a slightly faster rate with increasing TE than lower concentrations.52

Figure 3.13: MFGRE magnitude images of the high concentration iron oxide (two upper rows) and hydroxyapatite (two lower rows) phantom with a) TE = 4.5 ms, b) TE = 14.5 ms, and c) TE = 24.6 ms. Numeric labels refer to the concentration of hydroxyapatite and iron oxide in each sample in units of mg/mL. Note the blooming in the iron oxide samples increases with TE and with increasing iron concentration.53

Figure 3.14: Hydroxyapatite signal in the high concentration preliminary phantom by echo time (TE). The normalized signal shows a clear concentration dependence in the decay rate of the signal with TE.54

Figure 3.15: Iron oxide signal in the high concentration phantom shows a low signal at all echo times for all concentrations of iron oxide present.55

Figure 3.16: MFGRE magnitude images of an iron dextran (ID) and hydroxyapatite (HAP) phantom with the round design; sample concentrations are given in mg/mL for HAP and mg Fe/mL for ID. Iron dextran is on the top half and hydroxyapatite on the bottom half, as indicated by the white line in (a). The iron dextran displays T1 shortening (bright signal), and a chemical shift is present in high concentrations, indicated by the cyan circle (a). Signal remains present in several iron dextran samples at the third (b), and fifth (c) echoes and higher concentrations of hydroxyapatite were tested to decrease the T2* further relative to prior phantoms.56

Figure 3.17: MFGRE signal changes with increasing echo time (TE) for iron dextran samples in a round phantom. Signal normalized to the first TE is displayed in the plot at the bottom to emphasize the concentration dependence of the signal decay.57

Figure 3.18: MFGRE signal changes with increasing echo time (TE) for hydroxyapatite samples in a round phantom. Signal normalized to the first TE is displayed in the plot at the bottom to emphasize the concentration dependence of the signal decay.	58
Figure 3.19: DECT calcium/water material decomposition data for iron dextran and hydroxyapatite samples. Note that sulfur is present in the iron dextran complex, which is not present amongst biological hemorrhage.	59
Figure 3.20: MFGRE signal and normalized signal for hydroxyapatite with biological T2* levels. The T2* ranges from 5.53 to 42.22 ms in this phantom.	61
Figure 3.21: MFGRE signal and normalized signal for iron dextran with T2* values within the range expected in normal gray and white matter. The T2* in this phantom ranges from 30.44 to 89.49 ms.	62
Figure 3.22: Calculated T2* versus the SECT attenuation of the hydroxyapatite and calcium chloride gels. The T2* of the calcium chloride is higher than that of the hydroxyapatite for all SECT levels investigated.	63
Figure 3.23: MFGRE magnitude signal for various concentrations of calcium chloride with and without signal normalization	64
Figure 3.24: Iron(II) Chloride MFGRE signal data. Units of concentration are given in mg Fe/mL. Note that while there is a concentration dependence in the normalized plot, there is relatively little signal dropout even at high concentrations.	66
Figure 3.25: Iron(III) chloride MFGRE signal curves. Units of concentration are given in mg Fe/mL. There is a large signal dropout at high iron concentrations that are not seen when the iron is in the 2+ oxidation state.	67
Figure 3.26: Normalized MFGRE signal curves for a) hydroxyapatite, b) iron(III) chloride), c) iron dextran, and d) human hemoglobin.	69

Figure 3.27: Voxel-wise $T2^*$ calculations for each sample displayed in the same plane along the z-axis. The four vials labeled ID/HAPm have an iron dextran background and hydroxyapatite masses, and additional analysis was performed for these samples.	70
Figure 3.28: An example of the histogram analysis for the iron dextran samples that contained hydroxyapatite masses. A kernel density estimate (black line) was fit to the data to estimate the mean $T2^*$ of the background and mass. This suggests that voxel-wise histogram analysis of $T2^*$ might contain characterizing information that could be used clinically.	70
Figure 3.29: A linear fit of the $T2^*$ estimates resulting from the voxelized (kernel density) and ROI-based (biexponential fit) $T2^*$ estimates for iron dextran lesions with hydroxyapatite masses demonstrates correlation between the two analysis methods.	72
Figure 4.2: SWAN filtered phase (in mrad), PDF (in mrad), and QSM (in ppb) means for the hydroxyapatite samples. Error bars represent the standard deviation in the mean value across three acquisitions.	81
Figure 4.1: Hemoglobin, iron dextran, and iron(III) chloride signal on a) SWAN filtered phase, b) PDF, and c) QSM images versus iron concentration. The error bars represent the standard deviation of a VOI measurement across three acquisitions. Note that the mean and standard deviation in an iron(III) chloride samples with the highest iron concentration each excluded an extreme outlier in both the PDF and QSM fits (see Figure 4.3).	83
Figure 4.3: Images of phantom RF1 demonstrate the impact of poor phase unwrapping in the PDF and QSM processing for an iron(III) chloride sample (yellow circles). The acquisition shown in the top row shows a primarily positive phase on PDF (a) with some residual phase wraps, but a positive QSM proportional with its iron concentration (b). The bottom row is another acquisition in the same scan session where the phase has a 2π shift in the PDF (c), and thus the estimated susceptibility was negative (d).	84

Figure 4.4: ROC analysis for SWAN filtered phase, PDF, and QSM data. The threshold indicates the threshold for which the sum of the true positive rate and the false negative rate were optimized. AUC is defined as the area under the curve.86

Figure 4.5: Histograms of the mean in all calcific and hemorrhagic lesion models over three acquisitions for SWAN filtered phase (a), PDF (c), and QSM (e) data. Representative images of phantom RF1 are included for the three image types: b) SWAN Phase, d) PDF and f) QSM. The colored polygons indicate the material within the samples: hydroxyapatite (blue), iron dextran (red), iron(III) chloride (green), and hemoglobin (gold). Units for the SWAN and PDF images are milli-radians; QSM is in units of ppb. One iron(III) chloride sample (green arrows) had errors in the phase unwrapping (d), which were improved in the QSM (f).87

Figure 5.1: Study flowchart showing flow from screening to study enrollment and imaging, to the analysis of individual lesions in subsets of known calcifications and unclassified lesions.95

Figure 5.2: Subject accrual flow chart..... 101

Figure 5.3: SECT values for lesions classified as hemorrhage and calcification by the reference standard. The dotted black line marks the current established threshold for differentiating between calcification and hemorrhage on SECT (100 HU). Note that applying this threshold rigidly would misclassify multiple calcific lesions as hemorrhagic, based on initial clinical classification. 102

Figure 5.4: ROC curves for Water(Calcium) and Calcium(Water) data compared to the ROC curve for SECT with a threshold of 100 HU. 104

Figure 5.5: a) Classification matrices for the DECT-based logistic model compared to the reference standard and b) the ROC curve for the DECT and SECT classification schemes. 105

Figure 5.6: DECT water(calcium) and calcium(water) data classified by the reference standard. a) A scatter plot of the water(calcium) and calcium(water) means for all 328 lesions.

The dotted black line represents the optimal threshold between calcification and hemorrhage in the logistic model, where a linear combination of the water and calcium data is equal to -2.675.

b) The logistic regression compared to the reference standard. 105

Figure 5.7: Histogram of the CSF susceptibility measurements for 50 patients with a Gaussian fit (left). A quantile-quantile plot is shown on the right to display the deviation of individual measurements from the displayed normal distribution (right). A Shapiro-Wilk test did not reject the null hypothesis that the distribution was Gaussian ($p = 0.71$). 107

Figure 5.8: a) Classification matrices for the QSM-based logistic model compared to the reference standard and b) the ROC curve for the QSM and SECT classification schemes.... 108

Figure 5.9: a) Mean QSM for each lesion versus the SECT attenuation in HU. Note that two lesions measure both over 100 HU and well above a susceptibility of 37.6 ppb. These two lesions are known as outliers where calcification is present adjacent to a vein or hemorrhagic lesion. b) Histograms of the QSM mean for calcifications and hemorrhages with kernel density estimates of the distributions. The optimal threshold of 37.6 ppb is shown in yellow in both plots..... 109

Figure 5.10: A 48-year old female patient with a history of right frontal craniotomy and a lobular mass consistent with cavernoma presenting as a large focus of susceptibility on the MFGRE (TE = 14.5 ms) (a). The SECT (b) demonstrates a densely calcified region within the lesion (red outline) with HU greater than 100. (c) QSM of the lesion shows high magnetic susceptibility throughout the lesion with regions of apparent aliased signal. The calcification does not present with the expected negative susceptibility. 110

Figure 5.11: A 73-year old female patient with a history of metastatic melanoma with Gamma Knife therapy. (a) The globus pallidus shows mineralization consistent with aging that causes low signal on the MFGRE (TE = 14.5 ms). (b) SECT shows a small calcification (green outline) within the globus pallidus with attenuation over 100 HU. (c) QSM shows consistently

high signal in the globus pallidus despite the presence of calcification, but other calcific lesions (yellow arrows) demonstrate the expected negative susceptibility.	110
Figure 8.1: Clinical trial screening software example.	129
Figure 8.2: Dark lesion appearing in the right hemisphere (left, arrow). The next image in the series (middle) shows that both sides are symmetric. An example of the sagittal anatomy on T1-weighted imaging (https://www.imaio.com/en/e-Anatomy/Head-and-Neck/Brain-MRI-3D) with the level of the "lesions" shown.....	131
Figure 8.3: A calcification in the dura mater inside the skull (A) and separating the cerebral hemispheres (falx cerebri, B). These known calcifications can appear as dark lines along part or all of the falx cerebri.	132
Figure 8.4: Iron deposition in the putamen (left, arrows) and globus pallidus (right, arrows) in the basal ganglia.	132
Figure 8.5: Pineal gland calcification located centrally in the image.	133
Figure 8.6: Choroid Plexus (arrows) mineralization. Usually found on the same slice or near the z-location of the pineal gland.	133
Figure 8.7: Iron deposition found in the Dentate Nuclei (arrows) in the cerebellum. This can appear darker, similar to the basal ganglia examples.	134

List of Tables

Table 2.1: Summary of hemorrhagic event risk in patients with cavernous malformation.	5
Table 2.2: Single-Energy CT and conventional MRI image properties of intracranial hemorrhage by stage.	6
Table 3.1: Phantom materials simulating calcific and hemorrhagic lesions	34
Table 3.2: Hydroxyapatite and Iron(III) Oxide sample specifications for both low and high concentrations.	38
Table 3.3: Hydroxyapatite and Iron Dextran gel specifications and their estimated SECT attenuation in HU for the first iron dextran testing. This phantom had approximately matched SECT HU between the iron dextran and hydroxyapatite gels.	39
Table 3.4: Hydroxyapatite and Iron Dextran gel specifications for a second phantom. In this instance, SECT HU was not matched between the calcium and iron gels.	41
Table 3.5: Specifications for concentrations of hydroxyapatite, iron dextran, iron(III) chloride, and hemoglobin to be included in finalized calibration curves. Iron dextran concentration is given in mg iron/mL due to the lack of a nominal density for the dextran complex as a whole. Hemoglobin was assumed to be 0.31% iron per sample specifications. ...	44
Table 3.6: Agarose gel composition for a biological phantom with mixed materials. For the lesions with masses ("Mass"), Material 1 indicates the composition of the uniform background material while Material 2 indicates the concentration within the mass. Concentrations are reported in mg Fe/mL for iron containing compounds and mg/mL for hydroxyapatite.....	46
Table 3.7: MRI acquisition details for all phantom experiments, including repetition time (TR), inversion time (TI), receive bandwidth (BW), field-of-view (FOV), acquisition matrix.....	47

Table 3.8: Phantom experiment SECT and DECT protocols.....	48
Table 3.9: T2* values for hydroxyapatite and iron oxide samples of varying concentrations. The mean signal over five images was used to calculate T2*.....	53
Table 3.10: T2* values for hydroxyapatite samples of varying concentrations. The mean signal over five images was used to calculate T2*.....	55
Table 3.11: Calculated T2* for iron dextran and hydroxyapatite in a phantom with approximately matched SECT HU ranges.....	59
Table 3.12: Calculated T2* from the monoexponential fits for various concentrations of iron dextran and hydroxyapatite in a phantom with biological susceptibility levels.	60
Table 3.13: Calculated T2* for various concentrations of iron(II) chloride and iron(III) chloride in a phantom. The 0.4 mg Fe/mL iron(II) chloride sample was excluded due to the presence of an air bubble.....	65
Table 3.14: Mean \pm standard deviation of the T2* calculated for three acquisitions of the MFGRE.....	68
Table 3.15: Mean and standard deviation of each mixture or sample without visible mass for the voxel-wise calculation of T2*.	71
Table 3.16: T2* estimates for lesions containing masses, resulting from the biexponential fit of the ROI means and the peak location of the T2* kernel density estimate for the voxel-wise calculations.....	71
Table 4.1: MRI acquisition details for all phantom experiments, including repetition time (TR), inversion time (TI), receive bandwidth (BW), field-of-view (FOV), acquisition matrix.....	78
Table 4.2: Mean and standard deviation in phantom RF1 for the SWAN filtered phase, PDF, and QSM images. Concentration for hydroxyapatite is given in units of mg/mL while iron-containing compounds are reported in mg Fe/mL. Values marked by an asterisk have high variability between acquisitions and correspond with the samples with the highest magnetic susceptibility in the phantom.	82

Table 4.3: Predicted susceptibility based on the mixture concentrations in phantom RF2 input into the calibration curves for QSM defined in Phantom RF1. These values were compared to the measured susceptibility in the mixtures, and the percent error was calculated	85
Table 5.1: Study inclusion and exclusion criteria. Additional contraindications to MRI can be found in Appendix 1	93
Table 5.2: Study SECT and DECT imaging protocols. The scan range, image thickness, beam width, and field-of-view (FOV) were held constant between the two examinations.....	96
Table 5.3: MRI acquisition details for the patient trial, including repetition time (TR), inversion time (TI), receive bandwidth (BW), field-of-view (FOV), acquisition matrix	97
Table 5.4: DECT logistic regression. The equation for the fit is given in Equation 5.1. A p-value of less than 0.05 represents the statistical significance of the parameter within the model (indicated by *).	103
Table 5.5: Mean SECT, water(calcium), and calcium(water) measurements for lesions classified as hemorrhage and calcification in the DECT-based logistic regression.	104
Table 5.6: Mean SECT and QSM measurements for lesions classified as hemorrhage and calcification based on a threshold of 37.6 ppb.	107
Table 5.7: Classification matrix for the QSM classifications of all lesions versus the DECT classifications for all lesions	111
Table 5.8: Classification matrix for the QSM classifications of all lesions versus the DECT classifications for lesions with SECT greater than 100 HU.....	111
Table 5.9: Classification matrix for the QSM classifications of all lesions versus the DECT classifications for lesions with SECT less than 100 HU.	111
Table 5.10: Comparison of the ROC analysis for SECT (threshold = 100 HU), DECT, and QSM ROC analyses. Values were calculated for water(calcium) and calcium(water) images in the whole dataset. Dashes represent values that could not be calculated due to	

division by zero. The AUC for the SECT data was calculated assuming a threshold of 100 HU.

..... 112

List of Abbreviations

3D	Three Dimensional
CT	Computed Tomography
CTDI _{vol}	Computed Tomography Dose Index Volumetric
CV	Coefficient of Variation
DECT	Dual-Energy CT
DFOV	Display Field of View
DICOM	Digital Imaging and Communications in Medicine
GE	General Electric
GRE	Gradient Recalled Echo
GSI	Gemstone Spectral Imaging
HU	Hounsfield Unit
keV	Kilo-Electron Volt
kVp	Kilo-Voltage Peak
mA	Milliamperes
mAs	Milliampere-Second
MFGRE	Multi-echo Fast Gradient Recalled Echo
MR	Magnetic Resonance
NEX	Number of Averages
PDF	Projection onto Dipole Fields
QSM	Quantitative Susceptibility Mapping
R ²	Squared Pearson R-Value
ROI	Region of Interest
SD	Standard Deviation

SECT	Single-Energy CT
SFOV	Scan Field of View
SWAN	Susceptibility-Weighted Angiography
SWI	Susceptibility Weighted Imaging
TE	Echo Time
TR	Repetition Time
UTE	Ultra-short Echo Time

1.1 Significance

Using Single-Energy Computed Tomography (SECT), both hemorrhagic and calcific lesions are hyperintense relative to the background brain tissue, and the CT numbers of both lesion types may overlap, depending on their composition and density. Lesions that have a CT number of over 100 Hounsfield Units (HU) on SECT are definitively calcific (1, 2); however, in the region of approximately 50 – 100 HU, the signal levels of hemorrhage and low-density calcifications overlap, and differentiation based on the CT number becomes unreliable. On conventional T2*-weighted Gradient Recalled Echo (GRE) Magnetic Resonance Imaging (MRI), both calcific and hemorrhagic lesions appear as black signal voids in the image known as foci of susceptibility, and the two material types are indistinguishable. GRE pulse sequences are highly sensitive to these lesion types, and foci of susceptibility are a common incidental finding on brain MRI.

The presence of prior hemorrhage in the brain is a contraindication for anticoagulant therapies because they increase the risk of large brain bleeds. Additionally, certain disease profiles lend themselves towards either calcification or hemorrhage. Therefore, developing methods to distinguish calcific and hemorrhagic lesions allows for improved risk management and differential diagnosis amongst patients.

1.2 Objectives and Hypothesis

The objective of this project is to characterize brain lesions, discovered with traditional imaging methods, as either hemorrhagic or calcific by using Dual-Energy Computed Tomography (DECT) and Phase-Sensitive Magnetic Resonance Imaging (PS-MRI). These

modalities may increase or improve the information available to the radiologist regarding differential diagnosis and clinical management. Hemorrhagic lesions carry a risk of further bleeds while calcifications are generally benign. **The central hypothesis is that DECT and PS-MRI can be used to accurately classify foci of susceptibility detected on conventional MRI as either hemorrhage or calcification.**

1.3 Specific Aims

To test the central hypothesis, we have developed the following three specific aims:

Specific Aim 1: Design and construct an MRI-compatible phantom with calcific and hemorrhagic lesion models.

Subaim 1.1: Design and build an MRI-compatible phantom with varying densities of calcium and iron.

Subaim 1.2: Validate the phantom materials with conventional SECT, conventional MRI, DECT, and PS-MRI.

Subaim 1.3: Construct a final MRI-compatible phantom with calcific and hemorrhagic lesion models within biological constraints.

Specific Aim 2: Optimize the imaging acquisition schema and post-processing methods to maximize the specificity of calcification and hemorrhage classification.

Specific Aim 3: Conduct a human trial comparing the identification of intracranial calcification and hemorrhage using DECT and PS-MRI *in vivo*.

Subaim 3.1: Compare the accuracy of DECT and PS-MRI for identification of known intracranial calcifications (lesions measuring greater than or equal to 100 HU on SECT).

Subaim 3.2: Assess the concordance of DECT and PS-MRI for identification of intracranial hemorrhage and calcification measuring less than 100 HU on SECT.

1.4 Dissertation Organization

This dissertation is organized in the following way: Chapter 2 provides background information on hemorrhagic and calcific lesions, DECT, and PS-MRI techniques. Chapter 3 details Specific Aim 1 and presents the results of the MRI-compatible calcification and hemorrhage phantom experiments. Chapter 4 addresses Specific Aim 2 and covers the development of the pulse sequences and the mathematical models used to differentiate calcification and hemorrhage. Chapter 5 covers Specific Aim 3 and the results of a clinical trial comparing the use of DECT and PS-MRI *in vivo*. Lastly, Chapter 6 summarizes the dissertation and future avenues for this work.

2.1 Rationale

2.1.1 Intracranial Hemorrhage

Intracranial hemorrhage (ICH) is associated with a wide variety of etiologies, including—but not limited to—brain tumors, aneurysms, arteriovenous malformations, and hypertension (3, 4). In our patient population within a large, academic cancer hospital, we are particularly concerned with hemorrhage within brain malignancies as well as cavernous malformations, a type of venous malformation that is a common incidental finding on brain Magnetic Resonance Imaging (MRI) (5-7). Both lesion types may lead to clinically significant intracranial bleeding.

Cavernous malformations, also known as cavernomas or cavernous angiomas, are mulberry-shaped bundles of blood vessels that are often asymptomatic (8-11). Cavernomas are found in 0.4-0.8% of the general population, and most are found incidentally on MRI (7, 12, 13). However, *de novo* development of cavernous malformations following cranial radiation therapy has been well documented in the literature (14-18). Amongst long-term survivors of childhood malignancy treated with cranial irradiation, the incidence of cavernoma is estimated to be between 3.0% and 31.5% (17-22). While there is a wide reported range of the frequency of cavernomas amongst cancer survivors, this may be caused by differences in the follow-up time and imaging techniques used in the reported studies. Cavernomas also carry an inherent risk of larger clinical bleeds of 0.7 – 6.5% per person-year in prospective studies (9-11, 13, 23, 24). The results of these studies can be found in Table 2.1. A study by Salman et al found that the 5-year risk of mortality due to a cavernous malformation hemorrhaging was 4.5% (25).

Table 2.1: Summary of hemorrhagic event risk in patients with cavernous malformation.

Authors & Year	Number of Patients	Hemorrhage Rate/Patient-Year (%)	Re-hemorrhage Rate/Patient-Year (%)
Moriarty et al., 1999 (13)	68	3.1	NA
Kondziolka et al., 1995 (10)	122	1.3	4.5
Zabramski et al., 1994 (9)	31	6.5	NA
Flemming et al., 2012 (23)	292	2.25	6.19
Salman et al., 2012 (25)	139	2.4 (5-year risk)	29.5 (5-year risk)
Labauge et al., 2001 (11)	33	4.3	NA

The appearance of ICH on MRI and CT changes over time. ICH evolves through the following phases: hyperacute (< 12 hours since onset), acute (12 hours to 2 days), early subacute (2-7 days), late subacute (8 days to 1 month), and chronic (> 1 month) (26). Hyperacute hemorrhage consists primarily of fluid with blood products, including hemoglobin, and has an attenuation of 40 – 60 Hounsfield Units (HU) (3, 26). As the lesion progresses through the acute and early subacute states, clotting begins, the hematocrit level rises, and globin and fibrin form, causing increases in x-ray attenuation to between 60 and 80 HU (3, 26). In the early subacute phase, the clot retracts and further increases in attenuation up to approximately 100 HU before cell lysis begins and the protein structures of the clot are broken down, causing the attenuation to decrease through the late subacute stage until the lesion becomes chronic (3, 26).

While the CT appearance of hemorrhage depends primarily on the density of the clot and the associated iron levels, the MR appearance depends on the pulse sequence used and the form of hemoglobin—or its byproducts—present at the time of imaging (Table 2.2). In the subacute phase, oxyhemoglobin dominates the MRI signal in the lesion; the signal in the acute phase is due to deoxyhemoglobin (3, 26). Deoxyhemoglobin is metabolized to methemoglobin, which is

present within the intracellular compartment in the early subacute phase and is transferred to the extracellular space as cell lysis begins in the late subacute phase (3, 26). Finally, the methemoglobin is metabolized, and the iron is stored in hemosiderin deposits surrounding the rim of the lesion (3, 26).

Table 2.2: Single-Energy CT and conventional MRI image properties of intracranial hemorrhage by stage.

<i>ICH Stage</i>	CT Attenuation (HU)	Hemoglobin Product	T1-weighted MR	T2-weighted MR	T2*-weighted GRE MR
<i>Hyperacute</i>	40 – 60	Oxyhemoglobin	Isointense or Slightly hyperintense	Hyperintense	Hypointense Rim
<i>Acute</i>	60 – 80	Deoxy-hemoglobin	Isointense or hypointense	Hypointense	Hypointense Rim Progressing to Center
<i>Early Subacute</i>	80 – 100	Intracellular Methemoglobin	Hyperintense	Hypointense	Hypointense
<i>Late Subacute</i>	Decreasing 0.7 – 1.5 HU/day	Extracellular Methemoglobin	Hyperintense	Hyperintense	Hypointense
<i>Chronic</i>	25 – 35 HU	Hemosiderin	Isointense or Hypointense	Hypointense	Hyperintense or Isointense Core with Hypointense Rim

Note: Table adapted from reference (26) with additional data from reference (3).

2.1.2 Intracranial Calcification

Intracranial calcifications are a common incidental—and often normal—finding on imaging examinations of the brain (27). The most common forms include calcification of the pineal gland, which affects up to 40% of the population by age 20 (27), the choroid plexus (28), and dura mater (29). The incidence of these physiologic calcifications increases with patient age (27). Other types of calcification are a symptom of metabolic disorders, congenital or acquired infections, parasitic disease, and both benign and malignant brain tumors (30-35). Disorders of the parathyroid are associated with calcifications of the basal ganglia, subcortical white matter,

thalami, and cerebellum (33-35). Examples of congenital etiologies featuring intracranial calcifications include neurofibromatosis type II and Sturge-Weber syndrome (36-38). Infections such as Human Immunodeficiency Virus (39), tuberculosis (40, 41), and the parasitic disease neurocysticercosis (42) are also commonly associated with multiple calcifications within the brain parenchyma.

In the realm of cancer diagnosis and treatment, the presence of calcification is particularly important for differentiating oligodendroglioma from other brain cancers or benign intracranial lesions. Up to 90% of oligodendrogliomas contain calcium deposits, while the majority of other brain malignancies, including glioblastoma multiforme, typically do not (31, 32, 43). Additionally, calcifications are a long-term effect of past radiotherapy to the brain and can be caused by certain chemotherapies (44). Unlike intracranial hemorrhage, calcifications within the brain typically do not cause morbidity to the patient.

On conventional T1- and T2-weighted MRI, calcifications do not consistently provide the same signal intensity relative to normal tissue (45). Dense calcifications have low water content, which lowers the available MR signal (46); meanwhile, diffuse calcifications may shorten T1 and T2 due to water's interaction with the porous surface of the calcium salts (47). On T2*-weighted MRI, calcium is consistently hypointense but can mimic microbleeds or hemorrhages. On CT, a signal measurement of over 100 HU is a definitive marker for calcification (2); however, diffuse calcifications may have CT numbers less than 100 and may mimic hemorrhagic lesions using conventional SECT.

2.1.3 Anticoagulant Use among Cancer Patients

The risk of venous thromboembolism is increased for patients with cancer over those in the general population, even in ambulatory patients, with rates of 4.1 to 7.4% (48-52). Inpatient treatment of cancer leads to further increases in the likelihood of morbidity or mortality due to

thromboembolism. Consequently, oncology patients are frequently prescribed prophylactic anticoagulation to minimize the occurrence of deep vein thrombosis and pulmonary embolism (53-55). While this lowers overall morbidity from complications of cancer and its treatment, care must be taken to appropriately use prophylaxis because of the risk of inducing a hemorrhagic stroke.

The risk of bleeding from cavernous angiomas while on anticoagulant therapy has not been well defined. Recently, several investigators have attempted to determine the risk associated with antithrombotic therapies in patients with cavernomas. In a cohort of 292 patients with diagnosed cavernomas studied by Flemming et al, only six patients were placed on anticoagulant therapy, and no prospective or recurrent bleeds were recorded amongst those patients (56). Schneble et al also found that there were no hemorrhages in 26.4 person-years of observation amongst five patients with diagnosed cavernoma that were prescribed warfarin (57). However, there have been several documented case studies of cavernous angioma bleeds occurring in patients receiving antithrombotic therapy, including one instance of a known asymptomatic cavernoma hemorrhaging following treatment with low-molecular weight heparin following surgery (58, 59). Overall, due to the small sample sizes in these studies, the results cannot be considered conclusive (57, 60, 61).

Anticoagulant use is contraindicated in patients that have had prior bleeds within the brain because the risk of large, symptomatic hemorrhage is increased following smaller bleeds that may have been asymptomatic and found incidentally. These include all lesions that may have indications of chronic or acute hemorrhage on imaging exams of the brain, including, but not limited to venous malformations, primary brain tumors, and hemorrhagic metastases of the brain.

2.2 DECT Implementations and Image Reconstruction

Dual-Energy Computed Tomography (DECT) provides unique opportunities to differentiate materials in the human body. The theoretical underpinnings of DECT were developed in the late 1970s and first implemented in the 1980s (62-67). However, due to limitations in the CT hardware and computing power, the potential of DECT was not fully realized until the first commercial dual-source CT scanner was released in 2005 (68). As of 2018, the major manufacturers have added DECT capabilities to at least one of their commercially available CT systems, and have independently developed variations on the hardware used to acquire DECT exams and the software used to analyze the data (69).

DECT is based upon the premise that the CT number, measured in Hounsfield Units (HU), varies with x-ray energy (E) according to the following equation (70):

$$CT\ Number = 1000 \times \frac{\mu_x(E) - \mu_{water}(E)}{\mu_{water}(E)} \quad \text{Equation 2.1}$$

where μ_x represents the linear attenuation coefficient of an unknown material x and μ_{water} is the linear attenuation coefficient for water. The linear attenuation coefficient is a function of x-ray energy and depends on the material. For example, iodine—commonly used in clinical CT contrast agents—has a very high attenuation coefficient at low x-ray energies due to the prevalence of photoelectric interactions with high Z materials, and the attenuation decreases as the energy decreases due to Compton scatter becoming the predominant interaction at higher energies. For low Z materials such as water, the attenuation coefficient is much more stable with x-ray energy. The difference in the shapes of these curves allows for the differentiation of materials with the use of two or more energy spectra (Figure 2.1).

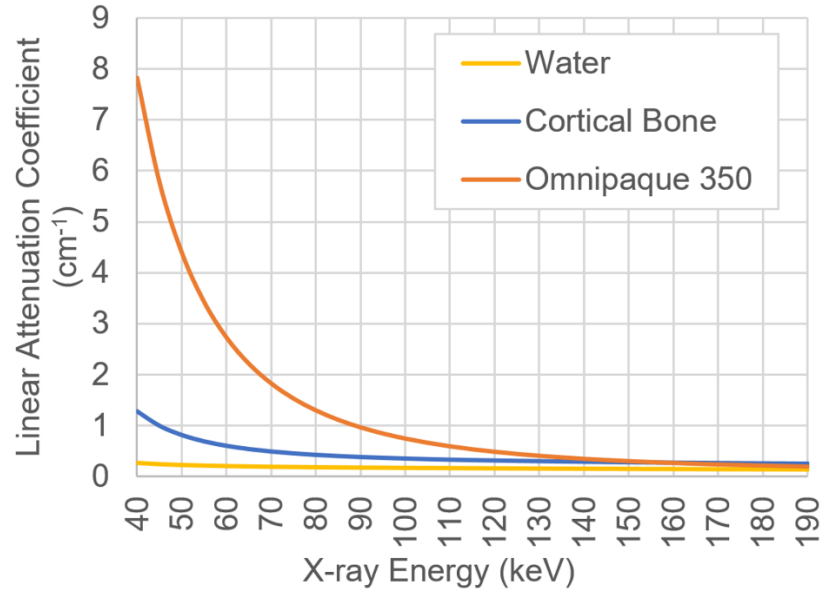


Figure 2.1: Linear attenuation coefficients for water, cortical bone, and Omnipaque 350 (iodinated contrast agent) demonstrating differences in the material attenuation properties across a range of diagnostic x-ray energies. In this example, cortical bone could be described as a linear combination of water and Omnipaque.

2.2.1 DECT Hardware Implementation

There are six major hardware implementations of DECT currently available in the marketplace. The first commercially available DECT was a dual-source (DS) system with two x-ray tube and detector arrays, which allowed for scanning with two separate energies (Figure 2.1b). The first system of this type became available in 2005 (Definition, Siemens Healthineers, Forchheim, Germany), and there have been two additional dual-source scanners released as of 2018 (Definition Flash and Definition Force, Siemens). There are several advantages to this type of system. First, the potential spectral separation is maximized because there are two separate x-ray spectra, and additional filtration can be placed on one or both tubes to separate the spectra further (71, 72). Since its first release, there have been two additional scanner models released using this hardware scheme—the Siemens Definition Flash and Definition Force scanners—known as 2nd and 3rd generation DS-DECT. One downside of these systems is that there is a temporal mismatch between projections at the low and high energy levels; additionally,

scattered radiation from one x-ray tube and detector pair can enter the other detector array, known as cross-scatter, and must be accounted for during the image reconstruction process.

The second DECT hardware implementation to be released commercially was the fast peak kilovoltage (kVp) switching systems (Figure 2.2a) developed by General Electric Healthcare (HD750 and Revolution CT, GE Healthcare, Waukesha, WI). On these systems, the generator switches from 80 kVp to 140 kVp between alternating projections. This acquisition method allows for acquisition of DECT data in which the two spectra have a nearly perfect temporal agreement but limits the degree of spectral separation that is feasible because added filtration is not possible and data is acquired continuously during the kVp-switching process (73, 74).

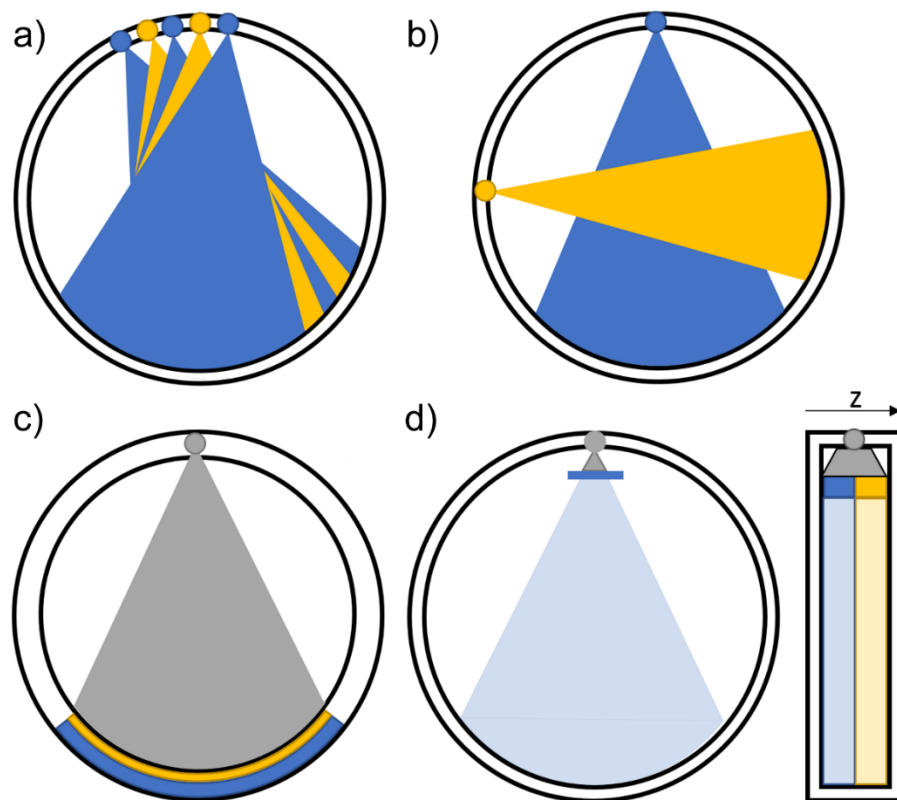


Figure 2.2: Schematics of DECT hardware implementations currently available, including a) fast kVp-switching, b) dual-source, c) dual-layer detectors, and d) split-filter systems.

Dual-layered detector DECT systems, such as the Philips IQon (Philips Healthcare, Best, The Netherlands), also utilize a single x-ray tube (Figure 2.2c). These systems operate at a single kVp, and the resulting data is split into two spectra by using a detector with two sets of electronics. The top layer of the detector preferentially absorbs low-energy photons, while high-energy photons penetrate the first layer and are absorbed in the bottom layer of the detector. The resulting data can either be used to create low- and high-energy image sets and DECT reconstructions or the data acquired by the two layers can be combined to reconstruct a conventional SECT image (75-78). It is unclear how well this method separates the spectra since a high-energy photon could be scattered in the first layer, depositing a portion of its energy in each detector layer. However, these systems are advantageous for performing comparisons of DECT and conventional SECT (75) since DECT data can be stored for every exam for later processing as needed without burdening radiologists with additional image series.

Split-filter systems operate in dual-energy mode with a single x-ray tube run at 120 kVp but create two different energy spectra along the z-axis of the scanner via the addition of additional filtration (Figure 2.2d) (79, 80). Half of the supplementary filter is gold—softening the x-ray spectrum—and half is tin, which hardens the spectrum (81-84). This paradigm results in relatively little spectral separation, which may be further degraded by the presence of cross-scatter. The available technique parameters are limited to helical scans with a low pitch to obtain adequate photon counts in each energy bin. Additionally, these filters may induce artifacts in the images when the air outside the body is included within the region of helical over-ranging due to the interpolation required to combine the data from various times and locations along the z-axis. The poor temporal matching between the high and low energy projections may also limit the use of certain reconstruction algorithms, and the long scan times make this dual-energy technique more susceptible to motion artifacts.

There are also systems designed to incorporate slow kVp-switching to acquire DECT data. These scanners acquire two consecutive rotations at the same z-location at two different energies. This method is utilized by the Canon (formerly Toshiba) Aquilion One CT (Canon Medical Systems, Otawara, Japan) (85). This scanner is capable of scanning whole organs in one rotation, which minimizes the chances of motion artifacts between projections. However, there is still a temporal mismatch between the high and low energy projections. Compared to fast kVp-switching, there is the potential for better spectral separation, but there has been relatively little research performed using this DECT methodology to date (86-91).

Finally, there are scanners which can perform DECT acquisitions by first acquiring a scan at low energy followed by a scan at higher energy (69, 92). While this is a highly cost-effective option and provides very good spectral separation, it is particularly sensitive to patient motion, and cannot be used to assess iodine concentrations in tissue because of the timing differences between the two scans.

2.2.2 DECT Software Implementations

DECT data is processed either through projection-based methods, which are performed on the raw sinogram data prior to image reconstruction (93-96) or by image-based methods that first reconstruct low- and high-energy images and subsequently calculate DECT properties (97, 98).

Projection-based methods require temporal co-registration of the low- and high-energy datasets; the fast kVp-switching and dual-layer detector systems utilize this approach to DECT reconstruction. In these algorithms, DECT data is derived using basis material decomposition, which posits that any material can be modeled as a linear combination of the attenuation coefficients of two predefined materials, the proof of which is shown here. X-ray attenuation depends on two primary mechanisms in the diagnostic energy range: photoelectric effect and

Compton scattering, the fraction of scatter caused by each mechanism is defined as f_{PE} and f_C , respectively. Both f_{PE} and f_C depend on the x-ray energy, E . Therefore, the linear attenuation coefficient (μ) of any material can be defined as a linear combination of the attenuation due to each of those effects (Equation 2.2).

$$\mu(E) = \alpha f_{PE}(E) + \beta f_C(E) \quad \text{Equation 2.2}$$

Therefore, the attenuation of the basis materials 1 and 2 gives us the following system of equations:

$$\begin{cases} \mu_1(E) = \alpha_1 f_{PE}(E) + \beta_1 f_C(E) \\ \mu_2(E) = \alpha_2 f_{PE}(E) + \beta_2 f_C(E) \end{cases} \quad \text{Equation 2.3}$$

Solving Equation 2.3 for the photoelectric and Compton scatter fractions returns Equation 2.4 and Equation 2.5:

$$f_{PE}(E) = \frac{\beta_2 \mu_1(E) - \beta_1 \mu_2(E)}{\alpha_1 \beta_2 - \alpha_2 \beta_1} \quad \text{Equation 2.4}$$

$$f_C(E) = \frac{\alpha_2 \mu_1(E) - \alpha_1 \mu_2(E)}{\alpha_2 \beta_1 - \alpha_1 \beta_2} \quad \text{Equation 2.5}$$

Equation 2.4 and Equation 2.5 define the photoelectric and Compton scatter fractions in terms of the attenuation of materials 1 and 2. Substituting these back into Equation 2.2 returns:

$$\mu(E) = \alpha \left(\frac{\beta_2 \mu_1(E) - \beta_1 \mu_2(E)}{\alpha_1 \beta_2 - \alpha_2 \beta_1} \right) + \beta \left(\frac{\alpha_2 \mu_1(E) - \alpha_1 \mu_2(E)}{\alpha_2 \beta_1 - \alpha_1 \beta_2} \right) \quad \text{Equation 2.6}$$

Equation 2.6 is algebraically equivalent to Equation 2.7.

$$\mu(E) = a_1 \mu_1(E) + a_2 \mu_2(E) \text{ where} \quad \text{Equation 2.7}$$

$$a_1 = \frac{\alpha \beta_2 - \beta \alpha_2}{\alpha_1 \beta_2 - \alpha_2 \beta_1} \text{ and } a_2 = \frac{\beta \alpha_1 - \alpha \beta_1}{\alpha_1 \beta_2 - \alpha_2 \beta_1}$$

The attenuation coefficients of materials 1 and 2 are known *a priori*. Measuring the attenuation of the voxel in question at two energy levels returns a system of two equations with two unknowns that can be solved to determine the amount of materials 1 and 2. The resulting quantities of each material, which can be given in terms of density, represent the amounts of

each material that would be required to model that voxel's attenuation properties (Equation 2.8).

$$\begin{cases} \mu(E_{low}) = a_1\mu_1(E_{low}) + a_2\mu_2(E_{low}) \\ \mu(E_{high}) = a_1\mu_1(E_{high}) + a_2\mu_2(E_{high}) \end{cases} \quad \text{Equation 2.8}$$

It should be noted that while the basis materials can be chosen by the user, the two materials selected must have sufficiently different attenuation properties in order to achieve an accurate classification of materials. It is optimal to have one low Z material—water or soft tissue—and one higher Z material—iodine or calcium. Additionally, users must be aware of the energy of the K-edge of the material. Since CT data is polychromatic, the energy range over which data is acquired is approximately 40 to 140 keV for a system with a maximum kVp of 140. As a result, if the K-edge of the material of interest falls within this range, the attenuation differences between the low- and high-energy measurements may not be large enough to calculate accurate material density estimates (Figure 2.3).

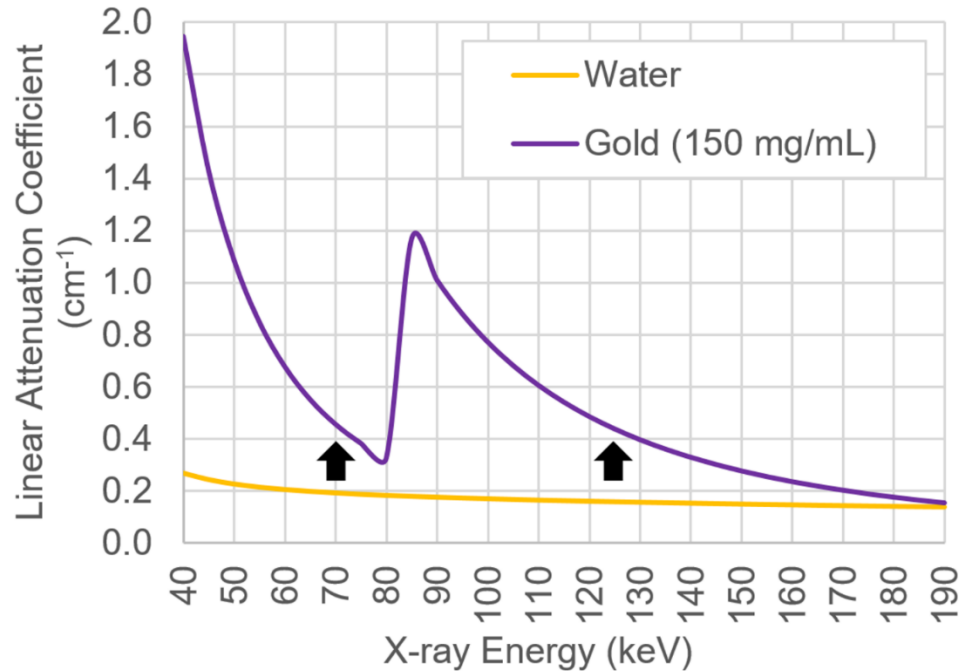


Figure 2.3: Linear attenuation coefficients for gold (K-edge at 80.7 keV) and water. When the K-edge falls between 40 and 140 keV, it is possible that the measured attenuation at the low- and high-energies in DECT may return similar attenuation values.

Image-space DECT analysis is performed following reconstruction of low- and high-energy CT datasets (69, 99-101). All acquisition methods that cannot ensure temporal registration of the two datasets use image-based reconstruction. These algorithms may use up to three materials, which are mapped to predefined CT numbers in the low- and high-energy images and include a volume conservation term where the sum of the volume fractions of each material must equal one (96). Figure 2.4 shows a theoretical example of an abdominal virtual non-contrast algorithm where the three materials are soft tissue, fat, and iodinated contrast. For a given measured voxel, a , the point can be projected onto the line segment between the two low-density tissues to point b along a second line originating from the defined iodine point. Point b represents the virtual non-contrast values for the voxel, and the distance between points a and b , the length i , is proportional to the amount of iodine present in the voxel. The value i can be presented as the attenuation in HU attributed to iodine enhancement or as an iodine concentration. While this theoretical example utilized iodine as a high Z material, different applications may utilize different materials than those depicted here.

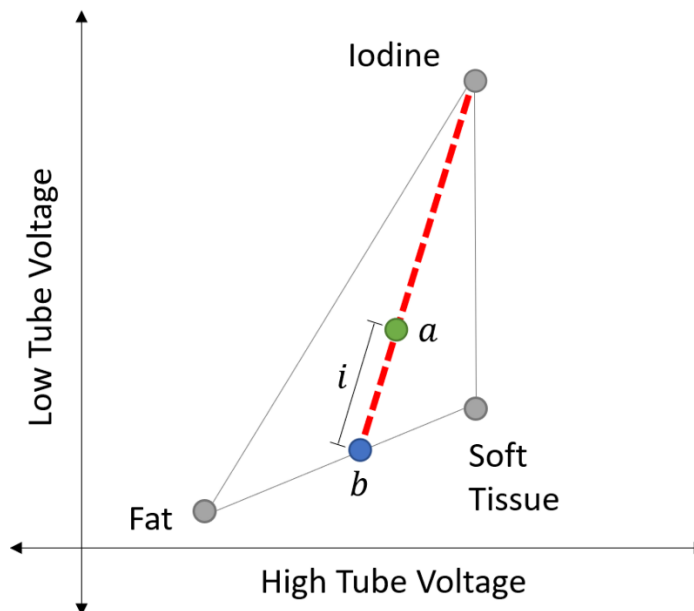


Figure 2.4: Schematic of image-based three material decomposition. Point a represents the CT numbers of a measured voxel at the low and high tube voltages. The measured values are then projected onto the line between fat and soft tissue values along the red

line. Thus, point b represents the virtual unenhanced CT numbers while i represents the amount of iodine present.

2.3 DECT Applications

2.3.1 Virtual Non-Contrast

One of the primary clinical applications of DECT is the digital removal of the signal caused by the presence of iodine, known as Virtual Non-Contrast (VNC) or Virtual Unenhanced imaging (68, 102-105). VNC enables clinics to perform a single contrast-enhanced scan of a patient and produce a simulated non-contrast phase, which can help in efforts to lower patients' exposure to ionizing radiation and lower the costs associated with CT imaging. Vendors typically provide a non-contrast or water image as well as an iodine map either in units of mg Iodine/mL (General Electric, Philips) or the HU attributed to iodinated contrast (Siemens).

Many studies have been performed to assess the utility, image quality, and accuracy of virtual non-contrast images (103, 106-108). The resulting iodine maps have been used to differentiate between benign and malignant renal lesions (105, 109-112), identify metastatic disease in lymph nodes (113-116), and improve visualization of pancreatic (117, 118) and gynecological cancers (119). One common application of DECT virtual non-contrast imaging in neurology is the differentiation of hemorrhage from residual iodinated contrast agent following mechanical thrombectomy in patients with ischemic stroke (120-123).

Although these images may be useful clinically, there are disadvantages of which users must be aware. When choosing materials for virtual non-contrast image processing, vendors use iodine as the high-Z material in their processing algorithms and either one or two soft tissue-like materials (water, soft tissue, fat, etc.). Materials must be classified as a linear combination of these materials. Therefore, other high-Z materials such as calcium appear in both the virtual non-contrast and the iodine map provided by the vendors.

2.3.2 Virtual Monoenergetic Images

DECT data may also be used to create virtual monoenergetic images that simulate images acquired with a monoenergetic x-ray source (67, 92, 124-126). Users can reconstruct images at any energy between 40 keV and either 140 keV on GE systems or 190 keV on Siemens and Philips systems. To create these images, the density of the low-Z material (soft tissue or water) and iodine are calculated as detailed in section 2.2.2 for each voxel. Then, using the attenuation coefficient of each material, as defined by the National Institutes of Standards and Technology (NIST), is used in the following equation to estimate the total attenuation coefficient at the user-defined energy.

$$\mu_{total}(E) = \left(\frac{\mu}{\rho}\right)_L(E) \cdot \rho_L + \left(\frac{\mu}{\rho}\right)_H(E) \cdot \rho_H \quad \text{Equation 2.9}$$

2.3.3 Calcium Identification

Since calcium is a high Z material with a low K-edge, calcium can be readily identified using material decomposition, which is particularly useful because calcium and iodine can have very similar attenuation levels using SECT. DECT, therefore, enables more accurate removal of bony anatomy and removal of calcific plaques to improve visualization on CT angiography (84, 127, 128). Additionally, virtual calcium removal can lead to visualization of bone marrow edema in fractures that may otherwise be difficult to diagnose without MRI (89, 129-132). Material decompositions that incorporate calcium also enable quantitative estimates of calcium density, which have been utilized to estimate bone mineral density (133, 134).

2.3.4 Distinguishing Calcification and Hemorrhage

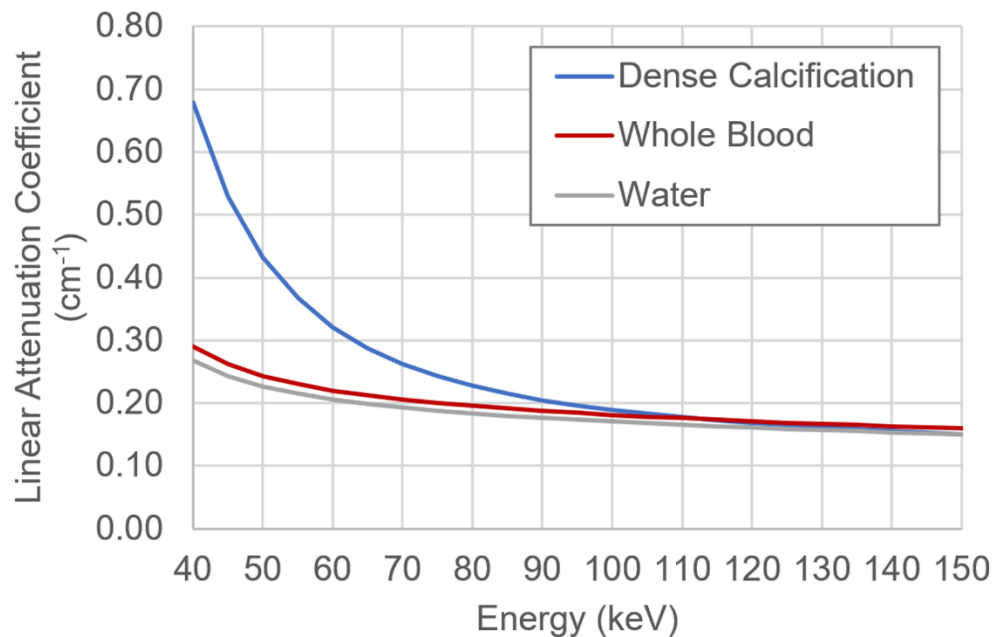


Figure 2.5: Attenuation curves for dense calcification (as modeled by low density cortical bone) and whole blood products. Note that blood products have a very similar curve shape as water with a slightly higher overall density.

There have been several studies published in the literature regarding the differentiation of intracranial calcification from hemorrhage (135-138). First were two phantom studies by Nute et al. demonstrating the feasibility of distinguishing these lesion types quantitatively using a calcium and water material decomposition on a fast kVp-switching system (135, 136). Both of these studies utilized an anthropomorphic head phantom and simulated calcific and hemorrhagic lesions by doping agarose (135) and brain attenuation-equivalent epoxy-resin (136) with calcium hydroxyapatite and iron oxide. Based on the attenuation curves for blood products and bone, the authors found that by using a decomposition of calcium and water, a plane of differentiation could be calculated that optimally separated the lesion types, as shown in Figure 2.6 (136). Differentiation was possible primarily using the water(calcium) images, in which hemorrhagic lesions would be iso- or hypo-intense, and calcific lesions would be hyperdense (Figure 2.7). Using this method, they found that differentiation was possible at

signal levels of 50 and 60 HU for 1.5cm and 1.0cm lesions in the cerebrum at 90% accuracy (136).

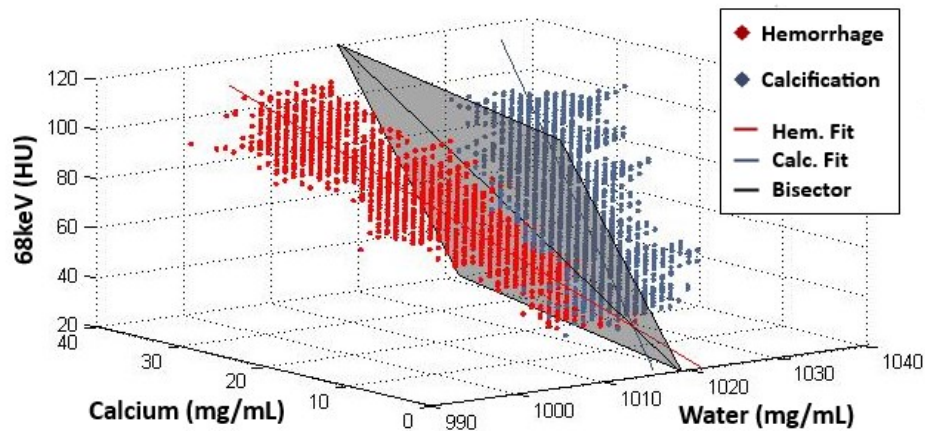


Figure 2.6: Example of a plane of differentiation developed with geometric bisectors for a 1.5cm diameter lesion in the cerebrum, imaged at 132.5 mGy and reconstructed at 5 mm image thickness with a soft filter. Voxel data for the hemorrhagic lesions are shown in red, while voxel data for the calcific lesions are shown in gray.

Lesion differentiation was also tested on a dual-source DECT system in an emergency department where all patients with suspected stroke underwent DECT imaging of the head (137). They found that a 3-material decomposition using calcium, brain tissue, and hemorrhage was capable of identifying calcific lesions because they were completely removed from the virtual non-calcium images while the signal in hemorrhagic lesions was visualized in both the calcium and soft tissue images. The authors confirmed the presence of hemorrhage on follow-up MRI and CT imaging (139). This technique, while not quantitative, had a sensitivity of 96% and specificity of 100% for the detection of hemorrhage (137).

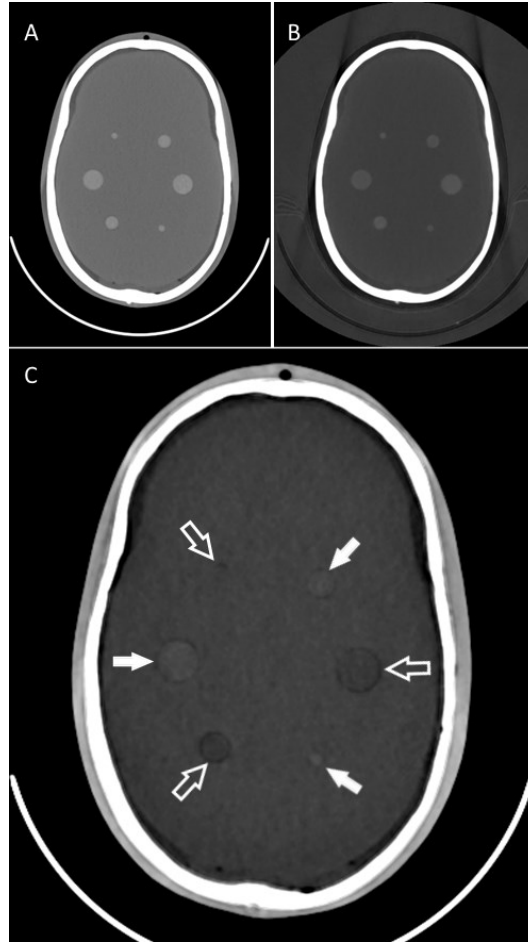


Figure 2.7: DECT reconstructions of a) 68 keV, b) calcium(water), and c) water(calcium) in a phantom image acquired at 132.6 mGy CTDIvol with 5 mm slice thickness and a soft reconstruction filter. Lesion models in the phantom were 80 HU at 120 kVp SECT. Solid arrows indicate calcific lesions while unfilled arrows identify iron-based lesion models.

2.4 Magnetic Susceptibility

Magnetic susceptibility is an inherent property of any material represented by a dimensionless scalar (χ). It represents the extent to which the material magnetizes when placed in a magnetic field, and is equal to the magnetization of the object divided by the magnetic field strength.

Ferromagnetism is a unique property of certain compounds in which the material remains magnetized after being removed from an external magnetic field caused by both the chemical make-up of the material and a particular crystal structure. Ferromagnets are the magnetic

materials most commonly encountered in daily life, but are not present naturally within the human body; the forms of magnetism that are naturally occurring in humans are described below.

2.4.1 Diamagnetism

Diamagnetic materials repel or weaken a magnetic field within a given material and have a negative magnetic susceptibility. Water ($\chi = -9.035 \times 10^{-6}$) and many tissues in the body are slightly diamagnetic (140). The most common usage of the term diamagnetic in the medical literature refers to materials with a susceptibility less than that of water, including calcium deposits (140-144).

2.4.2 Paramagnetism

Paramagnetic materials are also common within the human body. These materials have a positive susceptibility, so a magnetic field is locally strengthened in the material. For truly paramagnetic materials, the amount of magnetism is directly proportional to the strength of the applied field. Paramagnetism is caused by the spin of unpaired electrons within a material, and in total only a small portion of the spins orient with the field, so the effect is weak. Examples of materials that are paramagnetic relative to water are deoxyhemoglobin and iron deposits in the form of ferritin and hemosiderin.

2.4.3 Superparamagnetism

Superparamagnetism occurs in materials where very small individual paramagnetic particles each have an individual magnetic domain within a non-magnetic medium. These single domain particles each have their own magnetic moment, and together the total moment, when exposed to a magnetic field, is orders of magnitude higher than that of a typical paramagnet. The effect is present because materials with larger particles tend to form grains of magnetic materials that interact with each other and do not individually align with the applied magnetic field. One example of this phenomenon is superparamagnetic iron oxide nanoparticles (diameter < 30

nm), which have a much higher susceptibility for a given iron concentration than iron oxides with larger particles (145).

2.5 MRI Phase Basics

The Magnetic Resonance Imaging (MRI) data required to form an image comes from the spin precession of hydrogen nuclei, known as the Proton Resonance Frequency (PRF). To fully describe the location of the precessing spins, the data is acquired in quadrature, meaning that the signal acquired is acquired along two orthogonal directions (146, 147). The signal can be modeled as a complex number, where one channel is labeled “real” and the other “imaginary” (Figure 2.8).

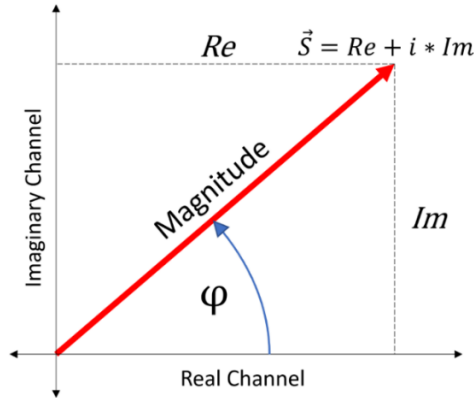


Figure 2.8: Diagrammed relationship between the MRI signal (S), the components measured in the real (Re) and imaginary (Im) channels, and the magnitude and phase of the signal.

The signal can also be expressed in the rotating frame of reference in terms of its magnitude, $|S|$, and phase angle, φ :

$$S = |S|e^{i\varphi} \quad \text{Equation 2.10}$$

The exact magnitude of the signal depends on the magnetic field strength, the pulse sequence used, and the following material properties: T_1 , T_2 , T_2^* , and proton density. The proton density is proportional to the number of hydrogen atoms in the voxel of interest. T_1 represents the rate at which longitudinal magnetization is regained following excitation into the transverse plane by an RF pulse. T_2 is the rate at which the transverse magnetization dephases based on nuclear

interactions only, whereas $T2^*$ is the observed relaxation rate when accounting for magnetic field inhomogeneities, and $T2'$ is proportional to the change in the local magnetic field at the inhomogeneity (Equation 2.11).

$$\frac{1}{T2^*} = \frac{1}{T2} + \frac{1}{T2'} \quad \text{Equation 2.11}$$

Phase is measured over the range of $[-\pi, \pi]$, so a true phase value of 2π would be mapped to a measured phase of 0. This results in an effect called phase wrapping, in which sharp boundaries in the phase image occur between a phase of $-\pi$ and $+\pi$, as depicted in Figure 2.9.



Figure 2.9: The MRI phase image displayed depicts phase wrapping at boundaries between $-\pi$ and π . Additionally, noise is amplified in low signal regions of the image.

2.5.1 Gradient Recalled Echo Pulse Sequences

Gradient recalled echo (GRE) pulse sequences are used when the application requires fast scanning or scanning of a large volume, including but not limited to perfusion, angiographic, and cardiac imaging. Following the initial RF excitation pulse, the free induction decay signal is rephased for readout using a gradient pulse. Spin echo sequences that utilize a 180° RF pulse to refocus the signal also refocus off-resonance effects caused by local magnetic field inhomogeneities (70, 146). GRE sequences cannot refocus these spins that are resonating off

of the expected frequency, and so these cause artifacts in the images. As a result of these off-resonance effects, GRE sequences are T2*-weighted rather than T2-weighted, and regions with differences in susceptibility relative to the background are emphasized because they change the local magnetic field. The echo time (TE), repetition time (TR), and flip angle (α) of the pulse sequence determines the exact weighting of the sequence, and the signal of a spoiled GRE is also dependent on the T1 and T2* of a material, and is adjusted by a scaling factor f :

$$S(TE) = f \frac{\sin \alpha (1 - e^{-TR/T1})}{(1 - \cos \alpha \cdot e^{-TR/T1})} e^{-TE/T2^*} \quad \text{Equation 2.12}$$

Despite the number of factors that impact the image weighting, TE is the primary factor that will influence the degree of T2* weighting in the final image, and lower TE images will feature higher SNR and fewer susceptibility artifacts than those images with higher TE.

2.5.2 Magnetic Susceptibility and MRI Phase

As described in section 2.4, paramagnetic and diamagnetic materials increase and decrease the magnetic field, respectively. The effective magnetic field (B_{eff}) is defined by the following equation, where B_0 is the strength of the main magnetic field, and $\Delta\chi$ is the difference in the susceptibility compared to that of the background (148).

$$B_{eff} = (1 + \Delta\chi)B_0 \quad \text{Equation 2.13}$$

The effective magnetic field in the region with differing susceptibility causes the spins to precess at a slightly different rate from the spins present in normal tissue. Therefore, at the TE in a GRE sequence—in which these spins are not rephased by a 180° RF pulse—there is an accumulation of phase in accordance to the following equation (148):

$$\varphi(t) = -\gamma B_0(TE + \Delta\chi) \quad \text{Equation 2.14}$$

The true phase can, therefore, be used to estimate the susceptibility of a lesion. However, there are confounding factors that must be accounted for to calculate the correct phase value

for a given voxel. First, phase wraps (Section 2.5) must be eliminated by one of various phase unwrapping algorithms, which becomes increasingly challenging as the number of spatial dimensions increases (149-151). Once phase wraps are successfully removed, the image is an estimate of the magnetic field perturbation (152). Additionally, there are background phase variations caused by non-local effects such as inhomogeneities in B_0 , large susceptibility differences (for example, air-tissue interfaces), and eddy currents (153, 154). The simplest method of removing the background phase is to use a high-pass filter to remove the low frequency components of the image (155, 156). Other methods have estimated the background phase using polynomial fitting (157-159), forward calculations using *a priori* knowledge of the background susceptibility distribution (160), and models of magnetic dipole sources outside of the region of interest (154) in attempts to model the phase more accurately.

2.6 Susceptibility-Weighted Imaging

Susceptibility-weighted imaging (SWI) is a technique for improving the visualization of veins and other high-susceptibility tissues (Figure 2.10). The method utilizes a background subtracted phase image to create an image mask, usually created by passing a high-pass filter over the phase image (161). Following background phase removal, the phase mask is created by scaling the phase using the following equation (162):

$$f(x) = \begin{cases} \frac{\pi + \varphi(x)}{\pi}, & -\pi < \varphi(x) < 0 \\ 1, & \text{otherwise} \end{cases} \quad \text{Equation 2.15}$$

where x specifies voxel location and $\varphi(x)$ is the phase at that location. The magnitude image $\rho(x)$ is utilized to create the susceptibility-weighted image $\hat{\rho}(x)$ according to the formula:

$$\hat{\rho}(x) = f^n(x) \cdot \rho(x) \quad \text{Equation 2.16}$$

In which n represents the number of times the phase mask is multiplied by itself, and is chosen to change the susceptibility weighting and optimize the signal to noise ratio (SNR) (161, 163). It has been shown that $n = 4$ provides an optimal balance between enhancing the image contrast of venous structures while maintaining SNR (164).

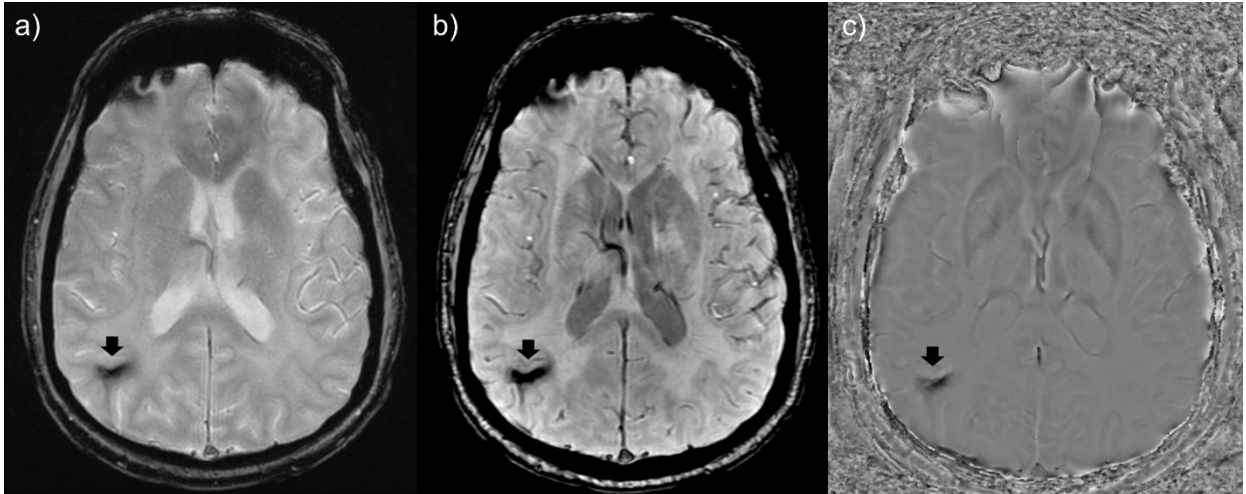


Figure 2.10: Susceptibility-weighted imaging (SWI) improves visualization of venous structures, as shown by comparison of a T2*-weighted GRE (a), Susceptibility-Weighted Angiography (b). The high-pass filtered phase image (c) from the SWAN sequence emphasizes the local magnetic field changes near the susceptibility lesion (black arrows).

The typical scaling of SWI does not differentiate between negative and positive phase accumulation. As a direct result, calcification and hemorrhage cannot be differentiated using the phase scaling in Equation 2.15. Other phase masks have been developed, such as a triangular mask that accounts for negative phase values (165); however, these are not commonly applied in SWI applications provided by MR vendors.

2.7 Quantitative Susceptibility Mapping

Quantitative Susceptibility Mapping (QSM) is an MRI phase-based post processing technique to reconstruct tomographic maps of magnetic susceptibility in tissue (148, 153, 162, 166). Following phase unwrapping and background phase removal, QSM solves an inverse problem, going from the measured magnetic field perturbation around a distribution of magnetic dipoles back to the susceptibility distribution that caused it (148). Because GRE pulse sequences are inherently sensitive to magnetic susceptibility, they are an obvious choice for QSM acquisitions. All QSM post-processing is vulnerable to noise in the phase images. High noise in the phase image is of particular concern in large hemorrhagic or calcific lesions where the signal is very

low, and thus noise is amplified significantly (Figure 2.9). As a result, multi-echo GRE sequences are most commonly used to acquire data for QSM processing because the phase can be calculated more accurately by assessing the temporal evolution of the phase as the TE changes, as shown in Figure 2.11 (152).

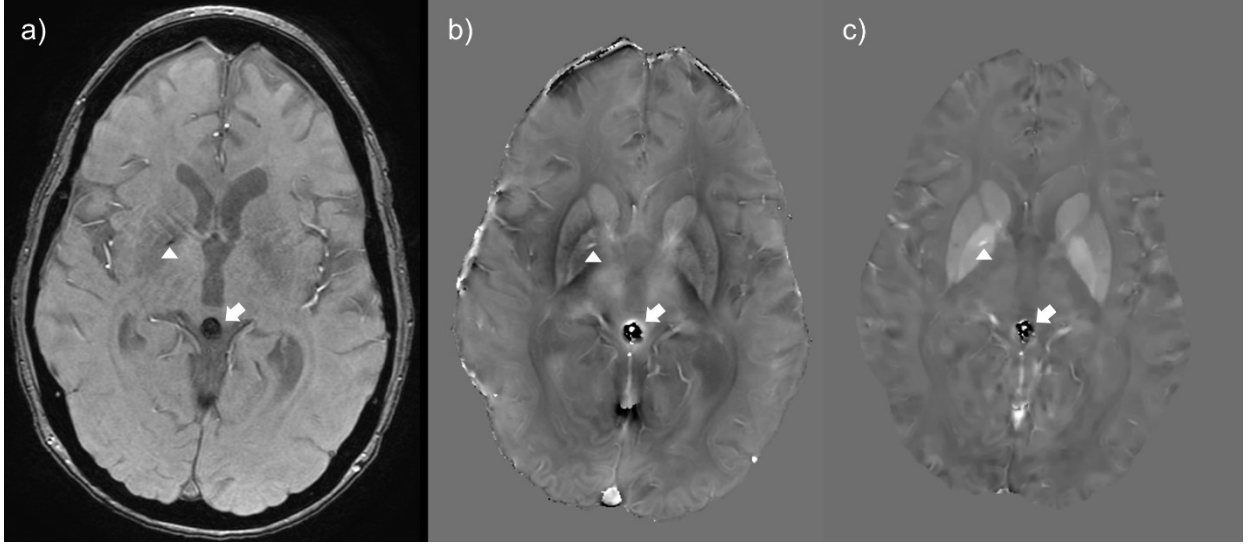


Figure 2.11: A multi-echo gradient recalled echo sequence (magnitude image, a) is used to generate a background subtracted phase image (b) and a Quantitative Susceptibility Map (c). Note the pineal calcification (arrow) and a punctate paramagnetic lesion in the globus pallidus (arrowhead) that both appear hypointense in the magnitude image and can be differentiated in the QSM.

2.7.1 Mathematical Derivation of the Inverse Problem

A predefined magnetization distribution $\vec{M}(\vec{r})$, which is proportional to the distribution of the magnetic susceptibility, induces a magnetic field variation $\Delta\vec{B}(\vec{r})$, that is equal to

$$\Delta\vec{B}(\vec{r}) = \frac{\mu_0}{4\pi} \int_V \left\{ \frac{3\vec{M}(\vec{r}')(\vec{r} - \vec{r}')^2}{|\vec{r} - \vec{r}'|^5} - \frac{\vec{M}(\vec{r}')}{|\vec{r} - \vec{r}'|^3} \right\} d^3(\vec{r}') \quad \text{Equation 2.17}$$

where \vec{r} represents coordinates in Cartesian space and μ_0 represents the magnetic permeability in free space. We can assume that the main magnetic field resides solely in the z direction, so Equation 2.17 simplifies to:

$$\Delta B_z(\vec{r}) = \frac{\mu_0}{4\pi} \int_V \left\{ \frac{3M_z(\vec{r}')(z-z')^2}{|\vec{r}-\vec{r}'|^5} - \frac{M_z(\vec{r}')}{|\vec{r}-\vec{r}'|^3} \right\} d^3(\vec{r}') \quad \text{Equation 2.18}$$

where $\Delta B_z(\vec{r})$ is the magnetic field variation along the z-axis. Equation 2.18 can be represented as a convolution of the magnetization distribution with the magnetic dipole kernel, $\vec{D}(\vec{r})$.

$$\begin{aligned} \Delta B_z(\vec{r}) &= \mu_0 M_z(\vec{r}) * D(\vec{r}) \\ &= \mu_0 M_z(\vec{r}) * \left[\frac{1}{4\pi} \frac{3 \cos^2 \theta - 1}{r^3} \right] \end{aligned} \quad \text{Equation 2.19}$$

From this point, we assume that the susceptibility at any given point is sufficiently small to assume that $M_z(\vec{r}) \approx B_0 \chi(\vec{r}) / \mu_0$. The problem is better posed in the frequency domain (k-space), so the Fourier transform is taken ($D(\vec{k}) = FT\{D(\vec{r})\}$), and the convolution theorem is applied to Equation 2.19, returning the desired inverse problem, in which \vec{k} represents a vector in frequency space and k_z is the z-component of the vector.

$$\Delta B_z(\vec{k}) = B_0 \chi(\vec{k}) \times D(\vec{k}) \quad \text{Equation 2.20}$$

$$D(\vec{k}) = \frac{1}{3} - \frac{k_z^2}{|\vec{k}|^2} \quad \text{Equation 2.21}$$

Since $\Delta B_z(\vec{r})$ is measured and the remaining quantities are known, the inverse problem can be solved to calculate the distribution of $\chi(\vec{r})$. However, in k-space, the dipole moment (Equation 2.21) is equal to zero along a cone at an angle of 54.7° (hence known as the “zero cone”), and therefore the problem is ill-posed (152, 153, 167-169).

2.7.2 QSM Methods

Because solving for the susceptibility distribution is ill-posed, many methods have been implemented to correct for the streak artifacts that would otherwise be induced by the zeros in the dipole moment. The gold standard for accurately measuring the susceptibility is “Calculation Of Susceptibility through Multiple Orientation Sampling,” or COSMOS (170-172).

The COSMOS technique requires multiple acquisitions of GRE data with the sample in different orientations to effectively average out the effect of the zero cone, ensuring that no point in k-space is filled with zeros. Thus, the inverse problem can be solved directly. This method is highly accurate but time consuming and difficult for many body regions outside of the extremities and the head.

Because of the logistical constraints of implementing COSMOS for QSM measurements *in vivo*, multiple processing methods have been developed that utilize a single GRE acquisition to estimate the susceptibility. What these methods have in common is that they utilize some form of regularization. The first of these methods is Thresholded K-space Division (TKD), in which very small or zero values in the dipole kernel are replaced with a constant (173-176). This method reduces streaking artifacts caused by the zero cone, but it can induce artifacts elsewhere in the image if phase shifts are not caused by susceptibility.

Several methods use iterative computational techniques to calculate a solution to the inverse problem. The difference between the measured magnetic field and the convolution of the dipole moment and calculated susceptibility distribution is computed first. The end goal is to minimize the sum of the L2 norm of this difference and a regularized prior information term. The prior information completes the missing data in k-space. Other similar techniques include using a sparse linear equation and least squares (LSQR) approach (177, 178), piecewise constant regularization (157), non-linear regularization of the susceptibility gradients (179, 180), and methods requiring anatomical or morphological agreement (167, 181). Morphology-Enabled Dipole Inversion (MEDI) is the most prominent QSM method using this scheme. The prior information in MEDI is taken from the magnitude images, and edges in the magnitude image are assumed to correspond with true edges in the calculated susceptibility map (167, 182, 183). Disadvantages of this technique include mismatches in the calculated susceptibility

values where the anatomic edges and edges in the true susceptibility distribution do not match (152).

A final group of algorithms only fills in ill-conditioned k-space data rather than using prior information to inform the whole dataset. These methods split k-space into various subdomains, and the ill-conditioned portions are reconstructed separately from the other domains. The susceptibility distribution is optimized subject to either a sparse L1 norm or total variation norm (152). The Homogeneity-Enabled Incremental Dipole Inversion (HEIDI) technique is one particular example of this subdomain-based QSM method (184). These methods tend to be quite accurate when compared to COSMOS and eliminate streak artifacts effectively (184).

2.7.3 QSM Applications

The primary sources of susceptibility in human tissues are iron, calcium, lipids, and myelin (140, 185). While there has not been an investigation to date using QSM to quantify the fat content of tissues since other methodologies, such as the Dixon method, have proven accurate in this area, diseases that cause myelin degeneration, dysregulation of iron metabolism, and diseases featuring calcifications have been studied using QSM.

Myelin sheaths cover the axons of nerves to insulate them from outside electrical currents. In diseases such as multiple sclerosis (MS) and amyotrophic lateral sclerosis (ALS), demyelination of nerves in gray matter and the spinal cord is a clinical feature of the disease (186, 187). Cancer treatment with cranial radiation is also a common cause of demyelination of brain tissue, and has been shown to cause changes in normal-appearing white matter (188, 189). Myelin is diamagnetic compared to water due to its high phospholipid content, and so susceptibility will increase as demyelination occurs. This increase in magnetic susceptibility has been observed in several studies using QSM (190, 191).

Iron-containing lesions, such as hemorrhage (see section 2.1.1) (192-194), cerebral microbleeds (184, 195, 196), traumatic brain injury (196, 197), and chronic MS lesions (190, 191, 198, 199), have been the primary diagnostic targets of QSM to date. These lesions are highly paramagnetic compared to water, so they have improved the ability of clinicians to identify them and quantify disease progression. Deep gray matter also has very high iron content, so QSM improves the anatomic visualization of tissues within the basal ganglia (putamen, globus pallidus, and choroid plexus), thalamus, red nucleus, and dentate nucleus (184, 192, 200-203).

Calcifications, often composed of hydroxyapatite ($\chi = -14.83$ ppm), are also prominent in various diseases (see section 2.1.2) (140, 204). QSM provides differentiation of calcific and hemorrhagic lesions in agreement with conventional SECT (45, 205, 206), and has improved the visualization of calcifications compared to methods utilizing background corrected phase images from T2*-weighted GRE (142) and susceptibility-weighted imaging sequences (207, 208). To date, the ability of QSM to identify calcifications below 100 HU on SECT has not been studied.

Lesion Differentiation in Magnetic Resonance Imaging Phantoms

3.1 Introduction

The differentiation of intracranial calcifications and hemorrhage using imaging is of critical importance to patient diagnosis and care. In particular, low density lesions that fall below 100 Hounsfield Units (HU) on conventional Single-Energy Computed Tomography (SECT) are of interest to researchers because the signal level of hemorrhage and low-density calcifications overlaps within this range. Multi-echo T2*-weighted GRE sequences are highly sensitive to hemorrhage, but the characterization is challenging because calcifications also appear as black spots due to their inherent magnetic susceptibility. Techniques that utilize the complex phase data from a GRE acquisition, known as Phase-Sensitive Magnetic Resonance Imaging (PS-MRI) methods, have been utilized in clinical research studies to differentiate calcific and hemorrhagic lesions *in vivo* successfully. However, the *in vivo* studies currently available in the literature relied on a SECT threshold to determine if a lesion was calcific, which is not an adequate gold standard for low density lesions (45, 205, 206). To circumvent this issue, we have developed multiple agarose-based phantoms to use as a gold standard comparison for *in vivo* studies.

Multiple studies in the literature have examined the use of parametric MRI for identifying calcific and hemorrhagic lesions on T2* maps. A study published in Radiology by Langkammer et al. demonstrated that R2*-mapping ($R2^* = 1/T2^*$) had a high correlation with iron content in the brains of human cadavers (209). They found that the iron concentration in gray matter tissues, including the globus pallidus, putamen, caudate nucleus, and thalamus, ranged from 49 to 205 mg iron/kg of wet mass (209). These iron levels corresponded to T2* range of 13.8 to 33.3 ms

in these iron-laden normal tissues. In another study, 52 patients experiencing symptoms of Parkinson’s disease, brain iron—frequently elevated in these patients—was highly correlated with T2* parametric maps, and the T2* ranged from approximately 15 ms to 35 ms (210). Within cavernomas suspected of bleeds, the T2* was as low as approximately 7.7 ms (211). Roy et al. found that calcified neurocysticercosis lesions had a median T2* of 14.6 ms for lesions with a 120 kVp SECT attenuation of 142.10 HU (212).

Based on these literature values, we qualitatively and quantitatively verified that the phantom materials generated the expected MR signal decay curves with minimal image artifacts and finally constructed several MR phantoms with calcific and hemorrhagic lesion models within biological constraints.

3.2 Methods

3.2.1 MRI Phantom Materials

Many materials have been used in the literature to simulate calcific and hemorrhagic lesions. Based on the literature and prior experience making agarose-based phantoms (136), we chose to model calcification and hemorrhage using the materials listed in Table 3.1.

Table 3.1: Phantom materials simulating calcific and hemorrhagic lesions

Calcification Models	Iron Models
Hydroxyapatite (136, 213)	Iron(III) Oxide (214)
Calcium Chloride (215)	Iron(II) Chloride (193)
	Iron(III) Chloride (193, 211)
	Iron Dextran (216, 217)
	Hemoglobin (211)

The materials, with the exception of hemoglobin, were suspended in 1% weight/volume agarose gel (#0710; Amresco, Solon, OH) within cylindrical, plastic 1.8ml cryovials (#375418;

Thermo Scientific, Waltham, MA). The hydroxyapatite (#289396; Sigma-Aldrich, St. Louis, MO) and iron(III) oxide (#529311; Sigma-Aldrich) required emulsification in 0.01% Triton X (#112K09721; Sigma Aldrich) with a magnetic stir bar overnight. Following emulsification, the agarose was added, and the vials were agitated manually to ensure the uniform distribution of material (136). Hemoglobin was dissolved in sterile Lactated Ringer's solution (#07-19-75-231; Baxter, Deerfield, IL) to reach physiologic concentrations.

The phantom background material was comprised of LB Agar Miller (#1102830500; Millipore Sigma, Darmstadt, Germany) at a concentration of 3.7% weight/volume. This material provides physical strength, the flexibility to choose the orientation of the phantom relative to the main magnetic field and is reasonably tissue equivalent due to its protein and sodium chloride content.

3.2.2 MRI Phantom Design

There were several aspects of the MRI phantom design to be considered before construction of the phantom. First, a plastic container with a low magnetic susceptibility was required. Second, the vials had to be held parallel to each other within the background medium and be sufficiently far from the edges of the phantom to minimize the effect of signal loss at the air-phantom boundary. With these concerns in mind, two phantom designs were created.

Preliminary Phantom Design

The preliminary phantom design utilized a 12 cm x 12 cm test tube rack made of polypropylene for gel placement. Holes were drilled in the bottom of the test tube rack to enable removal of the vials. The tops of thirteen vials were wrapped in Parafilm M (P 7793; Sigma Aldrich, St. Louis, MO) and inserted into the test tube rack (Figure 3.1a). The agarose background was prepared and poured into a heat-safe polypropylene storage container with dimensions of 15.6 cm x 15.6 cm x 8.6 cm (Ziploc Medium Square Container, SC Johnson, Racine, WI) and allowed to cool to a temperature of 50°C. The test tube rack was then inverted and placed in

the container so that the vials were immersed in the agarose. The phantom was then stored at 4°C overnight to allow the agarose to set, and the test tube rack was removed, using a toothpick to release the vials from the test tube rack. Phantoms utilizing this design had abbreviations beginning with “P” to indicate the use of the preliminary design.

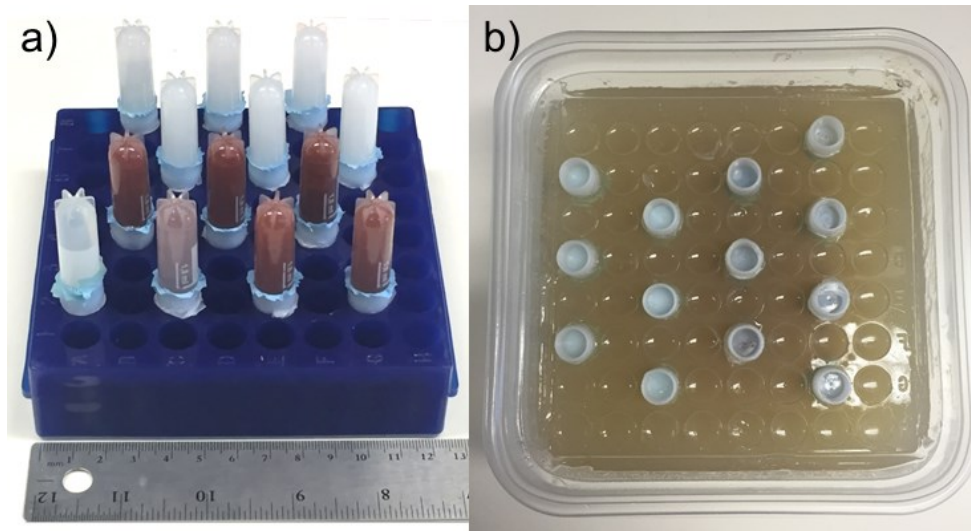


Figure 3.1: Preliminary phantom design demonstrating the vial positioning in the test tube holder (a) and the completed preliminary phantom (b) with the agarose background.

Round Phantom Design

The preliminary phantom design allowed for a maximum of twelve samples and one control. Additionally, using an existing test tube holder did not allow for even spacing of the vials within the phantom or the ability to position all vials away from the phantom edge. Therefore, a second design was conceived to alleviate these problems.

A 16-cm diameter, round, heat safe, polypropylene container (Large Bowl Food Storage Container, H-E-B, San Antonio, TX) was chosen for the phantom. The phantom was designed with a 2-cm buffer between individual samples. There was also greater than 2 cm between the outer ring of vials and the phantom edge to minimize signal loss from the air-phantom boundary. A total of nineteen samples fit within the container. A schematic of the phantom

design is shown in Figure 3.2. A custom test-phantom template to hold the vials in place was made from 1/8" craft plywood (Michaels, Irving, TX). Phantoms with this design were abbreviated "R" for round phantom.

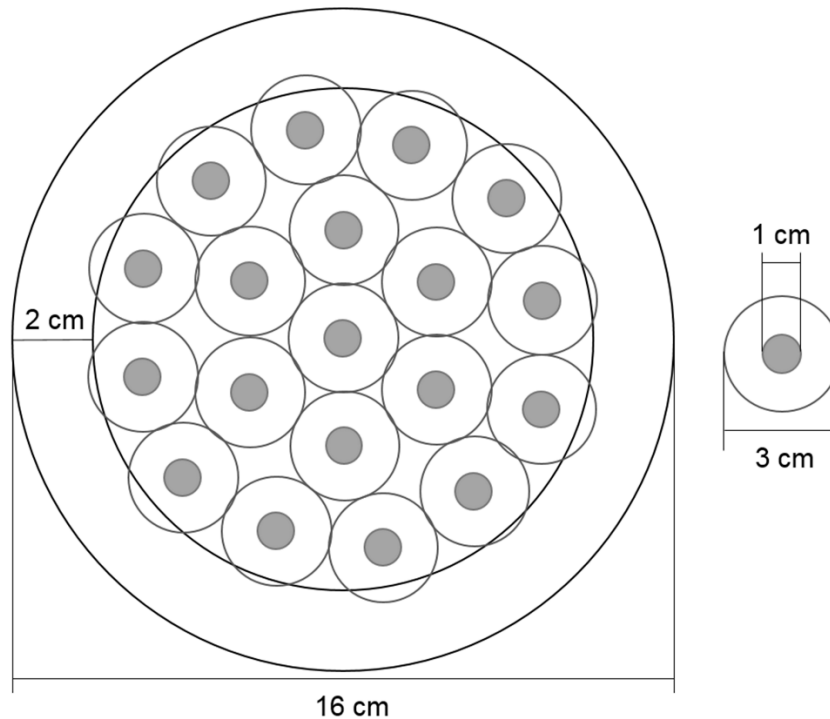


Figure 3.2: Schematic of the round phantom design. The cryovials measure 1 cm in diameter, and all vials were greater than 2 cm from the edge of the phantom and 2 cm away from all other vials.

3.2.3 Material Validation Phantoms

Hydroxyapatite and Iron (III) Oxide (P1 & P2)

Several phantoms were made to validate the materials used in each phantom. The preliminary phantom design was used to create two phantoms that each contained six hydroxyapatite vials and six iron(III) oxide vials. The goal of these phantoms was to test calcific and hemorrhagic lesion models that had the same SECT HU value, as calculated using the equations presented in Nute et al. (135). Low HU samples were grouped in one phantom (Figure 3.3a) while high HU samples were placed in the second phantom (Figure 3.3b). The material concentrations for the desired SECT HU are shown in Table 3.2.

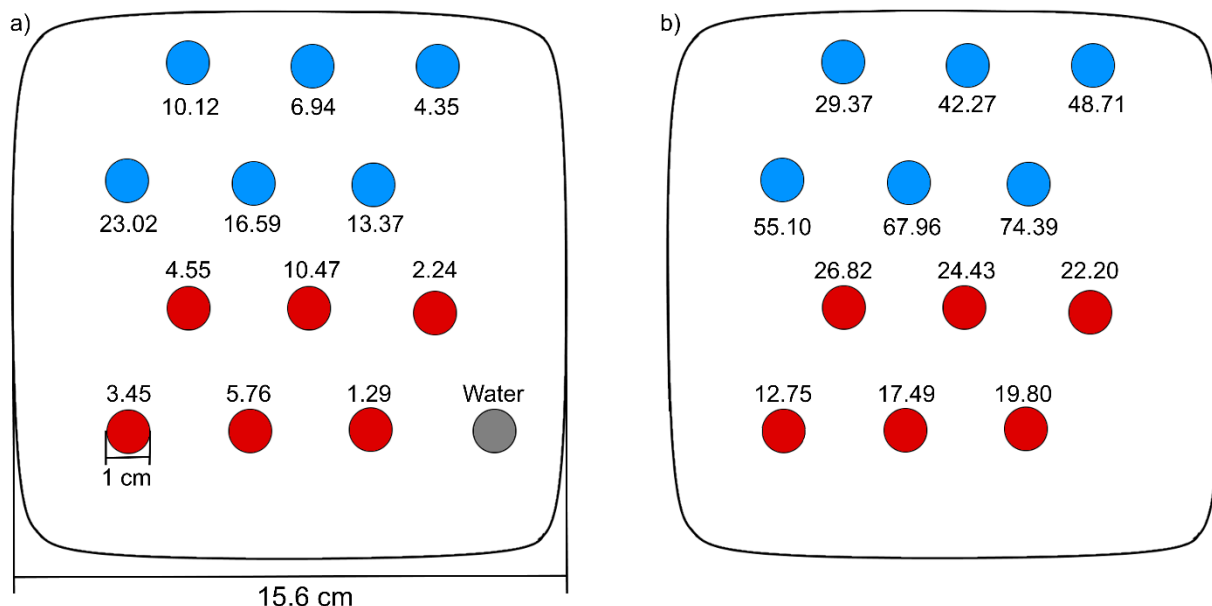


Figure 3.3: Iron oxide and hydroxyapatite phantoms a) P1, with low concentrations, and b) P2 with high concentrations of the two materials. The concentrations displayed here are in mg of analyte per mL.

Table 3.2: Hydroxyapatite and Iron(III) Oxide sample specifications for both low and high concentrations.

Phantom	Predicted SECT (HU)	Iron(III) Oxide Concentration (mg/mL)	Hydroxyapatite Concentration (mg/mL)
Low Concentration Phantom (P1)	1	1.29	4.35
	5	2.24	6.94
	10	3.45	10.12
	15	4.55	13.37
	20	5.76	16.59
	35	10.47	23.02
High Concentration Phantom (P2)	40	12.75	29.37
	60	17.49	42.27
	70	19.80	48.71
	80	22.20	55.10
	100	24.43	67.96
	110	26.82	74.39

Hydroxyapatite and Iron Dextran (R1 & R2)

A hydroxyapatite and iron dextran (INFeD; Allergan, Dublin, Ireland) phantom was made with the round phantom design, containing nine hydroxyapatite gels, nine iron dextran gels, and a vial of Milli-Q water (Millipore Sigma). A 2-mL vial of iron dextran (50 mg iron/mL) was scanned in air using SECT (HD750 CT; General Electric Healthcare, Waukesha, WI) to estimate the HU before making the dilutions. The concentrations of each material used in the phantom are given in Table 3.3. The SECT signal was approximately matched between the iron dextran and hydroxyapatite gels to test the feasibility of using the same concentrations of iron dextran for both CT and MRI lesion modeling. A schematic of the phantom is shown in Figure 3.4.

Table 3.3: Hydroxyapatite and Iron Dextran gel specifications and their estimated SECT attenuation in HU for the first iron dextran testing. This phantom had approximately matched SECT HU between the iron dextran and hydroxyapatite gels.

Phantom	Iron Dextran Concentration (mg iron/mL)	Iron Dextran Estimated SECT HU	Hydroxyapatite Concentration (mg/mL)	Hydroxyapatite Estimated SECT HU
Approximately-Matched SECT HU (R1)	0.59	5	13.22	20
	1.77	15	24.82	40
	3.54	30	42.24	70
	5.89	50	48.00	80
	8.25	70	59.53	100
	10.61	90	74.16	125
	11.79	100	117.61	200
	14.15	120	146.51	250
	32.41	255	194.24	350

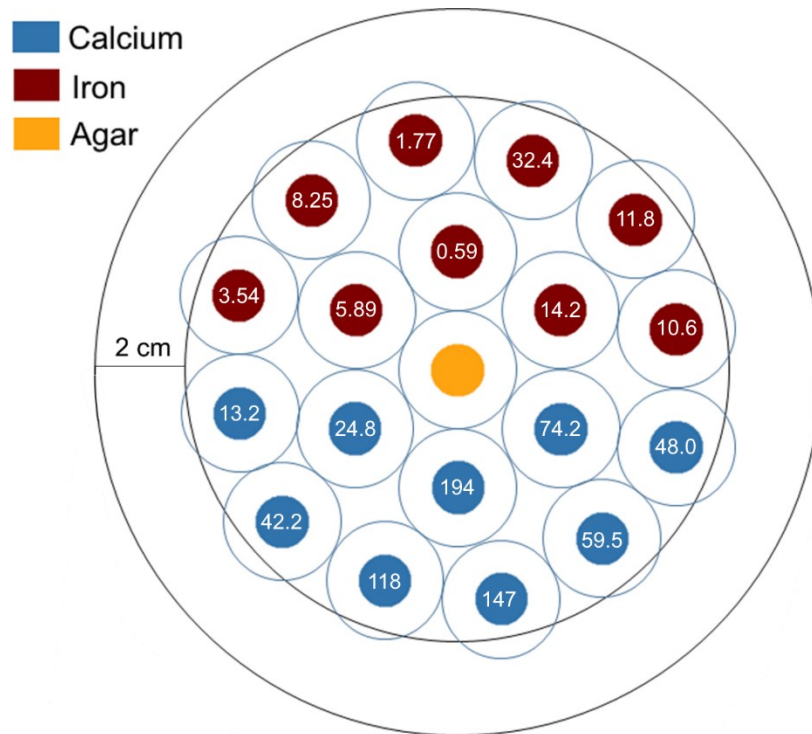


Figure 3.4: Diagram of the phantom R1. Hydroxyapatite is shown in blue, iron dextran in red, and 1% w/v agarose in gold. The numbers refer to the concentration of material in each vial (iron dextran in units of mg Fe/mL, hydroxyapatite in mg/mL).

Following the scanning of phantom R1, another hydroxyapatite and iron dextran phantom (R2) was developed which limited the iron concentration to avoid inducing chemical shift artifact (Table 3.4, Figure 3.5). As a result, the SECT attenuation was not matched between the calcific and hemorrhagic lesion models in phantom R2.

Table 3.4: Hydroxyapatite and Iron Dextran gel specifications for a second phantom. In this instance, SECT HU was not matched between the calcium and iron gels.

Phantom	Iron Dextran Concentration (mg iron/mL)	Hydroxyapatite Concentration (mg/mL)
Limited Iron Concentrations (R2)	0.4	7.8
	0.8	15.7
	1.2	23.5
	1.6	31.4
	2	39.2
	2.4	58.8
	2.8	78.4
	3.2	137.3
	3.6	196.1

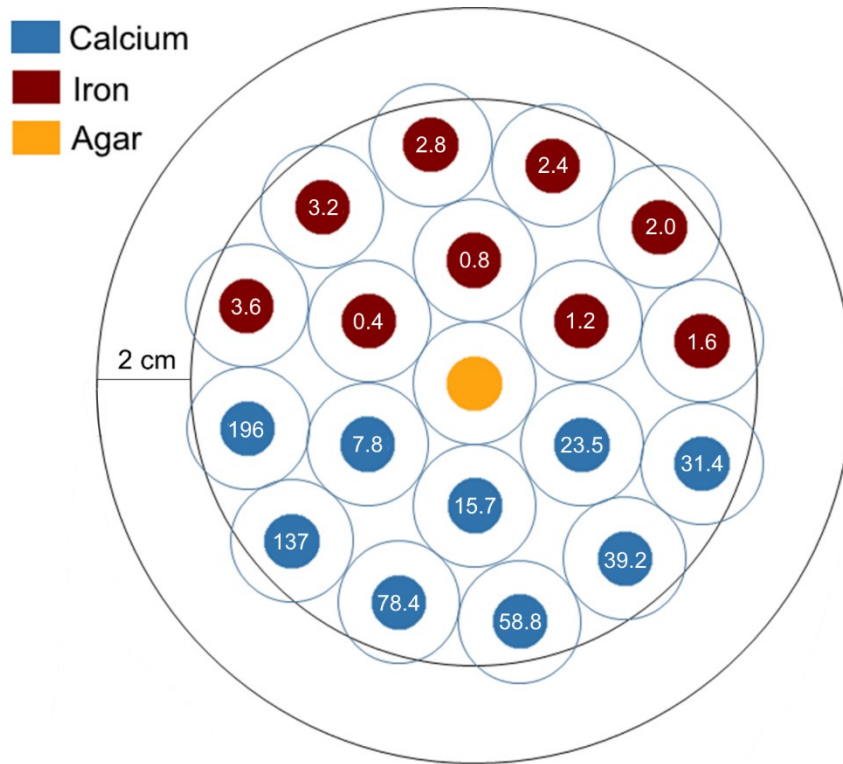


Figure 3.5: Phantom R2 with adjusted iron dextran and hydroxyapatite concentrations. Iron dextran concentration values in the diagram are given in mg Fe/mL while hydroxyapatite concentrations are given in mg/mL.

Hydroxyapatite and Calcium Chloride (R3)

Having a calcific substance that is soluble in water would improve the uniformity of the phantom materials and potentially enable the use of higher concentrations of calcium to model materials with more negative magnetic susceptibilities. A potential material was determined to be calcium chloride, which had been used to make alginate gel beads in another MRI phantom experiment (215). Serial dilutions of calcium chloride (CaCl_2) in 1% w/v agarose (2.0, 1.0, 0.5, 0.25, 0.1, and 0.05 M) were prepared along with nine hydroxyapatite gels (13.2, 24.8, 42.2, 48.0, 59.5, 74.2, 117.6, 146.5, and 194.2 mg/mL) and two iron dextran gels (1.77 and 5.89 mg iron/mL) for reference. This phantom will be abbreviated as R3.

Iron(II) Chloride and Iron(III) Chloride (R4)

The magnetic susceptibility of a compound depends primarily on the number of unpaired electrons present in the molecule (140, 204). While oxyhemoglobin has no unpaired electrons, deoxyhemoglobin has four unpaired electrons, and methemoglobin has five (204). The heme iron must be in the 2+ state to bind oxygen, at which point it is oxidized to the 3+ state (218, 219). The goal of this phantom was to determine whether it was necessary to account for the iron valence state to model the hemorrhagic lesions seen clinically. A 10 mg iron/mL stock solution of FeCl_2 (#50-901-14656; Fisher Scientific, Waltham, MA) was prepared in a 1% L-ascorbic acid (#255564, Sigma Aldrich) buffer to ensure the iron remained in the 2+ valence state. The FeCl_3 stock was also prepared to a concentration of 10 mg iron/mL in MilliQ water. 1% agarose was added to dilute the solutions to the following concentrations: 0.0, 0.2, 0.4, 0.6, 0.8, 1.0, 1.2, 1.4, and 1.6 mg iron/mL. The vials were then arranged according to the round phantom design

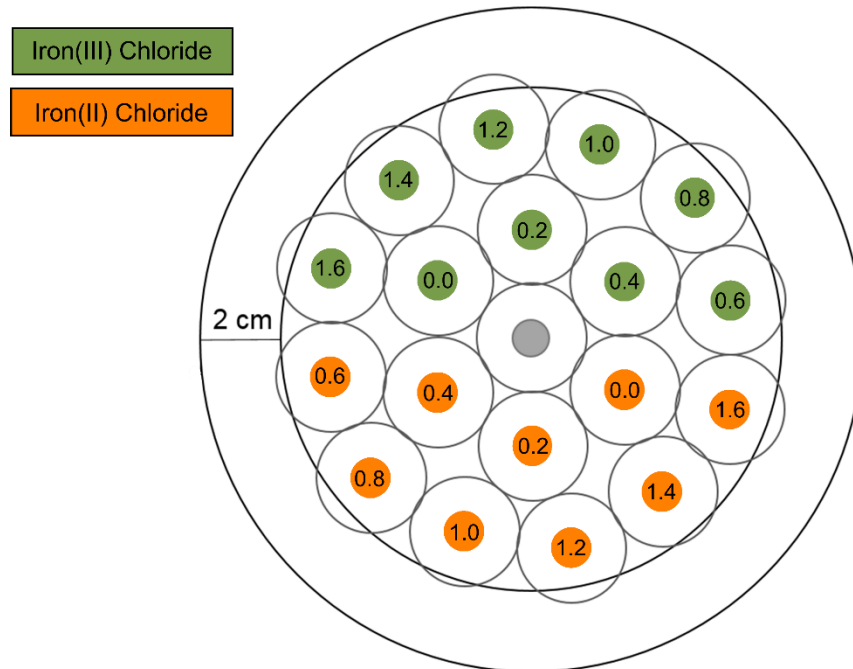


Figure 3.6: Phantom R4 arrangement of iron(III) and iron(II) chloride samples. Units are given in mg Fe/mL.

Biological Calibration Phantom (RF1)

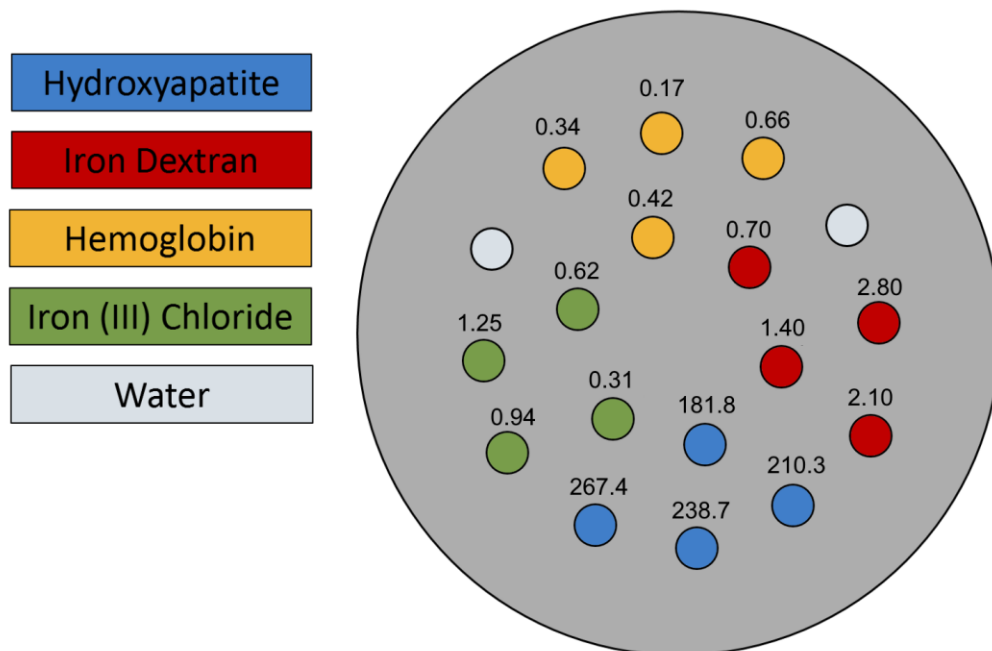


Figure 3.7: Phantom RF1, a calibration phantom, featuring hydroxyapatite, iron dextran, hemoglobin, and iron(III) chloride. The numbers above the vials refer to the concentration in units of mg/mL for hydroxyapatite and mg Fe/mL otherwise.

The goal of this phantom was to provide calibration curves over a biological range of T2* values for calcifications and several iron-based compounds. Four vials each of hydroxyapatite, iron dextran, iron(III) chloride, and hemoglobin (in Lactated Ringer's solution) were made to the specifications listed in Table 3.5. The vials were placed in the phantom as depicted in Figure 3.7. The phantom abbreviation used was RF1 to indicate that it was one of the round finalized phantoms to be used in a future analysis (see Chapter 4).

Table 3.5: Specifications for concentrations of hydroxyapatite, iron dextran, iron(III) chloride, and hemoglobin to be included in finalized calibration curves. Iron dextran concentration is given in mg iron/mL due to the lack of a nominal density for the dextran complex as a whole. Hemoglobin was assumed to be 0.31% iron per sample specifications.

Hydroxyapatite (mg/mL)	Iron Dextran (mg Fe/mL)	Iron(III) Chloride (mg Fe/mL)	Hemoglobin (mg Fe/mL)
181.8	0.70	0.31	0.17
210.3	1.40	0.62	0.34
238.7	2.10	0.94	0.42
267.4	2.80	1.25	0.66

This phantom was scanned three times to test the repeatability of the MR results.

Biological Phantom with Mixed Materials (RF2)

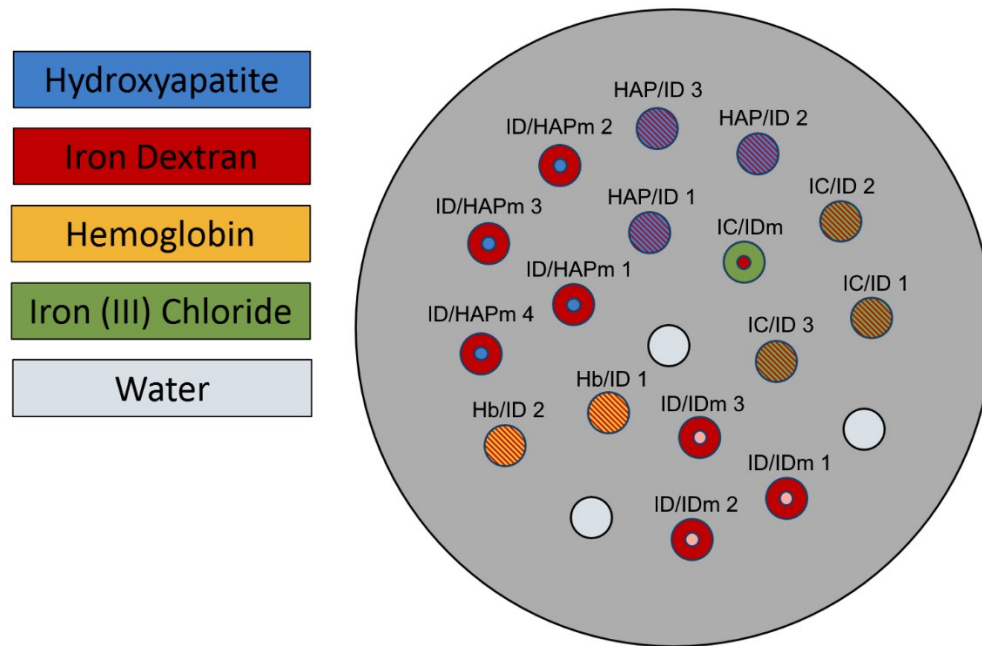


Figure 3.8: Diagram of the biological phantom with mixed materials. Lesion models with diagonal stripes represent mixtures while vials with smaller spots represent regions of differing material and concentration within a uniform background.

A final phantom (RF2) with a variety of mixed lesions was created to assess the feasibility of identifying both mixtures of materials and smaller regions of differing susceptibility within a larger lesion. In total, eight mixtures were made with iron dextran and one other material—hydroxyapatite, iron(III) chloride, or lyophilized human hemoglobin—evenly distributed throughout a 2% agarose background (Table 3.6). Eight additional lesion models were created with simulated regions of a different material or material concentration, hence referred to as “masses.” To manufacture the vials containing masses, several vials of hydroxyapatite and iron dextran (concentrations found in Table 3.6) were created with a 5% w/v agarose background to ensure structural integrity. Then a 5-mm Miltex standard biopsy punch (#3334; Integra LifeSciences, Plainsboro, NJ) was used to remove a cylindrical piece of the gel approximately 3/8” deep. Agarose with the chosen background material was prepared at a concentration of 2% w/v and the cylindrical mass was gently inserted into the vial with a metal spatula before

the agarose was set. A schematic of the vial placement within the phantom is provided in Figure 3.8. This phantom was scanned three times to test the repeatability of the MR results.

Table 3.6: Agarose gel composition for a biological phantom with mixed materials. For the lesions with masses (“Mass”), Material 1 indicates the composition of the uniform background material while Material 2 indicates the concentration within the mass. Concentrations are reported in mg Fe/mL for iron containing compounds and mg/mL for hydroxyapatite

Label	Type	Material 1	Material 1 Concentration (mg Fe/mL OR mg/mL)	Material 2	Material 2 Concentration (mg Fe/mL OR mg/mL)
HAP/ID 1	Mixture	Hydroxyapatite	210.2	Iron Dextran	2.10
HAP/ID 2	Mixture	Hydroxyapatite	210.2	Iron Dextran	1.40
HAP/ID 3	Mixture	Hydroxyapatite	210.2	Iron Dextran	0.70
IC/ID 1	Mixture	Iron(III) Chloride	0.47	Iron Dextran	0.35
IC/ID 2	Mixture	Iron(III) Chloride	0.31	Iron Dextran	0.70
IC/ID 3	Mixture	Iron(III) Chloride	0.16	Iron Dextran	1.05
Hb/ID 1	Mixture	Hemoglobin	0.34	Iron Dextran	0.70
Hb/ID 2	Mixture	Hemoglobin	0.17	Iron Dextran	1.05
ID/HAPm 1	Mass	Iron Dextran	0.70	Hydroxyapatite	267.1
ID/HAPm 2	Mass	Iron Dextran	0.70	Hydroxyapatite	181.6
ID/HAPm 3	Mass	Iron Dextran	2.10	Hydroxyapatite	267.1
ID/HAPm 4	Mass	Iron Dextran	2.10	Hydroxyapatite	181.6
IC/IDm	Mass	Iron(III) Chloride	0.31	Iron Dextran	0.70
ID/IDm 1	Mass	Iron Dextran	1.40	Iron Dextran	0.70
ID/IDm 2	Mass	Iron Dextran	0.70	Iron Dextran	1.40
ID/IDm 3	Mass	Iron Dextran	0.70	Iron Dextran	2.80

3.2.4 MRI Scan Protocol

All phantom imaging was performed on a 3.0-T MRI system (MR 750, General Electric Healthcare) with an 8-channel head coil. The phantom was positioned with the vials parallel to B_0 to minimize blooming. A three-dimensional (3D) T1-weighted ultrafast gradient echo with magnetization preparation (IR-FSPGR) was acquired to assess geometric accuracy near the vials. A T2*-weighted GRE was acquired for comparison of the signal level in the phantom to conventional clinical images. 3D susceptibility-weighted angiography (SWAN) sequence was acquired to examine the background phase—which is automatically reconstructed—in each

material (see Chapter 4). Finally, a 3D multi-echo fast gradient recalled echo (MFGRE) was acquired to assess signal changes with increasing echo time (TE) and calculate T2*, an inherent property of a material indicating the time required for signal dephasing caused by magnetic field inhomogeneity (for example, those caused by magnetic susceptibility) to occur. Protocol details are shown in Table 3.7.

Table 3.7: MRI acquisition details for all phantom experiments, including repetition time (TR), inversion time (TI), receive bandwidth (BW), field-of-view (FOV), acquisition matrix

Sequence	IR-FSPGR	T2*-weighted GRE	3D SWAN	3D MFGRE
<i># of Echo Times</i>	1	1	6	12
<i>TE (ms) [min, max]</i>	2.1	15	23.3 ^a	[4.7, 61.4]
<i>TR (ms)</i>	5.7	600	37.6	65.2
<i>TI (ms)</i>	400	-	-	-
<i>Flip Angle</i>	20°	20°	15°	20°
<i>BW (kHz)</i>	128	128	128	128
<i>FOV (mm)</i>	220	220	220	220
<i>Phase FOV (% of FOV)</i>	80	75	80	80
<i>Matrix</i>	256 x 256	256 x 256	320 x 224	416 x 320
<i>Slice Thickness (mm)</i>	1.4	5	1.4	1.4
<i>Scan Time</i>	4:27	2:00	2:49	6:46

^a SWAN provides images that are a weighted average of the six echoes. The average TE is listed here.

SECT was also acquired to determine the conventional CT attenuation level of the vials within the phantom and to ensure gel uniformity. All scanning was performed with our institution's routine brain protocol. DECT was also acquired for phantoms with matched SECT HU (Hydroxyapatite and Iron Oxide phantoms and the first Hydroxyapatite and Iron Dextran phantom). Both protocols are listed in Table 3.8. The phantoms were placed in the head holder with the vials parallel to the z-axis of the scanner.

Table 3.8: Phantom experiment SECT and DECT protocols.

Technique Parameter	SECT	DECT
<i>Scan Type</i>	Helical	Helical (GSI-9)
<i>kVp</i>	120	80/140
<i>mA</i>	220	600
<i>Rotation Time (s)</i>	0.8s	0.9
<i>Pitch</i>	0.531	0.531
<i>CTDI_{vol} (mGy)</i>	65.2	132.6
<i>Image Thickness (mm)</i>	0.625	0.625
<i>Interval (mm)</i>	0.625	0.625
<i>Beam Width (mm)</i>	20	20
<i>Scan FOV</i>	Head	Head
<i>Display FOV (mm)</i>	250	250

3.2.5 Image Analysis

In phantoms P1-2 and R1-4, circular regions of interest (ROIs) approximately 7.5 mm in diameter were placed within each vial on five consecutive images for the SECT, DECT (when acquired) calcium(water) and water(calcium), and each echo of the MFGRE. The mean of the voxels within each ROI was calculated; the standard deviation of the mean values (n = 5) was used to measure the dispersion across the five images. For phantom RF1, the calibration phantom, the mean and standard deviation of the signal over three acquisitions of the MFGRE were calculated. The T2* GRE was assessed qualitatively for signal suggestive of susceptibility lesions, where the signal decreases with increasing TE.

For a multi-echo T2*-weighted GRE pulse sequence, the signal in a uniform material is expected to decay exponentially according to the following equation,

$$S(t) = S(t = 0) * e^{-TE/T2^*} \quad \text{Equation 3.1}$$

where $S(t)$ represents the signal at time t . The mean MFGRE signal in each vial was fit to this equation using a non-linear least square fit in Matlab (R2016a; MathWorks, Natick, MA) to calculate the $T2^*$.

In phantom RF1, we tested reproducibility of the $T2^*$ calculations by performing the same analysis found above across three acquisitions of the MFGRE. We calculated the mean $T2^*$ and the standard deviation of the mean over the three acquisitions. In phantom RF2, voxel-wise $T2^*$ calculations were made within the lesion models for one circular ROI (6.6 mm diameter, 34.2 mm² area) placed by hand within the lesion models. When a given lesion contained a mass visible on the MRI, the ROI was placed at the z-location of the mass and included both the mass and a portion of the background material to mimic the placement of an ROI on a biological lesion with a mixed signal. The mean signal from each lesion was fit with both a monoexponential curve (Equation 3.1) and a biexponential curve (Equation 3.2) to characterize multiple materials within a single lesion model.

$$S(t) = a * e^{-\frac{TE}{T2^*_1}} + b * e^{-\frac{TE}{T2^*_2}} \quad \text{Equation 3.2}$$

The mean and standard deviation were calculated for each ROI on the $T2^*$ image. For lesions with masses that visibly contained regions of differing $T2^*$ values, a histogram was generated, and a kernel density estimator was applied in Matlab. The mean of each region was determined by finding the locations of the peaks in the kernel density estimate. The peak locations along the $T2^*$ axis of the histogram were compared to the values $T2^*_1$ and $T2^*_2$ from the biexponential fit of the mean signal in the ROI.

3.3 Results

3.3.1 Hydroxyapatite and Iron Oxide Preliminary Phantoms

DECT water(calcium) and calcium(water) images were analyzed in both the low and high concentration phantoms. As the concentration of each material increased, the mean measured

calcium density increased for both materials (Figure 3.9), while the mean water value decreased for iron-based lesion models and increased for calcific lesion models. This result is in agreement with Nute et al. (135).

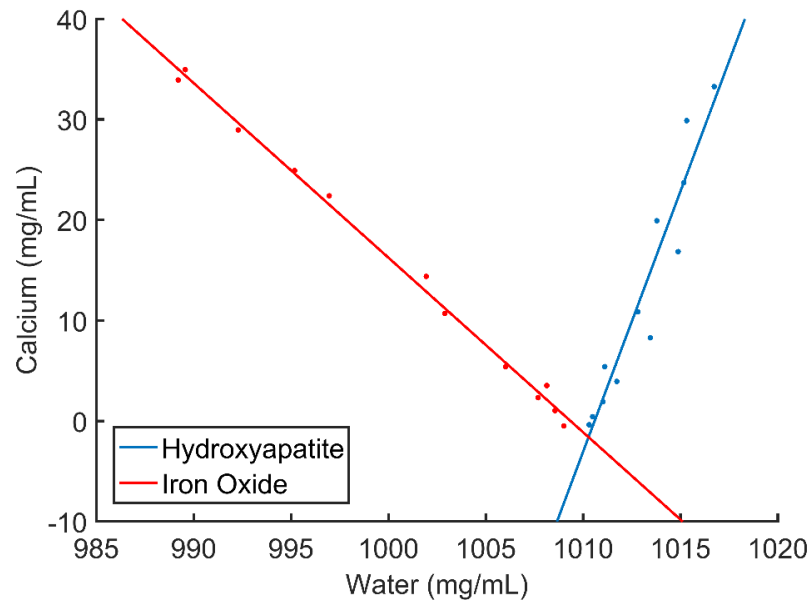


Figure 3.9: DECT water/calcium decomposition measurements for iron oxide and hydroxyapatite samples with matched SECT HU. Calcium density increases as SECT HU increases for both materials. Note that the use of the calcium/water material decomposition does not indicate that calcium was present within the iron oxide samples (see Section 2.3.4).

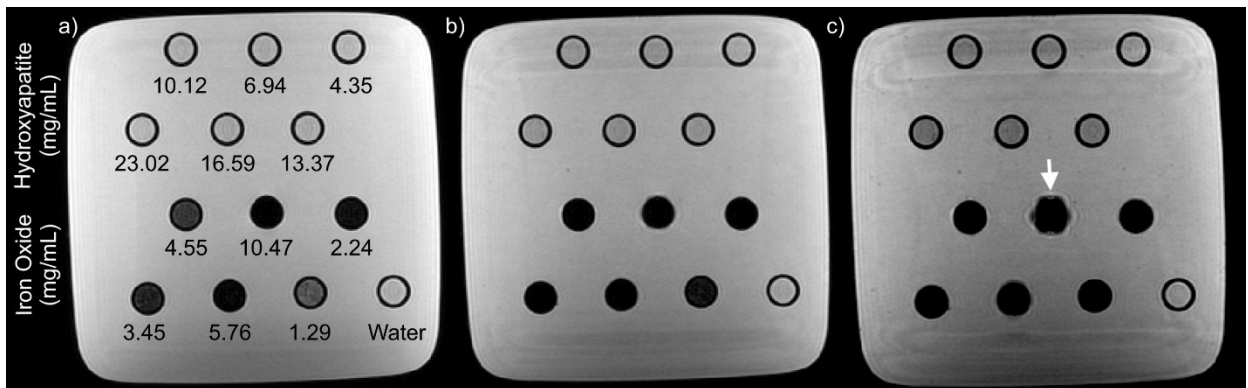


Figure 3.10: MFGRE magnitude images of the low concentration iron oxide (two bottom rows) and hydroxyapatite (two top rows) phantom for echo times of a) 4.5 ms, b) 14.5 ms, and c) 24.6 ms. At the highest echo time, the 10.47 mg/mL iron oxide sample (white arrow) becomes distorted. Note that very little signal is present in the iron oxide samples, even at low TE. Numeric labels represent the concentration of hydroxyapatite or iron oxide in units of mg/mL.

Low Concentration Phantom (P1)

The iron oxide demonstrated very low signals on the MFGRE pulse sequence, even at low concentrations. The effect is demonstrated in Figure 3.10, where the six iron oxide mixtures are shown in the bottom two rows of the phantom for echoes 1, 3 and 5 (TEs of 4.5, 14.5, and 24.6 ms). In Figure 3.10c, the shape of the vial containing the highest iron oxide concentration (10.47 mg/mL) is warped into that of a magnetic dipole (white arrow). At the same TEs, the hydroxyapatite vials show a slight decrease in the signal as echo time increases. In echoes 1 and 3, there is almost no difference in the signal that can be visually appreciated between hydroxyapatite gels of different concentrations; by the fifth echo (Figure 3.10c), there begins to be visually lower signal in those vials with higher concentrations of hydroxyapatite.

The quantitative analysis of the MFGRE signal showed that by a TE of approximately 30 ms, virtually all signal had dephased in the iron oxide samples. Three vials (4.55, 5.76, and 10.47 mg/mL) had signal levels below 1000 AU at TE = 4.5 ms (Figure 3.11). The signal in each sample was normalized to the first echo to improve visualization of the concentration dependence, which can be noted for the three lowest concentration samples. T2* values were calculated for each vial (Table 3.9), but due to the extremely low signal values in three of the samples, the R² of the exponential fit used to calculate the T2* was less than 0.2 and the values are therefore considered to be inaccurate. In general, we would expect the T2* to decrease with increasing iron presence in lesions with signal present above the noise floor.

The hydroxyapatite samples did not decay to the noise floor and had a much higher initial signal than the iron oxide (Figure 3.12). For both materials, signal decayed steadily with increasing TE, and normalizing the signal demonstrates a concentration dependence in the decay rate. The T2* generally decreases with increasing analyte concentration (Table 3.9). The vials containing the three lowest concentrations of hydroxyapatite were positioned near the

edge of the phantom and were subject to increased signal decay due to proximity to the air-phantom border, which may have impacted the T2* calculations.

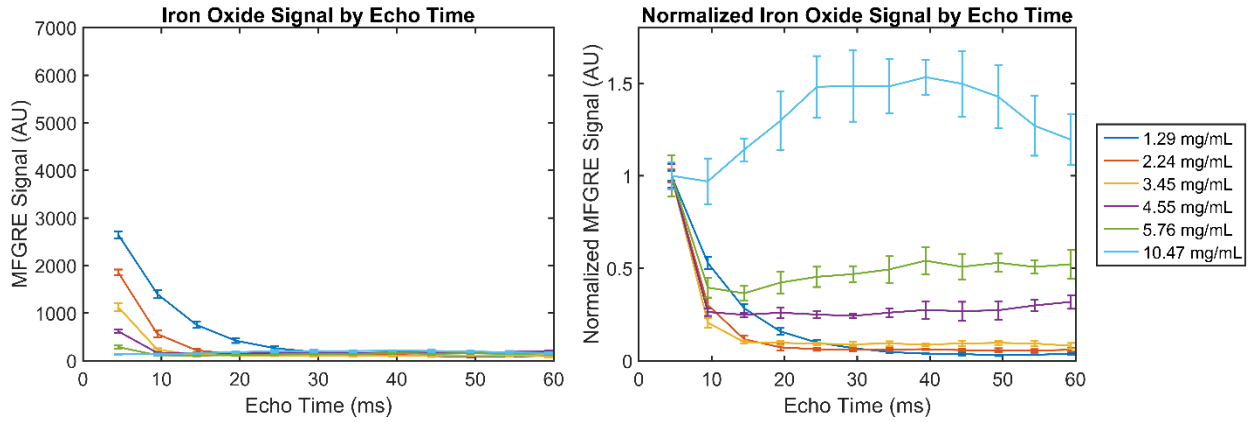


Figure 3.11: Iron oxide MFGRE signal at low concentrations. The signal in all samples dephased within a TE of 30 ms. Lower concentrations featured higher signal levels at lower TEs. The signal normalized to the first echo for each vial shows very little change in signal across the later echoes. The high normalized signal in the 10.47 mg/mL is solely indicative of the very low signal values across all echoes.

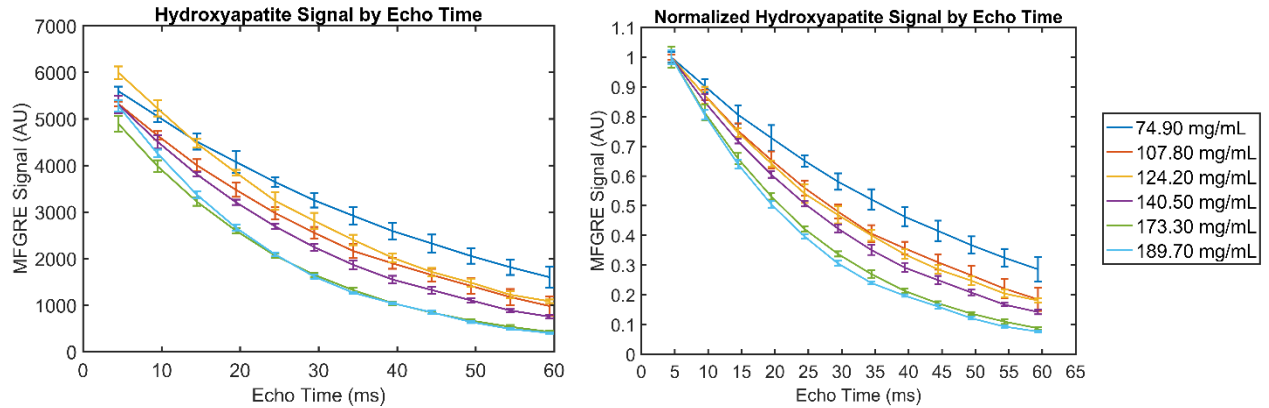


Figure 3.12: Hydroxyapatite MFGRE signals for low concentrations. The signal decreased steadily with increasing echo time (TE), and higher concentrations generally had lower signal levels. The normalized signal shows that higher concentrations decay at a slightly faster rate with increasing TE than lower concentrations.

Table 3.9: T2* values for hydroxyapatite and iron oxide samples of varying concentrations. The mean signal over five images was used to calculate T2*.

Hydroxyapatite Concentration (mg/mL)	Calculated T2* (ms)	Iron Oxide Concentration (mg/mL)	Calculated T2* (ms)
4.35	71.38	1.29	8.29
6.94	63.50	2.24	4.54
10.12	57.60	3.45	3.60
13.37	71.39	4.55	**
16.59	63.15	5.76	**
23.02	48.90	10.47	**

**Curves were poorly fit by the monoexponential decay model, due to signal levels at the noise floor for all TEs.

High Concentration Phantom (P1)

A qualitative analysis of the MFGRE images for the high concentration phantom shows little to no signal in the iron-containing lesion models. However, there is a concentration dependence to the apparent size of the sample at a given TE. This effect is exaggerated as the TE is increased (Figure 3.13). The hydroxyapatite samples have similar signals regardless of concentration at low TE (Figure 3.13a), and the concentration dependence of the signal level becomes more obvious as TE increases (Figure 3.13c). There is no blooming artifact present in the vials containing hydroxyapatite.

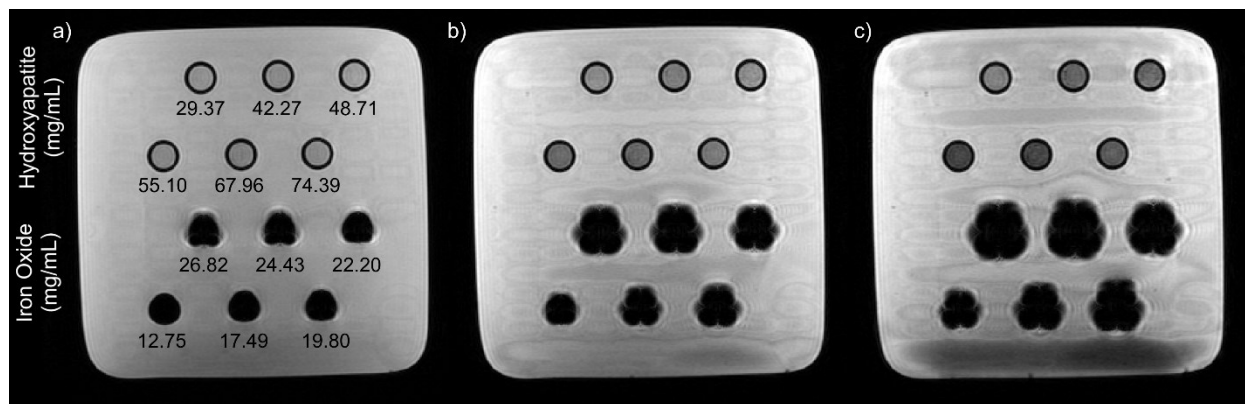


Figure 3.13: MFGRE magnitude images of the high concentration iron oxide (two upper rows) and hydroxyapatite (two lower rows) phantom with a) TE = 4.5 ms, b) TE = 14.5 ms, and c) TE = 24.6 ms. Numeric labels refer to the concentration of hydroxyapatite and iron oxide in each sample in units of mg/mL. Note the blooming in the iron oxide samples increases with TE and with increasing iron concentration.

Quantitative analysis of the MFGRE signal with TE shows that the hydroxyapatite samples in this phantom have a faster decay rate (lower $T2^*$) than in the previous, lower concentration phantom, which is depicted graphically in the normalized signal plot of Figure 3.14. The concentration dependence of the signal decay is shown definitively in this phantom. The $T2^*$ parameter calculated in these hydroxyapatite samples ranged from 21.32 ms at a concentration of 189.70 mg/mL to 44.76 ms at 74.90 mg/mL (Table 3.10).

The iron oxide signal levels within this phantom were all negligible, and no change was noted with TE (Figure 3.15). These signal levels were too low to provide an accurate assessment of the $T2^*$ for the samples.

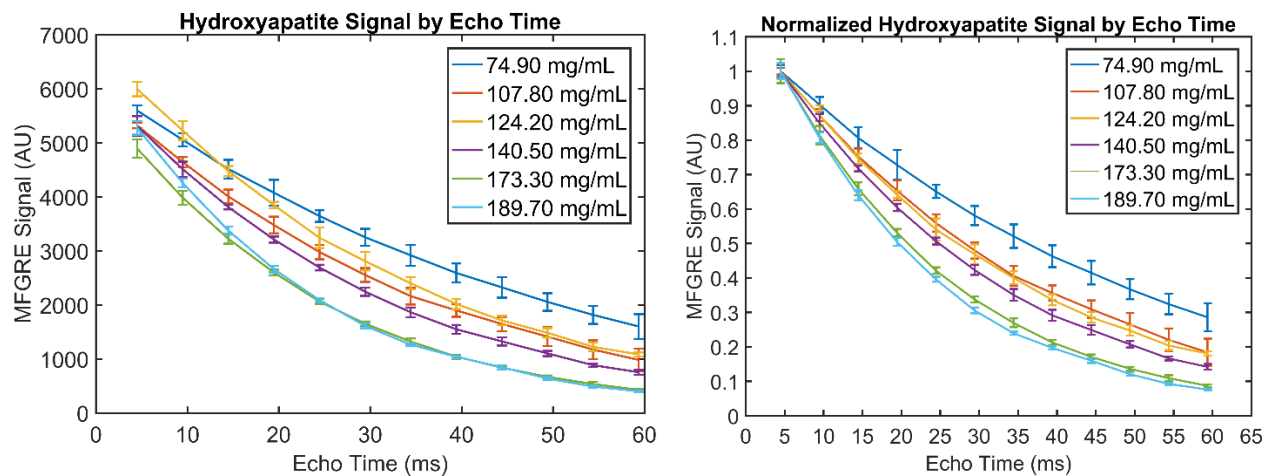


Figure 3.14: Hydroxyapatite signal in the high concentration preliminary phantom by echo time (TE). The normalized signal shows a clear concentration dependence in the decay rate of the signal with TE.

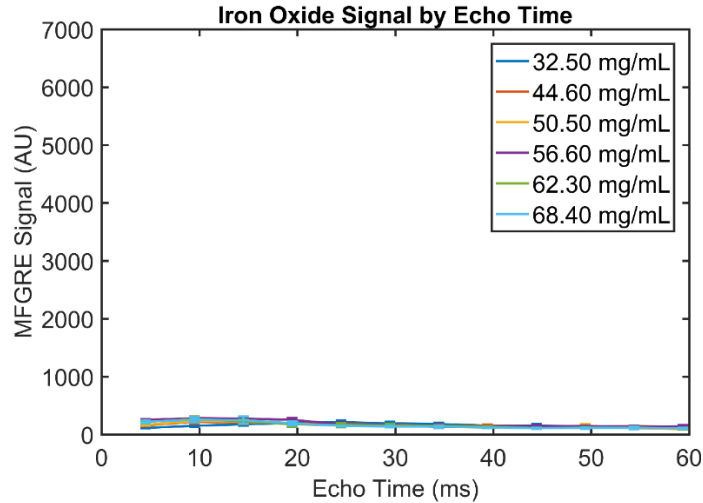


Figure 3.15: Iron oxide signal in the high concentration phantom shows a low signal at all echo times for all concentrations of iron oxide present.

Table 3.10: T2* values for hydroxyapatite samples of varying concentrations. The mean signal over five images was used to calculate T2*.

Hydroxyapatite Concentration (mg/mL)	Calculated T2* (ms)
74.9	44.76
107.8	33.42
124.2	32.00
140.5	28.50
173.3	22.78
189.7	21.32

3.3.2 Hydroxyapatite and Iron Dextran Phantoms

Approximately Matched SECT HU Phantom (R1)

The round phantom design minimized the signal loss caused by the air-phantom boundary by increasing the space between the samples and the outer edge of the phantom. The iron dextran tested in this phantom showed T1 shortening, indicated by the bright initial signal on the first echo of the MFGRE, and chemical shift artifact (black band above sample) at very high concentrations of iron dextran (Figure 3.16 a). Despite the high initial signal, the iron dextran displayed significant T2* decay, which was evident as the TE increased (Figure 3.16 b and c).

The hydroxyapatite samples were present in higher concentrations than in previous phantoms, and complete signal dropout was accomplished at later echoes (Figure 3.16 c).

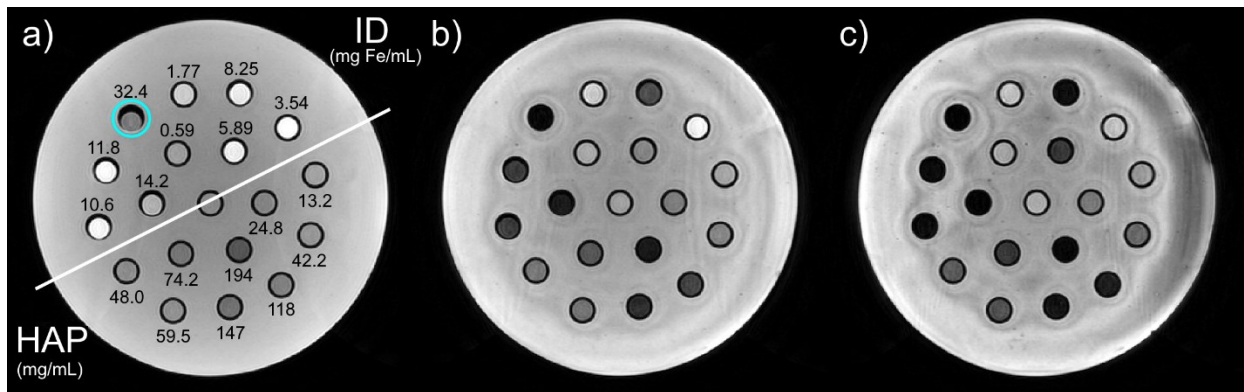


Figure 3.16: MFGRE magnitude images of an iron dextran (ID) and hydroxyapatite (HAP) phantom with the round design; sample concentrations are given in mg/mL for HAP and mg Fe/mL for ID. Iron dextran is on the top half and hydroxyapatite on the bottom half, as indicated by the white line in (a). The iron dextran displays T1 shortening (bright signal), and a chemical shift is present in high concentrations, indicated by the cyan circle (a). Signal remains present in several iron dextran samples at the third (b), and fifth (c) echoes and higher concentrations of hydroxyapatite were tested to decrease the T2* further relative to prior phantoms.

Quantitatively, the iron dextran signal at the lowest TE varies, in large part due to the T1 effects seen in the phantom images. The highest concentration (32.41 mg Fe/mL) had complete signal dropout by a TE of 19.5 ms (Figure 3.17), but enough signal was present in the prior echoes to measure T2*. The relaxation rate is a function of the iron dextran concentration, with a T2* of 86.92 ms at 0.59 mg Fe/mL down to 3.45 ms at 32.41 mg Fe/mL (Table 3.11). Notably, the hydroxyapatite samples had a similar range of T2* as the iron dextran (7.62 – 49.68 ms).

DECT analysis was performed in this phantom to the iron- and calcium-based lesions because the SECT HU values were intentionally matched between the iron dextran and hydroxyapatite. Plotting the mean water(calcium) and calcium(water) values show that the materials are not separable using this material decomposition Figure 3.19.

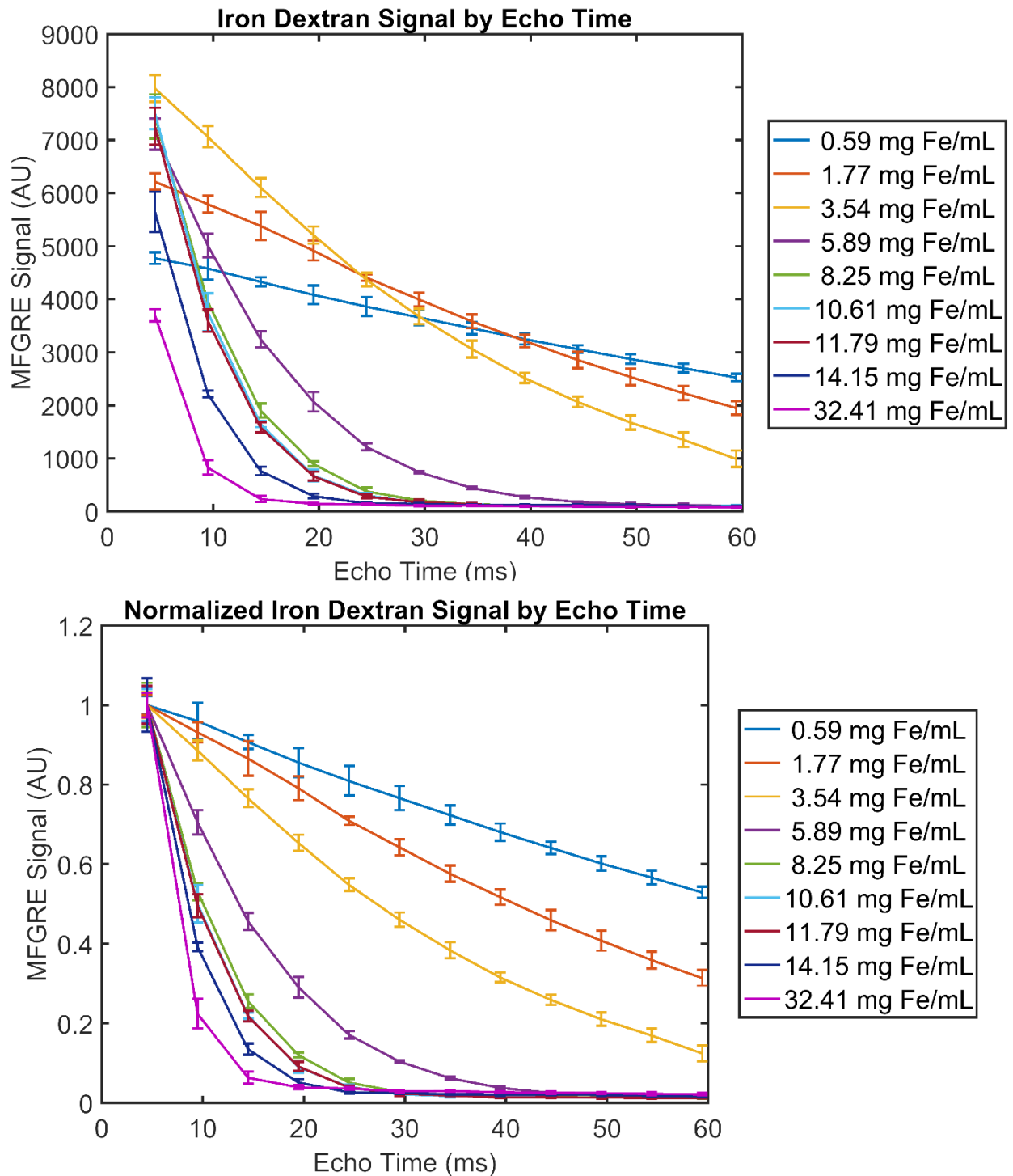


Figure 3.17: MFGRE signal changes with increasing echo time (TE) for iron dextran samples in a round phantom. Signal normalized to the first TE is displayed in the plot at the bottom to emphasize the concentration dependence of the signal decay.

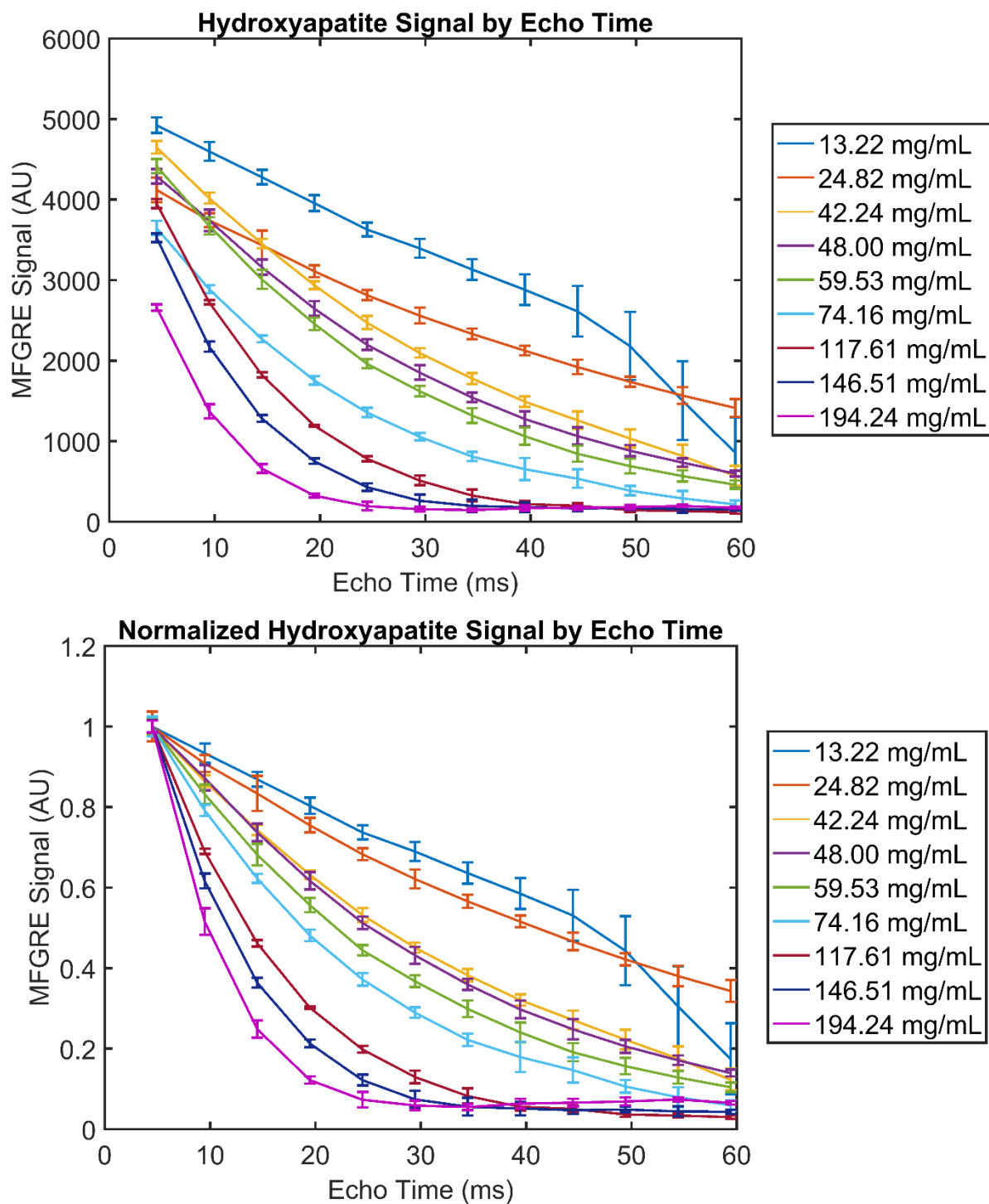


Figure 3.18: MFGRE signal changes with increasing echo time (TE) for hydroxyapatite samples in a round phantom. Signal normalized to the first TE is displayed in the plot at the bottom to emphasize the concentration dependence of the signal decay.

Table 3.11: Calculated T2* for iron dextran and hydroxyapatite in a phantom with approximately matched SECT HU ranges.

Iron Dextran Concentration (mg Fe/mL)	SECT Attenuation (HU)	Calculated T2* (ms)	Hydroxyapatite Concentration (mg/mL)	SECT Attenuation (HU)	Calculated T2* (ms)
0.59	8.72	86.92	13.22	22.85	49.68
1.77	11.77	49.60	24.82	39.19	51.96
3.54	19.33	29.58	42.24	66.65	29.91
5.89	44.30	11.80	48.00	75.96	28.64
8.25	67.49	7.36	59.53	87.05	24.50
10.61	75.90	6.71	74.16	112.56	20.18
11.79	78.23	6.68	117.61	178.84	12.58
14.15	94.72	5.22	146.51	231.32	10.01
32.41	218.53	3.45	194.24	326.78	7.62

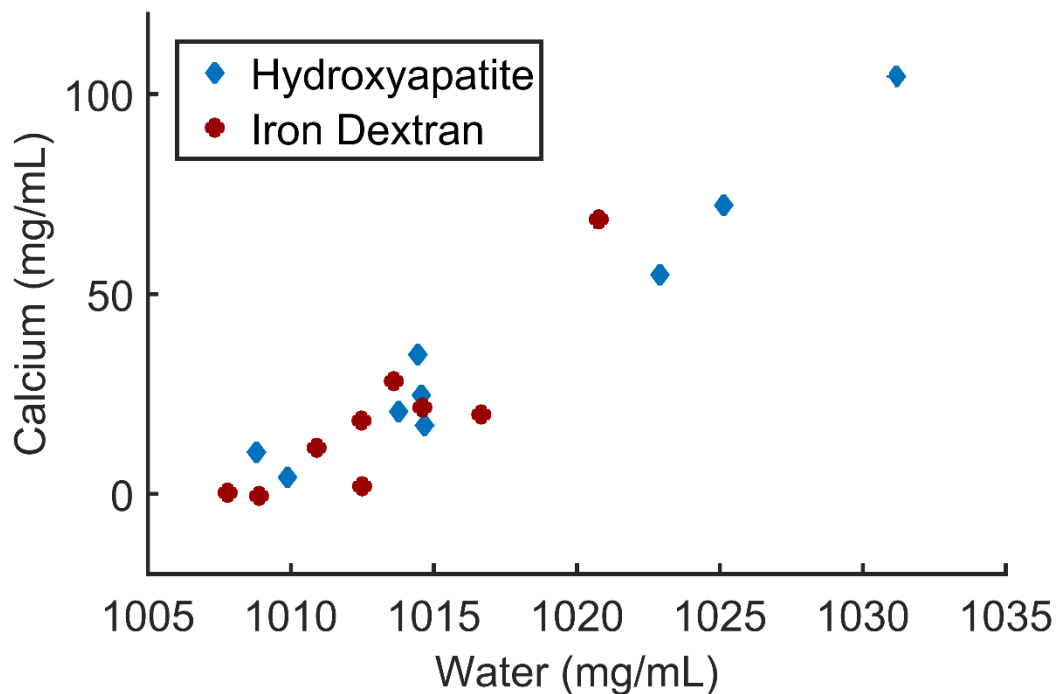


Figure 3.19: DECT calcium/water material decomposition data for iron dextran and hydroxyapatite samples. Note that sulfur is present in the iron dextran complex, which is not present amongst biological hemorrhage.

Biological T2* Phantom (R2)

This phantom demonstrated that iron dextran concentrations could be adjusted to create lesion models with biological levels of T2*. Lowering the concentration also had the added benefit of eliminating the chemical shift artifact that was seen in the vial with the most dextran complex in

the previous phantom (Figure 3.16). The ranges of the calculated T2* for the iron dextran and hydroxyapatite lesions, respectively, were found to be 30.44 – 89.49 ms and 5.53 – 42.22 ms (Table 2.2, Figure 3.20, Figure 3.21). The T2* values for hemorrhagic lesion models are in agreement with the literature values for iron-laden gray matter (4.1 – 62.5 ms) (209) and cavernomas (211), while the hydroxyapatite samples covered nearly the full range of T2* (9 – 50 ms) found in calcifications by Roy et al. (212).

Table 3.12: Calculated T2* from the monoexponential fits for various concentrations of iron dextran and hydroxyapatite in a phantom with biological susceptibility levels.

Iron Dextran Concentration (mg iron/mL)	Calculated T2* (ms)	Hydroxyapatite Concentration (mg/mL)	Calculated T2* (ms)
0.4	89.49	7.8	42.22
0.8	80.85	15.7	23.81
1.2	63.82	23.5	17.52
1.6	49.26	31.4	13.01
2	45.48	39.2	10.00
2.4	42.03	58.8	8.94
2.8	37.96	78.4	7.56
3.2	33.60	137.3	6.83
3.6	30.44	196.1	5.53

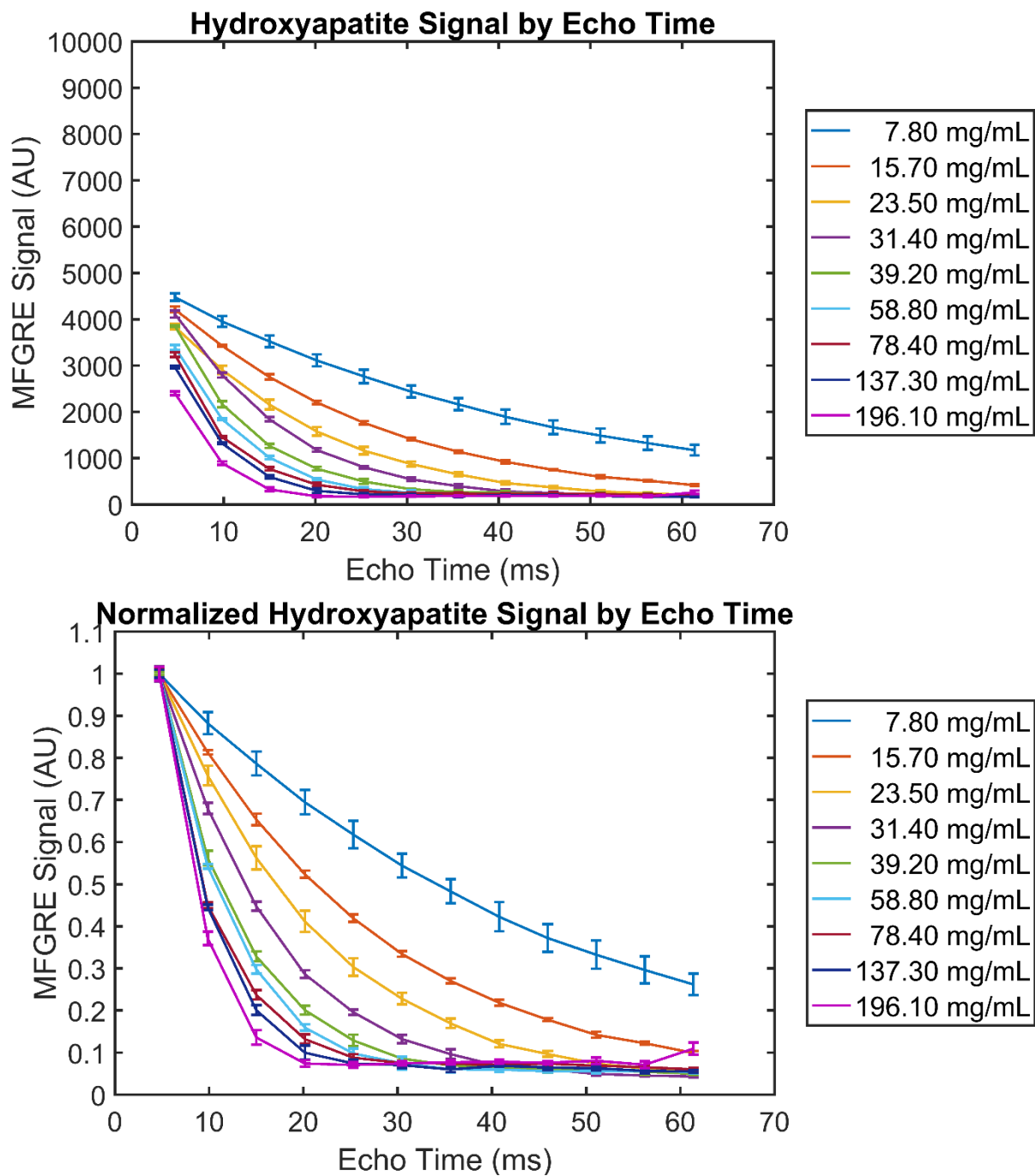


Figure 3.20: MFGRE signal and normalized signal for hydroxyapatite with biological T_2^* levels. The T_2^* ranges from 5.53 to 42.22 ms in this phantom.

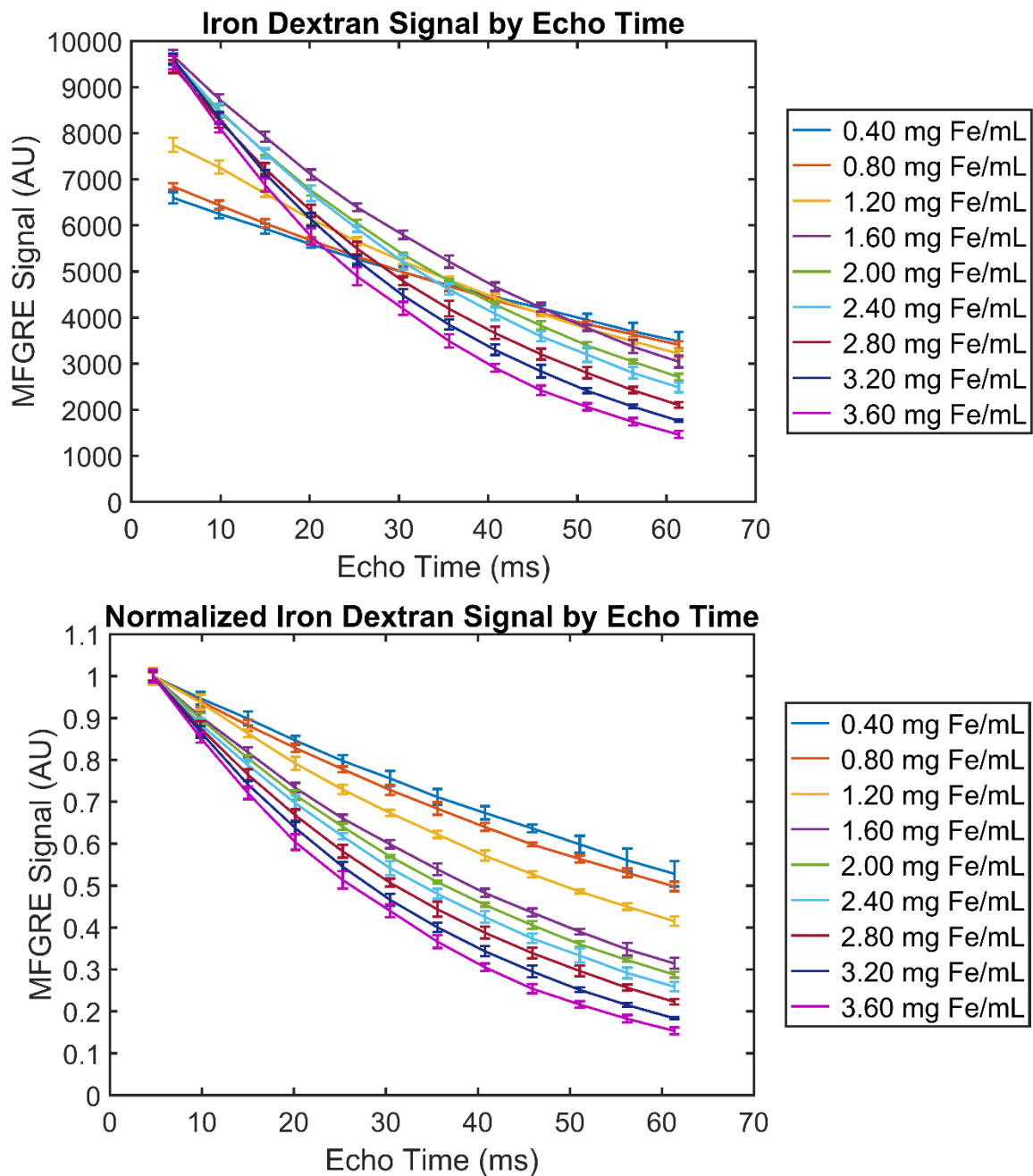


Figure 3.21: MFGRE signal and normalized signal for iron dextran with T2* values within the range expected in normal gray and white matter. The T2* in this phantom ranges from 30.44 to 89.49 ms.

3.3.3 Calcium Chloride Phantom (R3)

The MFGRE signal decay curves for the serial dilutions of calcium chloride in this phantom experiment are shown in the figure below (Figure 3.23). Low $T2^*$ is indicative of faster signal dephasing due to magnetic field inhomogeneities. Overall, hydroxyapatite had a lower $T2^*$ to SECT attenuation ratio (Figure 3.22), making it more similar to calcification than the calcium chloride.

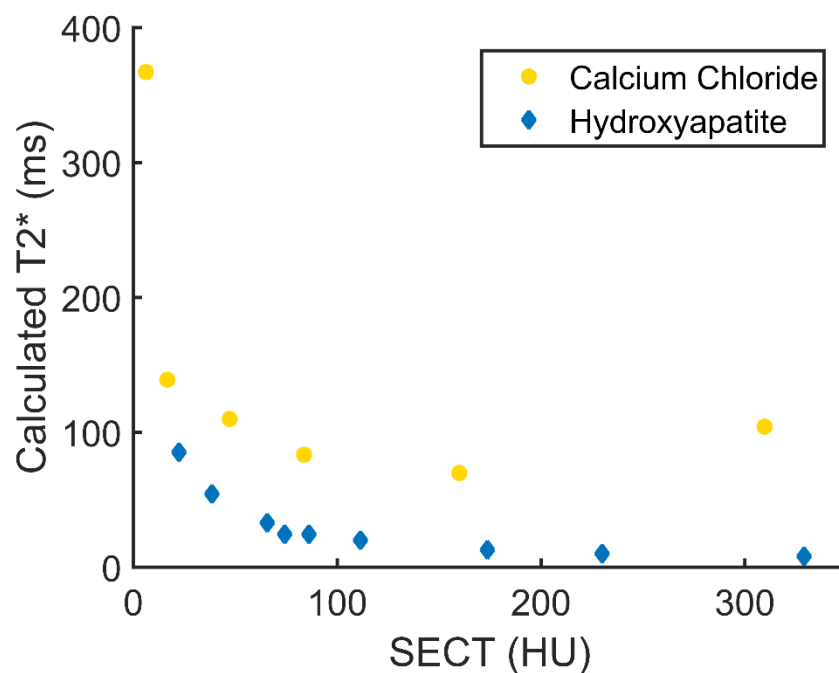


Figure 3.22: Calculated $T2^*$ versus the SECT attenuation of the hydroxyapatite and calcium chloride gels. The $T2^*$ of the calcium chloride is higher than that of the hydroxyapatite for all SECT levels investigated.

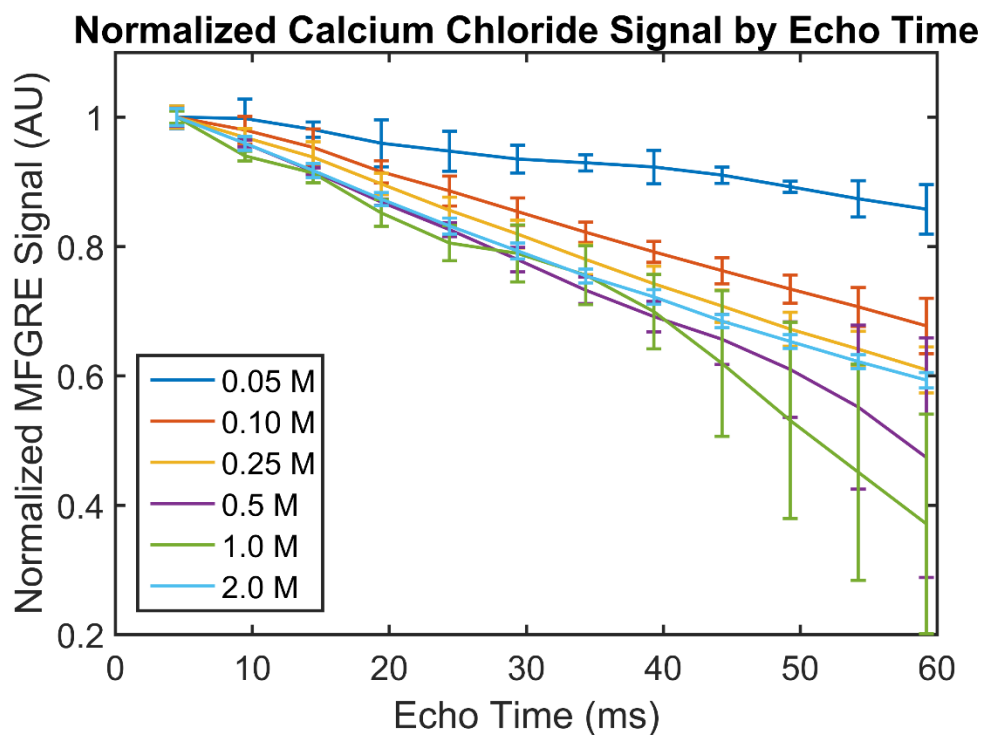
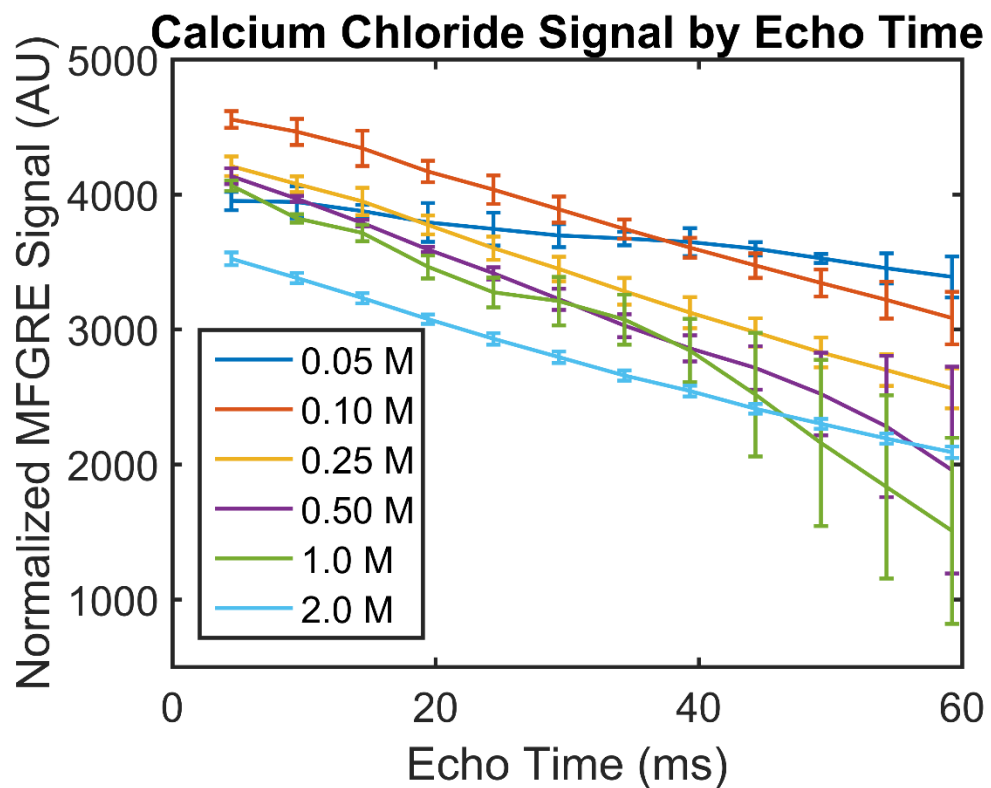


Figure 3.23: MFGRE magnitude signal for various concentrations of calcium chloride with and without signal normalization

3.3.4 Iron Oxidation State Phantom (R4)

The 0.4 mg Fe/mL concentration of iron(II) chloride was excluded from analysis due to the presence of an air bubble. Qualitatively, the signal of the iron(II) chloride was generally higher than that of the iron(III) chloride for the same amount of iron present. The signal of each material was concentration dependent, but the decrease in the normalized signal was greater for iron(III) than iron(II) (Figure 3.24, Figure 3.25).

The iron oxidation state of iron was shown to change the calculated T2* relaxation time for equal concentrations of iron particles. The ranges of calculated T2* for iron(II) chloride and iron(III) chloride were 84.96 – 777.14 ms and 4.01 – 90.53 ms, respectively. Both compounds demonstrated monotonically decreasing T2* with increasing iron concentration.

Table 3.13: Calculated T2* for various concentrations of iron(II) chloride and iron(III) chloride in a phantom. The 0.4 mg Fe/mL iron(II) chloride sample was excluded due to the presence of an air bubble.

Iron (II) Chloride Concentration (mg Fe/mL)	Calculated T2* (ms)	Iron(III) Chloride Concentration (mg Fe/mL)	Calculated T2* (ms)
0.2	777.14	0.2	90.53
0.4	-	0.4	30.11
0.6	190.31	0.6	15.63
0.8	133.91	0.8	10.57
1.0	117.55	1.0	7.31
1.2	105.89	1.2	5.67
1.4	101.34	1.4	4.87
1.6	84.96	1.6	4.01

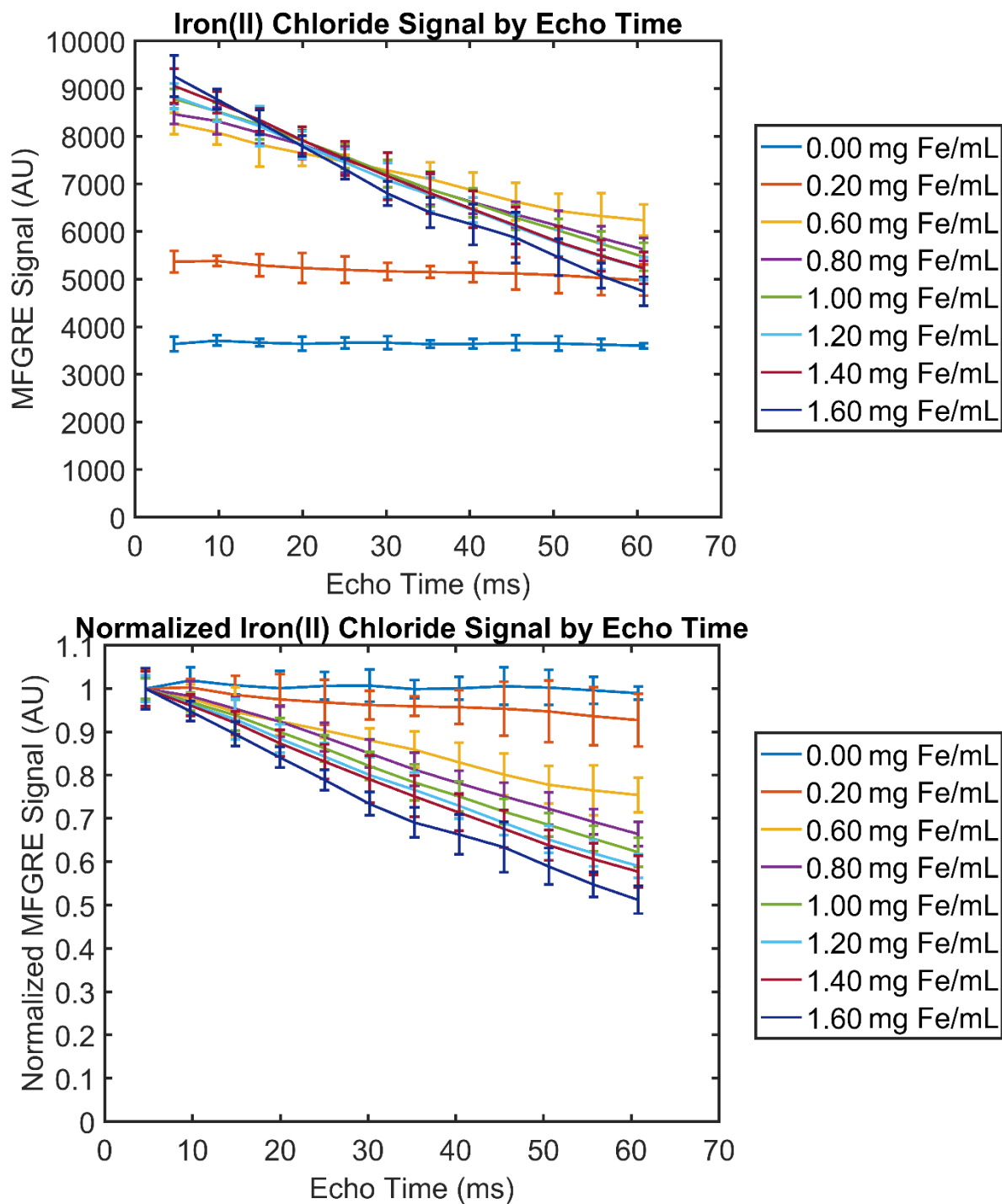


Figure 3.24: Iron(II) Chloride MFGRE signal data. Units of concentration are given in mg Fe/mL. Note that while there is a concentration dependence in the normalized plot, there is relatively little signal dropout even at high concentrations.

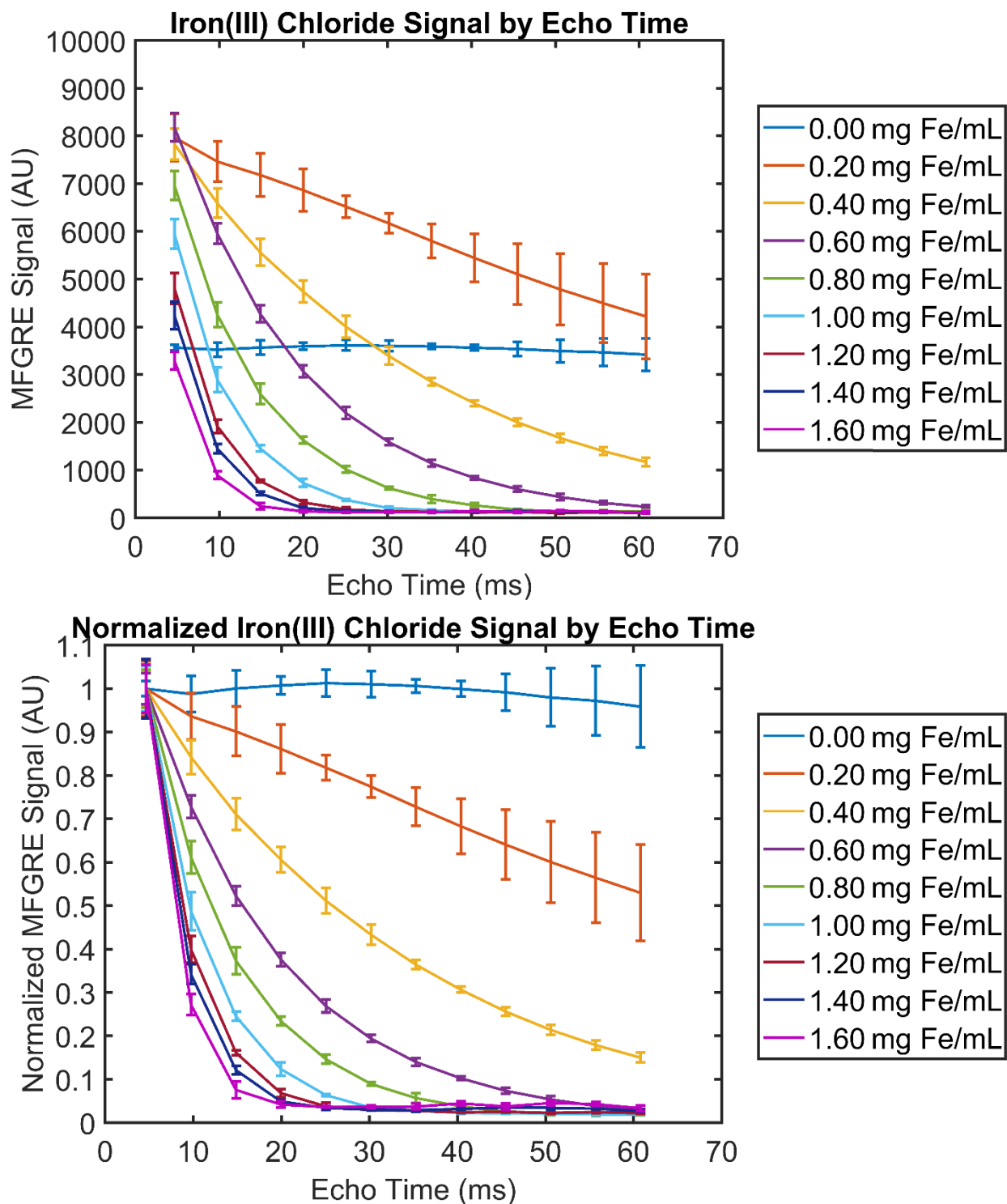


Figure 3.25: Iron(III) chloride MFGRE signal curves. Units of concentration are given in mg Fe/mL. There is a large signal dropout at high iron concentrations that are not seen when the iron is in the 2+ oxidation state.

3.3.5 Final Biological Phantoms

Calibration Phantom (RF1)

Multiple materials were made to span the clinical range of expected T2* values in patients. Of the iron containing lesion models, hemoglobin had the highest T2*, followed by iron dextran and iron(III) chloride (Table 3.14). This range is highly desirable in a single phantom because there may be multiple categories of hemorrhage (acute, subacute, chronic, etc.) imaged within a clinical trial. The standard deviation of the T2* calculated from three different MFGRE acquisitions was very low (0.02 – 0.45 ms), indicating good repeatability. The normalized signal curves for each material are found in Figure 3.26 a-d.

Table 3.14: Mean \pm standard deviation of the T2* calculated for three acquisitions of the MFGRE.

Hydroxy-apatite	Conc. (mg/mL)	181.8	210.3	238.7	267.4
	T2* (ms)	8.74 \pm 0.03	7.66 \pm 0.08	7.07 \pm 0.10	6.40 \pm 0.22
Iron Dextran	Conc. (mg Fe/mL)	0.7	1.4	2.1	2.8
	T2* (ms)	57.85 \pm 0.15	44.28 \pm 0.06	35.96 \pm 0.06	30.87 \pm 0.02
Iron(III) Chloride	Conc. (mg Fe/mL)	0.31	0.62	0.94	1.25
	T2* (ms)	12.04 \pm 0.02	5.09 \pm 0.04	3.39 \pm 0.04	3.11 \pm 0.12
Hemoglobin	Conc. (mg Fe/mL)	0.17	0.34	0.42	0.66
	T2* (ms)	128.98 \pm 0.45	75.85 \pm 0.24	74.21 \pm 0.17	16.13 \pm 0.04

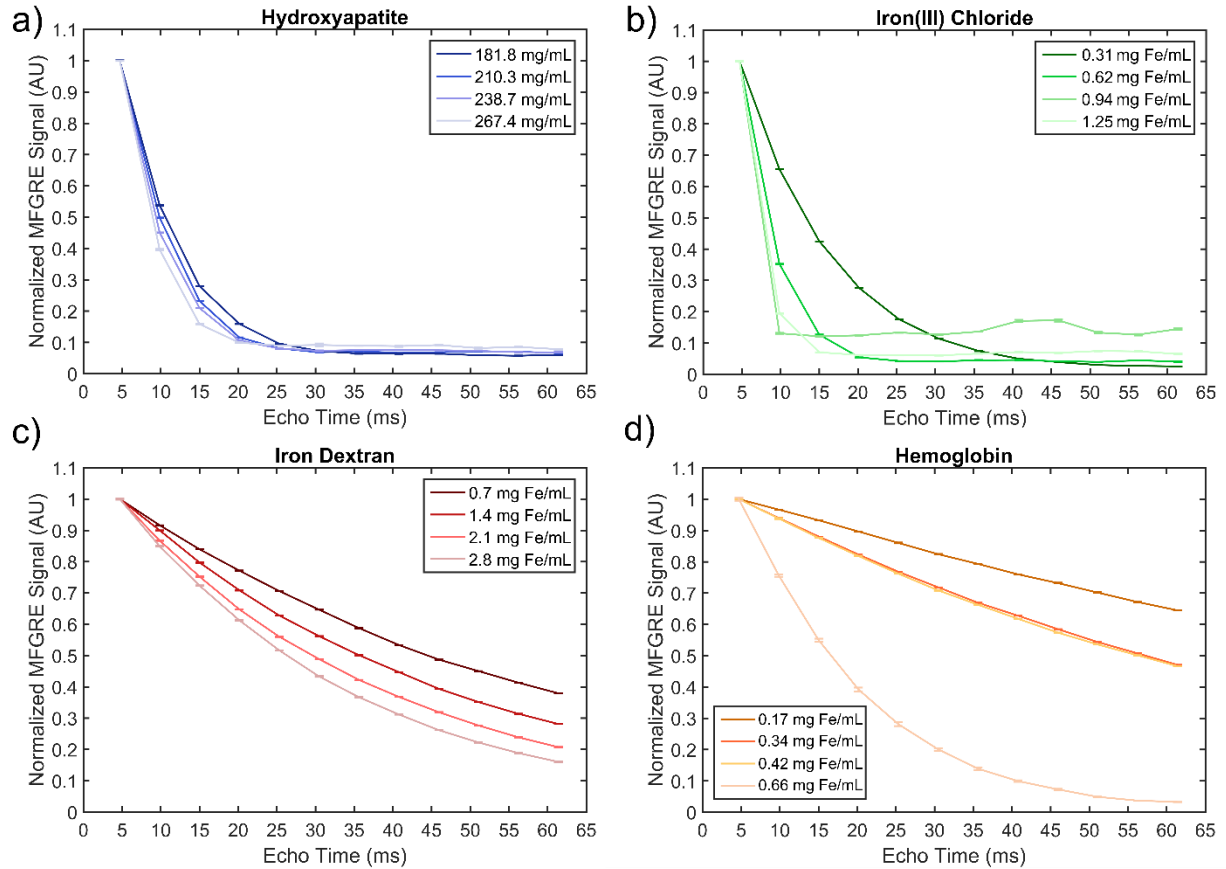


Figure 3.26: Normalized MFGRE signal curves for a) hydroxyapatite, b) iron(III) chloride, c) iron dextran, and d) human hemoglobin.

Biological Phantom with Mixed Materials (RF2)

Voxel-wise T_2^* fitting of ROIs within each sample returned T_2^* values between 3.92 ms and 80.86 ms. The mean and standard deviation of the T_2^* for each mixture is located in Table 3.15. Displaying the ROIs in a single plane (Figure 3.27) demonstrates the presence of the hydroxyapatite lesions (upper left) within four samples of iron dextran. The mixtures did not display large non-uniformities, and the standard deviations in the T_2^* measurements were small.

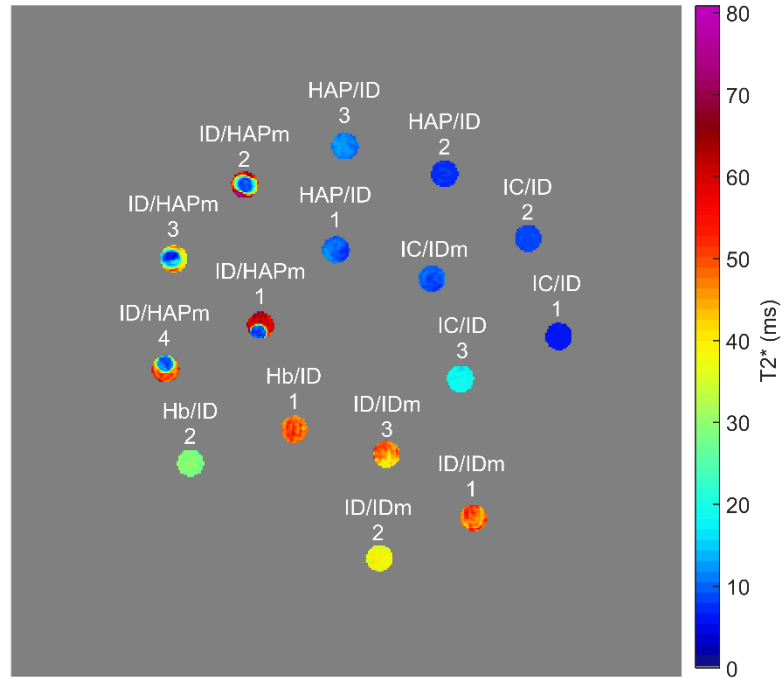


Figure 3.27: Voxel-wise T_2^* calculations for each sample displayed in the same plane along the z-axis. The four vials labeled ID/HAPm have an iron dextran background and hydroxyapatite masses, and additional analysis was performed for these samples.

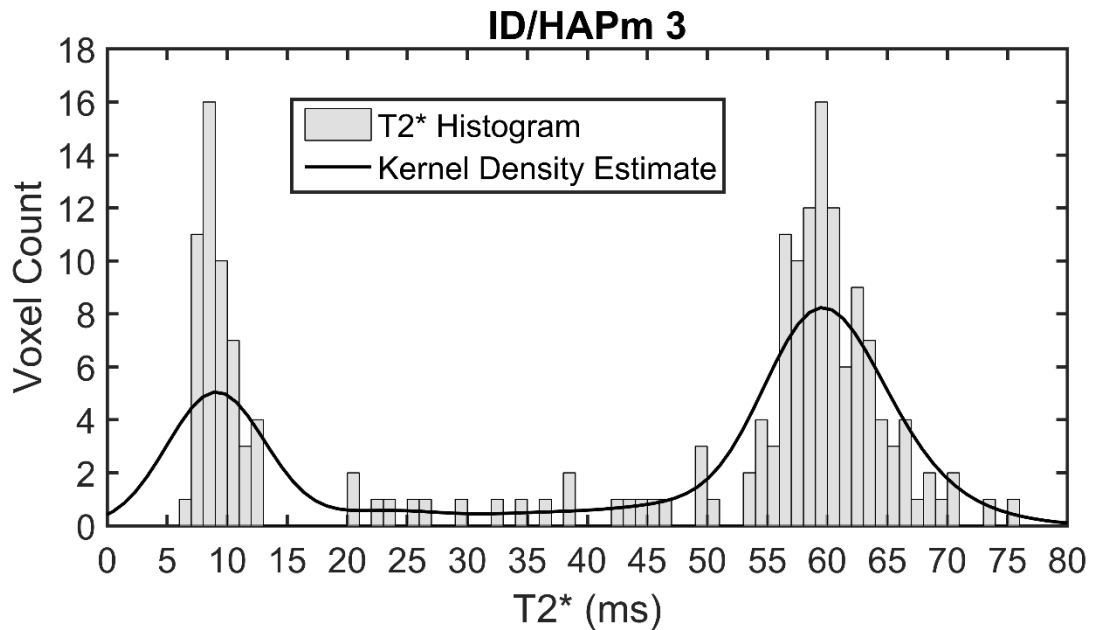


Figure 3.28: An example of the histogram analysis for the iron dextran samples that contained hydroxyapatite masses. A kernel density estimate (black line) was fit to the data to estimate the mean T_2^* of the background and mass. This suggests that voxel-wise

histogram analysis of $T2^*$ might contain characterizing information that could be used clinically.

Table 3.15: Mean and standard deviation of each mixture or sample without visible mass for the voxel-wise calculation of $T2^*$.

Lesion Model	Mean $T2^*$ (ms)	Standard Deviation (ms)
<i>HAP/ID 1</i>	10.00	1.41
<i>HAP/ID 2</i>	7.58	0.44
<i>HAP/ID 3</i>	11.69	0.84
<i>IC/ID 1</i>	6.14	0.28
<i>IC/ID 2</i>	8.58	0.38
<i>IC/ID 3</i>	18.51	0.72
<i>Hb/ID 1</i>	48.54	2.38
<i>Hb/ID 2</i>	29.01	1.10
<i>IC/IDm</i>	9.46	1.06
<i>ID/IDm 1</i>	48.04	3.11
<i>ID/IDm 2</i>	48.54	2.38
<i>ID/IDm 3</i>	45.22	4.01

Table 3.16: $T2^*$ estimates for lesions containing masses, resulting from the biexponential fit of the ROI means and the peak location of the $T2^*$ kernel density estimate for the voxel-wise calculations.

Lesion Model	Biexponential Fit		Kernel Density Estimate		Biexponential Fit Error	
	<i>$T2^*_1$</i> (ms)	<i>$T2^*_2$</i> (ms)	<i>Peak 1</i> (ms)	<i>Peak 2</i> (ms)	<i>$T2^*_1$ Err.</i> (ms [%])	<i>$T2^*_2$ Err.</i> (ms [%])
<i>ID/HAPm 1</i>	3.58	34.17	8.38	39.33	-4.80 [-57%]	-5.16 [-13%]
<i>ID/HAPm 2</i>	7.87	47.26	10.75	48.45	-2.88 [-27%]	-1.19 [-2.5%]
<i>ID/HAPm 3</i>	7.09	62.21	8.91	59.46	-1.82 [-20%]	2.75 [4.6%]
<i>ID/HAPm 4</i>	10.74	89.72	9.34	52.86	1.40 [15%]	36.86 [70%]

For the four lesion models with masses that were apparent on the $T2^*$ map (ID/HAPm 1-4, Figure 3.27), the results of the biexponential fitting and kernel density estimate (example in Figure 3.28) are displayed in Table 3.16. The estimates from the biexponential fit were within

approximately 5 ms of the T2* calculated from the peaks of the histogram's kernel density estimate. Overall, a linear fit of the estimated T2* values from the biexponential fit versus the peak locations of the voxelized T2* calculations had an R² value of 0.849, indicating that the two analysis methods were correlated (Figure 3.29). The biexponential fit of the higher T2* peak from the iron background did not fit well, and there was a 70% overestimate of the T2*. However, the mass was angled so that there was very little background in the ROI, and the higher peak was not evident in the histogram.

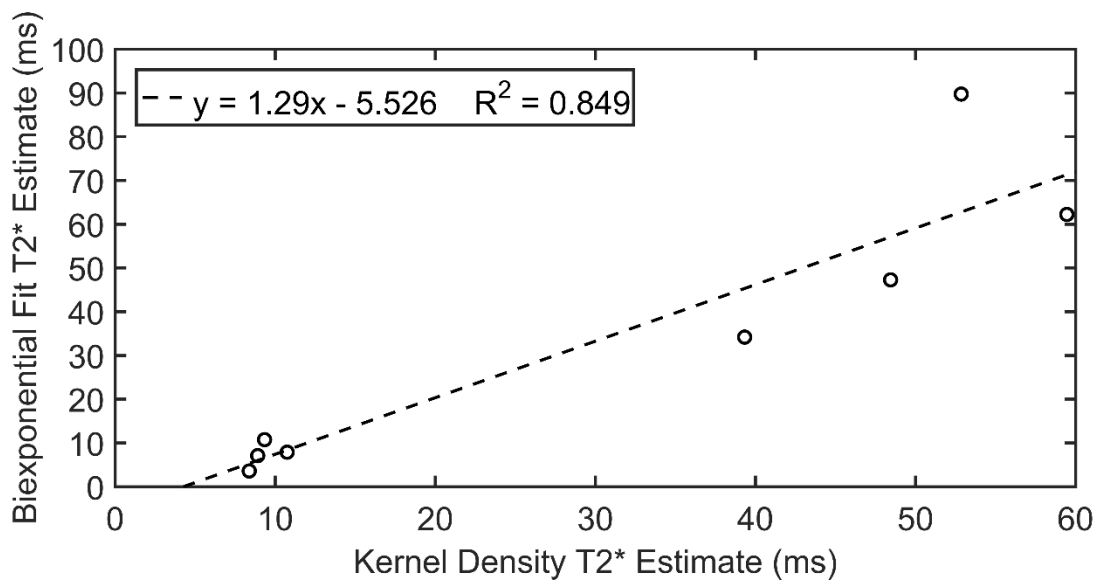


Figure 3.29: A linear fit of the T2* estimates resulting from the voxelized (kernel density) and ROI-based (biexponential fit) T2* estimates for iron dextran lesions with hydroxyapatite masses demonstrates correlation between the two analysis methods.

3.4 Discussion

The goal of this study was to validate materials for an MRI phantom of calcific and hemorrhagic lesion models and construct a final phantom with T2* properties within biological constraints. We determined that separate phantoms were required for DECT and PS-MRI. We analyzed two calcium-containing compounds—hydroxyapatite and calcium chloride—and five iron compounds, including iron(III) oxide, iron dextran, iron(II) chloride, iron(III) chloride, and human

hemoglobin. Out of these materials, the final MRI phantom was made from hydroxyapatite, iron dextran, iron(III) chloride, and hemoglobin.

One of the original goals of this work was to find a compound that could be used for both an MRI phantom and DECT phantom at the same concentrations. This goal was not met because that MRI is significantly more sensitive to the presence of paramagnetic materials such as iron than is CT. Concentrations of iron oxide high enough to mimic the appearance of hemorrhage on SECT and DECT (utilized by Nute et al. (135)) induced significant artifacts on T2*-weighted pulse sequences, and demonstrated virtually no signal at the TEs examined. Since iron oxide is not soluble in water, it would have been difficult to lower the concentration further compared to what was used in the lower concentration phantom. Therefore, iron oxide was eliminated as a possibility for modeling hemorrhagic lesions on MRI.

Since one of the primary drawbacks of using iron oxide in an MR phantom was insolubility in water, we focused on utilizing iron compounds that were easily dissolved in water. While many studies have used superparamagnetic iron oxide nanoparticles, as found in ferumoxytol (Feraheme; AMAG Pharmaceuticals, Waltham, MA), these would feature a very high magnetic susceptibility for a given iron concentration, and thus were ruled out. Instead, we chose to use iron dextran, another compound, like ferumoxytol, that is used to treat anemia intravenously. Iron dextran is soluble in water, and at appropriate concentrations (0.4 – 5.6 mg Fe/mL), was shown to have T2* values consistent with the literature for pathologically iron-laden tissues. It should be noted that this compound did shorten T1, so care must be taken to use this in phantoms appropriately since it will not adequately simulate the T1 properties of hemorrhage.

Iron chlorides were yet another option for an MR hemorrhage model. Iron exists in both the 2+ and 3+ oxidation states in the body (218, 219), and hematomas exhibit different T2* properties

as the lesion progresses from acute to chronic states and the density and oxidation states change (3, 26, 220). Chronic hemorrhage, heavy in the iron storage proteins hemosiderin and ferritin, and most forms of hemoglobin primarily contains iron in the more stable 3+ oxidation state (218, 219). Since Fe^{2+} can bind oxygen, it is primarily located in deoxyhemoglobin in patients with normal iron metabolism; however, when Fe^{2+} is found outside in tissues, it can induce tissue damaging free radical formation (220-222). This potential for iron-related damage to normal brain tissue due to disordered iron metabolism may be a factor in certain neurological diseases such as Parkinson's disease (221-223). However, due to the possibility that we may see more than one stage of hemorrhage or iron deposition due to multiple etiologies, we investigated the use of both iron(II) and iron(III) chloride in phantoms. We found that iron(II) chloride had a much higher T_2^* at similar iron concentrations compared to iron(III) chloride. Studies in the literature indicate that at a magnetic field strength of 3.0 T, the T_2^* of normal tissues ranged from 13.8 to 45.5 ms in seven male cadavers (age 38-81 years, mean age 52.3 years) (209, 224). In comparison to those biological values, the lowest T_2^* found in the iron(II) chloride samples was 84.96 ms. Therefore, we excluded iron(II) chloride from subsequent phantoms and analysis.

Iron dextran was investigated for potential use as a DECT phantom material, but we found that adequate separation of the hydroxyapatite and iron dextran was not possible using the methods developed by Nute et al. (135). Iron oxyhydroxide, which contains sulfur, is the primary iron-containing compound in iron dextran (225). The addition of sulfur increases the attenuation due to photoelectric effect compared to the iron-containing compounds found in the body (226). Despite the lack of translation of an iron compound from CT to MRI phantoms, hydroxyapatite—also utilized by Nute et al.—was the material selected to model calcific lesions over calcium chloride. Calcium chloride did not demonstrate a T_2^* value comparable to clinical studies for a given SECT HU (212). Hydroxyapatite does have limitations, however. The

material is not soluble in water, and therefore must be carefully emulsified, typically overnight, and manually shaken to achieve uniformity in agarose gels. While a magnetic stir bar was used to aid the emulsification process, adequate emulsification was not possible when concentrations exceeded approximately 275 mg/mL.

The final phantoms utilized for the study were comprised of hydroxyapatite, iron dextran, iron(III) chloride, and lyophilized human hemoglobin (as a biological reference). The MFGRE and SWAN data acquired for these two phantoms will be used in a future analysis (see Chapter 4). The calibration phantom will allow for direct comparisons of iron and calcium content in human tissue based on comparisons of the $T2^*$ and eventually magnetic susceptibility (See Chapter 4 for an evaluation of phase-sensitive MR techniques in these phantoms). The second of these biological phantoms features mixed lesions with various combinations of iron and calcium compounds as well as vials containing masses of other materials within a uniform background containing iron. It is particularly important to assess how well susceptibility mapping maintains lesion sizes in the presence of high susceptibility lesions, and we plan on testing this in phantom RF2. We showed in this chapter that lesions with masses featuring two dramatically different $T2^*$ values are best modeled using a voxel-wise analysis of the relaxation parameters. However, a biexponential fit of the mean signal across TEs provides a better fit than a monoexponential, and can potentially be used to estimate the two $T2^*$ values to within approximately 5 ms. Using this additional analysis may be useful to determine whether lesions in patients may contain more than one compound or density.

In making the final phantoms (Phantoms RF1 and RF2), there were several limitations. Hemoglobin is soluble in water to 20 mg/mL, but to adequately match the concentrations found in human blood, higher concentrations were necessary. Therefore, hemoglobin was the only material dissolved in Lactated Ringer's solution, which increased the solubility to over 200

mg/mL. There may be slight differences in the $T2^*$ calculations caused by changing the background material from agarose, which itself modifies $T2$ proportionally with its viscosity (227, 228). In the final phantom with mixed lesions, the concentration of the background agarose was raised to 2% weight/volume to keep the material in the masses, particularly the iron compounds, from bleeding into the surrounding agar background. However, this caused the agarose to solidify quickly, and several of the masses were mispositioned in the vials and could not be adequately imaged. The masses of the most interest, the calcific masses surrounded by iron dextran, were all readily visible, and so forming new samples and rescanning was deemed unnecessary.

We also limited the data used in the $T2^*$ calculations for all but the final phantom to the mean over five images per vial. The $T2^*$ calculations in the final phantom were based on calculations for each voxel within an ROI. While this voxelized $T2^*$ mapping is possible and provides additional information about the spatial variation in $T2^*$, since the majority of the phantoms were meant to validate the general MR properties of the materials with a simple methodology, we did not undertake this more computationally intensive analysis in every phantom at this point.

Magnetic Resonance Imaging Acquisition and Processing

4.1 Introduction

As discussed in Section 2.5, T2*-weighted Gradient Recalled Echo (GRE) pulse sequences are highly sensitive to changes in the magnetic susceptibility of tissues. It is the most commonly utilized sequence in the clinic for identifying chronic intracranial bleeds, cerebral microbleeds, and iron deposits. These lesions appear as black spots, representative of signal loss, and are known as “foci of susceptibility.” However, the specificity of this image type is limited since calcific lesions appear identical to hemorrhage due to their low proton density and diamagnetic characteristics.

The goal of this study was to utilize the phantoms developed in Chapter 3 to determine which pulse sequences and post processing algorithms provided the highest specificity for distinguishing calcification and hemorrhage. The methods investigated for this purpose include susceptibility weighted angiography (SWAN) sequence filtered phase images, background subtracted phase images from Projection onto Dipole Fields (PDF), and quantitative susceptibility mapping (QSM).

4.2 Methods

4.2.1 Phantoms

The phantoms used for this study included phantoms RF1 and RF2 from Chapter 3.3.5. Phantom RF1 provided calibration data for hydroxyapatite, iron dextran, iron(III) chloride, and hemoglobin at various concentrations (Table 3.5). Phantom RF2 focused on mixtures of the

materials present in RF1 as well as testing the feasibility of differentiating small calcific masses from hemorrhage models (Table 3.6).

4.2.2 MRI Scan Protocol

All phantom imaging was performed on a 3.0-T MRI system (MR 750, General Electric Healthcare) with an 8-channel head coil. The phantoms were positioned with the vials parallel to B_0 to minimize blooming. A three-dimensional (3D) T1-weighted ultrafast gradient echo with magnetization preparation (IR-FSPGR) was acquired to assess geometric accuracy near the vials. 3D susceptibility-weighted angiography (SWAN) sequence was acquired to examine the background phase—which is automatically reconstructed—in each material, and we acquired a 3D multi-echo fast gradient recalled echo (MFGRE) for generating both background-subtracted phase imaging with PDF and susceptibility distributions from QSM. Protocol details are in Table 4.1. The SWAN and MFGRE sequences were each acquired three times to check the repeatability of the test metrics.

Table 4.1: MRI acquisition details for all phantom experiments, including repetition time (TR), inversion time (TI), receive bandwidth (BW), field-of-view (FOV), acquisition matrix

Sequence	IR-FSPGR	3D SWAN	3D MFGRE
<i># of Echo Times</i>	1	6	12
<i>TE (ms) [min, max]</i>	2.1	23.3 ^a	[4.7, 61.4]
<i>TR (ms)</i>	5.7	37.6	65.2
<i>TI (ms)</i>	400	-	-
<i>Flip Angle</i>	20°	15°	20°
<i>BW (kHz)</i>	128	128	128
<i>FOV (mm)</i>	220	220	220
<i>Phase FOV (% of FOV)</i>	80	80	80
<i>Matrix</i>	256 x 256	320 x 224	416 x 320
<i>Slice Thickness (mm)</i>	1.4	1.4	1.4
<i>Scan Time</i>	4:27	2:49	6:46

^a SWAN provides images that are a weighted average of the six echoes. The average TE is listed here.

4.2.3 Phase-Sensitive MR Post-Processing

Post-processing of the SWAN sequence was performed at the scanner by selecting the option to reconstruct a high-pass filtered phase image from the k-space data. Real, imaginary, and magnitude images were generated for all echoes of the MFGRE pulse sequence at the scanner; additional processing for the MFGRE was performed on an external workstation (2.8 GHz Dual-Core Opteron Processor 8220 (Advanced Micro Devices, Santa Clara, CA) with up to 128 GB of RAM). The phase data was calculated from the real and imaginary images; a temporal phase unwrapping algorithm developed by Kressler et al. was used to calculate a map of the measured magnetic field (180, 183). Aliased frequencies in the magnetic field map were removed using the method described by Liu et al. (183). The final background-removed phase image was calculated using the Projection onto Dipole Fields (PDF) method (154), which eliminated phase shifts caused by non-local susceptibility effects (i.e., the air-phantom boundary). The resulting field map from the PDF was used as an input to morphology-enabled dipole inversion (MEDI) QSM processing (167, 182), which returned a map of the magnetic susceptibility within the phantom in units of parts per billion (ppb).

4.2.4 Image Analysis

Phantom RF1

For each acquisition, regions-of-interest (ROIs) were defined for each vial on five consecutive images to create larger volumes-of-interest (VOIs). The same VOIs were applied to the SWAN filtered phase images, the PDF results, and the QSM images. The mean of each VOI was then calculated for a given acquisition. The standard deviation of the VOI mean over three acquisitions was calculated for each sample and image type. Calibration curves for each image type and material were defined by linear regression of the signal versus material concentration (in mg/mL for hydroxyapatite and mg Fe/mL for iron-containing samples).

Phantom RF2

In phantom RF2, VOIs were defined spanning five consecutive images within each sample. The mean and standard deviation in the VOI across the three acquisitions were calculated. By plugging the known composition of each lesion model into the QSM calibration curves and taking the sum of the two material susceptibilities, we determined whether the expected susceptibilities were additive. The percent error was calculated relative to the predicted value. The diameter of a hydroxyapatite masse located within a hemorrhagic model (ID/HAPm 1) was measured on both the IR-FSPGR and QSM images to determine the geometric accuracy of the QSM images. The measurements were made by placing a line profile across the widest portion of the hydroxyapatite mass in five consecutive images. The diameter was calculated using the full width half max (FWHM) of the mass for both image types. The percent error was calculated relative to the IR-FSPGR, which has better geometric accuracy than the MFGRE pulse sequence that the QSM is based on.

4.2.5 Statistical Analysis

In phantom RF1, the mean values of the defined VOI for each acquisition were grouped into categories of hemorrhagic or calcific lesion models. Receiver operating characteristic (ROC) analysis was performed to determine the optimal threshold between the diamagnetic hydroxyapatite samples and the paramagnetic iron samples. The diameters of the hydroxyapatite mass as measured on the IR-FSPGR and QSM sequences were compared using a two-sided Student's t test with $\alpha = 0.05$.

4.3 Results

4.3.1 Phantom RF1 Analysis

The mean and standard deviation within each sample is reported in Table 4.2. In the hydroxyapatite samples, linear fits of the SWAN filtered phase, PDF, and QSM had negative slopes with hydroxyapatite concentration (Figure 4.1). While the SWAN phase demonstrated a negative trend with increasing hydroxyapatite content, the R^2 was only 0.437, and the phase

does not decrease monotonically. For linear fits of the same VOIs on PDF and QSM images, the R^2 values were 0.927 and 0.830, respectively, which indicated a tighter relationship with concentration than for the SWAN filtered phase images. In the iron-containing samples, SWAN filtered phase images also demonstrated poor fits with iron concentration for all three materials tested (Figure 4.2). The slope of the fit for hemoglobin was also negative while the fits for iron dextran and iron(III) chloride were positive, making it difficult to distinguish between potentially diamagnetic and paramagnetic materials (Figure 4.2a). In the iron-containing samples, PDF and QSM both had better fits overall than the SWAN phase images. However, QSM processing had a much tighter fit for the iron(III) chloride samples ($R^2 = 0.972$) than PDF did ($R^2 = 0.367$). This difference may be attributable to the spherical mean value (SMV) processing used within the QSM algorithm that is not used on the final PDF image. SMV computes the mean of a sphere several voxels in diameter for all voxels within the image, which effectively eliminates outlier voxels within uniform regions of the phantom (229).

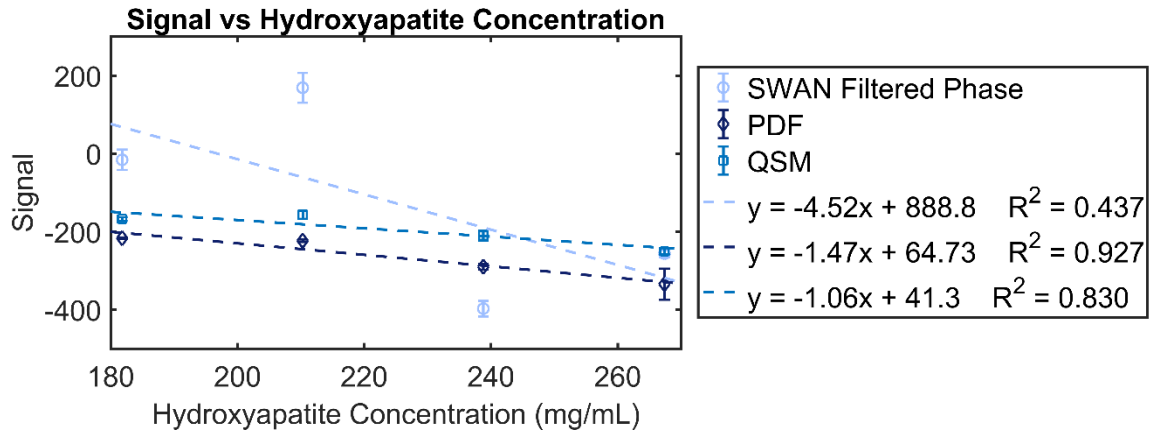


Figure 4.1: SWAN filtered phase (in mrad), PDF (in mrad), and QSM (in ppb) means for the hydroxyapatite samples. Error bars represent the standard deviation in the mean value across three acquisitions.

Table 4.2: Mean and standard deviation in phantom RF1 for the SWAN filtered phase, PDF, and QSM images. Concentration for hydroxyapatite is given in units of mg/mL while iron-containing compounds are reported in mg Fe/mL. Values marked by an asterisk have high variability between acquisitions and correspond with the samples with the highest magnetic susceptibility in the phantom.

Compound	Concentration (mg Fe/mL or mg/mL ^{**})	SWAN Filtered Phase (rad)	PDF (ppb)	QSM (ppb)
Hemoglobin	0.17	82.1 ± 3.9	174.6 ± 0.6	232.3 ± 5.4
	0.34	-63.3 ± 4.2	307.5 ± 1.1	436.6 ± 7.0
	0.42	168.9 ± 19.6	366.9 ± 1.0	461.5 ± 7.3
	0.53	-304.4 ± 16.8	695.2 ± 0.9	643.5 ± 5.7
Iron Dextran	0.70	7.6 ± 0.7	628.9 ± 1.4	738.4 ± 1.6
	1.40	-54.0 ± 4.0	1215.3 ± 3.8	1349.4 ± 8.5
	2.10	68.2 ± 4.9	1829.4 ± 2.4	2071.5 ± 14.0
	2.80	5.0 ± 8.2	2414.6 ± 4.9	2536.1 ± 31.3
Iron(III) Chloride	0.31	35.3 ± 2.3	1007.4 ± 2.9	862.9 ± 5.5
	0.62	-21.6 ± 19.4	2475.2 ± 20.9	2072.4 ± 24.9
	0.94	11.0 ± 75.7	1675.2 ± 9464.3*	837.2 ± 3054.8**
	1.25	53.2 ± 1.8	3501.2 ± 920.6*	3363.8 ± 407.4**
Hydroxy- apatite**	181.8	-15.9 ± 26.3	-216.9 ± 1.9	-167.7 ± 4.7
	210.3	168.7 ± 38.4	-223.6 ± 3.3	-157.1 ± 10.3
	238.8	-397.7 ± 19.9	-290.0 ± 7.6	-210.6 ± 12.8
	267.4	-256.7 ± 9.3	-334.9 ± 40.0	-250.6 ± 7.5

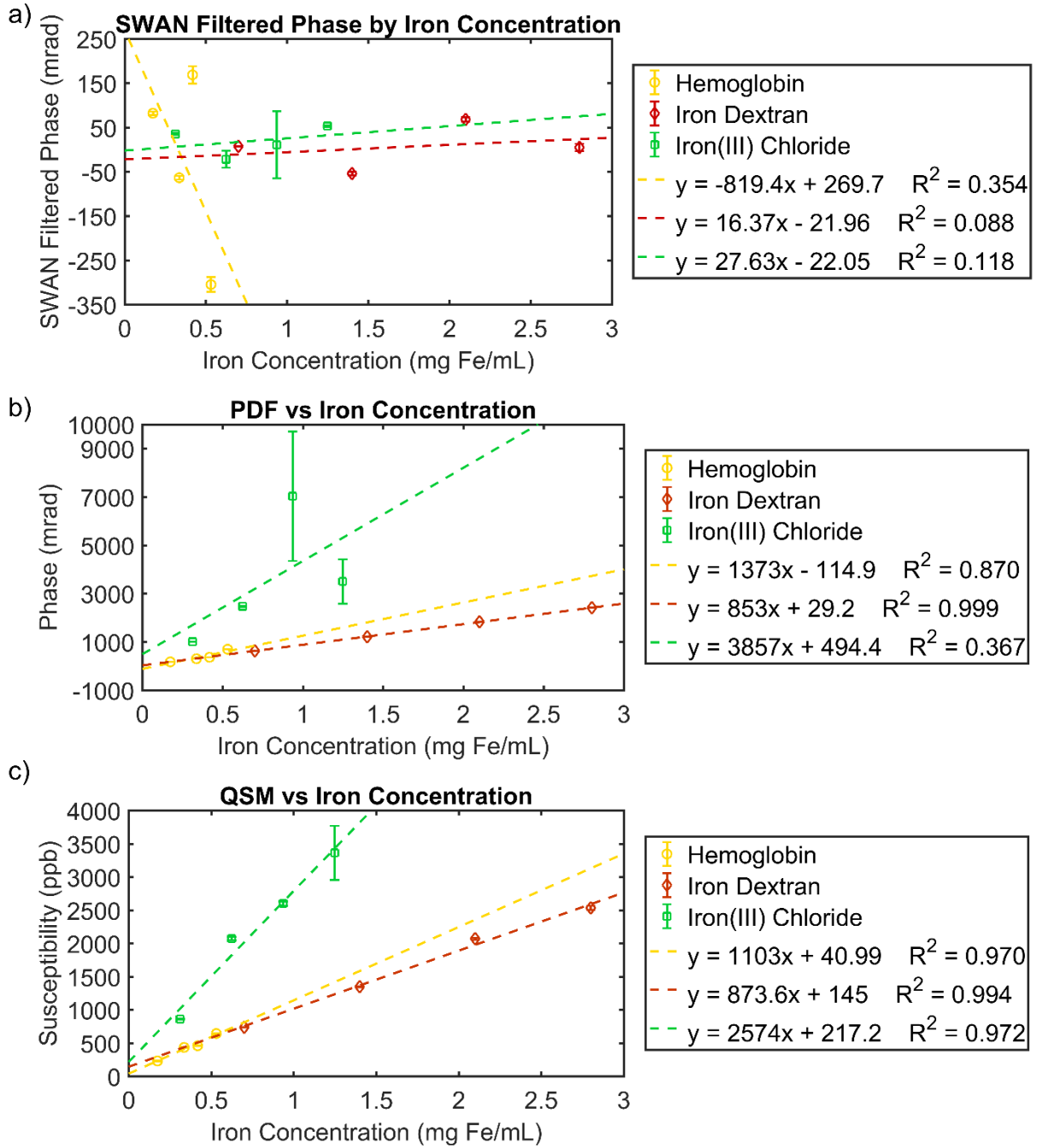


Figure 4.2: Hemoglobin, iron dextran, and iron(III) chloride signal on a) SWAN filtered phase, b) PDF, and c) QSM images versus iron concentration. The error bars represent the standard deviation of a VOI measurement across three acquisitions. Note that the mean and standard deviation in an iron(III) chloride samples with the highest iron concentration each excluded an extreme outlier in both the PDF and QSM fits (see Figure 4.3).

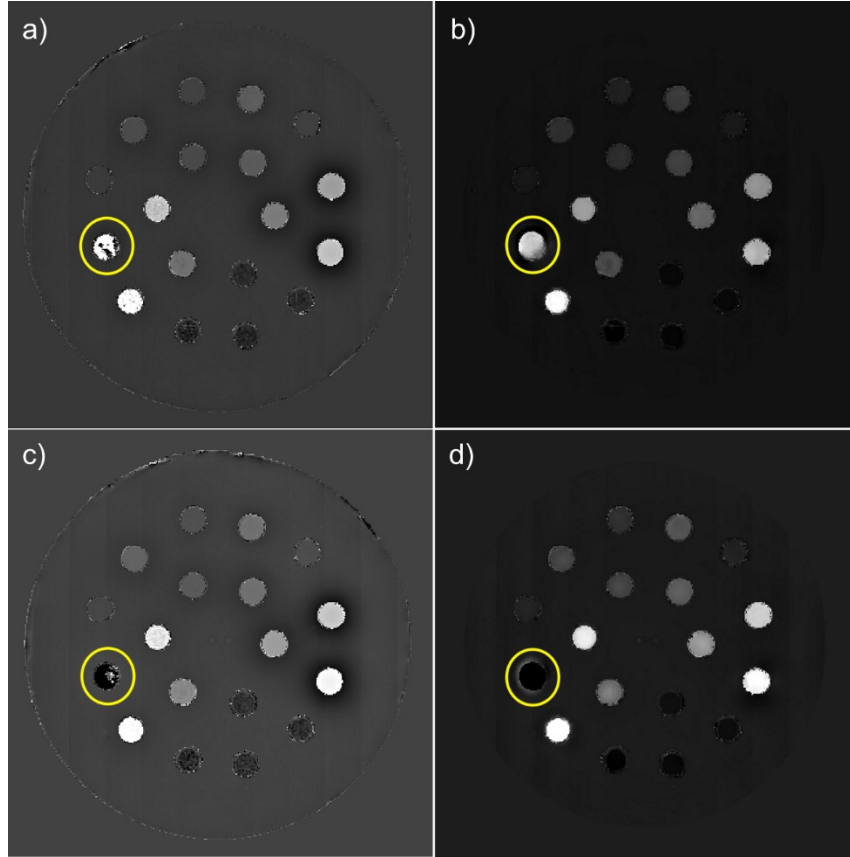


Figure 4.3: Images of phantom RF1 demonstrate the impact of poor phase unwrapping in the PDF and QSM processing for an iron(III) chloride sample (yellow circles). The acquisition shown in the top row shows a primarily positive phase on PDF (a) with some residual phase wraps, but a positive QSM proportional with its iron concentration (b). The bottom row is another acquisition in the same scan session where the phase has a 2π shift in the PDF (c), and thus the estimated susceptibility was negative (d).

4.3.2 Phantom RF2 Analysis

The predicted susceptibility for each mixture within the phantom is given in Table 4.3. The percent errors relative to the predicted value were very high for all material combinations except that of iron(III) chloride and iron dextran, which had a maximum error of 20.4%.

Therefore, we have experimentally verified that susceptibility is not an additive quantity in these lesion types in most cases.

Table 4.3: Predicted susceptibility based on the mixture concentrations in phantom RF2 input into the calibration curves for QSM defined in Phantom RF1. These values were compared to the measured susceptibility in the mixtures, and the percent error was calculated

Label	Predicted Susceptibility	Measured Susceptibility (ppb)	Percent Error (%)
HAP/ID 1	1798.0	870.1 \pm 0.5	-51.6 \pm 0.1
HAP/ID 2	1186.5	806.3 \pm 45.2	-32.0 \pm 3.8
HAP/ID 3	575.0	276.3 \pm 46.2	-51.9 \pm 8.0
IC/ID 1	1877.7	1897.6 \pm 47.4	1.1 \pm 0.2
IC/ID 2	1771.7	1634.4 \pm 49.9	-7.7 \pm 0.1
IC/ID 3	1691.3	1345.9 \pm 3.2	-20.4 \pm 0.4
Hb/ID 1	1172.5	697.5 \pm 0.8	-40.5 \pm 2.5
Hb/ID 2	1290.8	858.3 \pm 5.7	-33.5 \pm 2.8

The diameter of a hydroxyapatite lesion was assessed using FWHM measurements on the IR-FSPGR and QSM image sets. The mean diameter (\pm one standard deviation) was 5.04 ± 0.11 mm on the IR-FSPGR and 3.14 ± 0.13 mm on the QSM. The measured diameter on QSM was 1.90 mm (95% confidence interval: [1.79,2.02]), and the difference was statistically significant, with a p-value < 0.001 .

4.3.3 Statistical Analysis

Histograms of the individual VOI means for all iron-containing samples (red), and hydroxyapatite samples (blue) in Phantom RF1 and RF2 are shown in Figure 4.5. The optimal threshold to differentiate between the calcific and hemorrhagic lesion models were determined to be -69.9 mrad, 174.0 mrad, and 228.0 ppb for SWAN filtered phase, PDF, and QSM images, respectively. These thresholds resulted in a sensitivity values of 91.7%, 97.2%, and 97.2% and specificity values of 50.0%, 100%, and 100% for the three image types. PDF and QSM had identical performance metrics (AUC = 0.972) since there was a single iron measurement that was a known outlier (Figure 4.3, Figure 4.5) caused by an error in phase unwrapping. In contrast, the SWAN phase data returned an AUC of 0.644 (Figure 4.4).

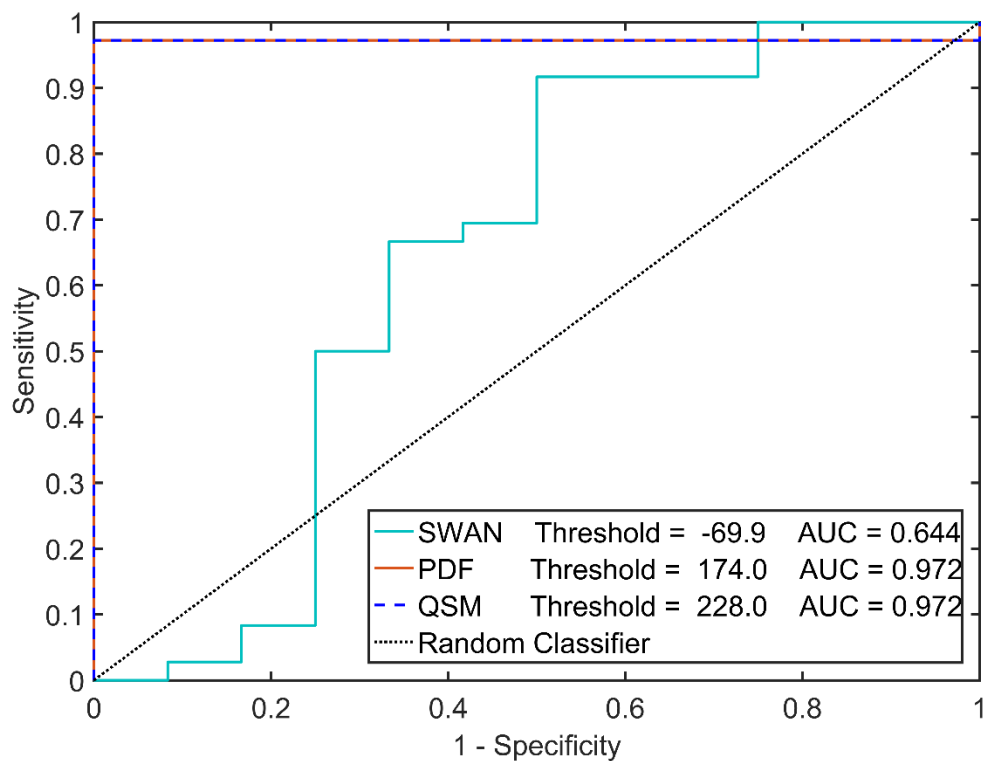


Figure 4.4: ROC analysis for SWAN filtered phase, PDF, and QSM data. The threshold indicates the threshold for which the sum of the true positive rate and the false negative rate were optimized. AUC is defined as the area under the curve.

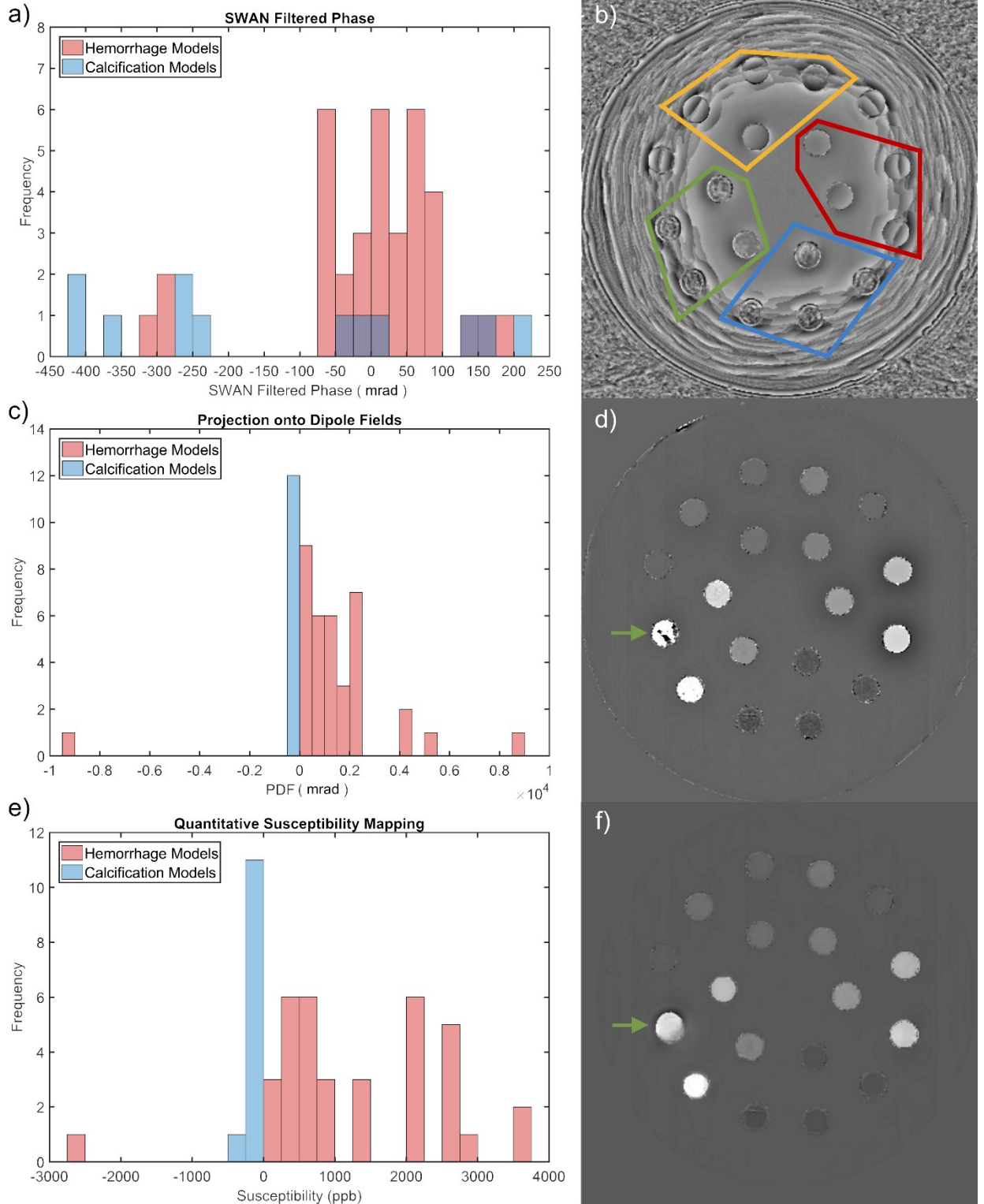


Figure 4.5: Histograms of the mean in all calcific and hemorrhagic lesion models over three acquisitions for SWAN filtered phase (a), PDF (c), and QSM (e) data. Representative images of phantom RF1 are included for the three image types: b) SWAN Phase, d) PDF and f) QSM. The colored polygons indicate the material within the samples:

hydroxyapatite (blue), iron dextran (red), iron(III) chloride (green), and hemoglobin (gold). Units for the SWAN and PDF images are milli-radians; QSM is in units of ppb. One iron(III) chloride sample (green arrows) had errors in the phase unwrapping (d), which were improved in the QSM (f).

4.4 Discussion

We found that the QSM had the best correlation with material concentration out of the three image types tested. There have been several studies demonstrating that the susceptibility of iron relative to water is between 0.55 and 1.30 ppb per ppm (by mass) of iron in wet tissue (176, 209, 224) or approximately 0.14 ppb per ppm iron in dry tissue (230). Since 1 mg Fe/mL is equal to 1000 ppm, the slopes calculated in the calibration curves in this study represented 1.10, 0.87, and 2.57 ppb of susceptibility per ppm of iron for hemoglobin, iron dextran, and iron(III) chloride, respectively. This is largely in agreement with the literature studies in humans.

As shown in Figure 4.5b, the SWAN filtered phase images do not provide sufficient phase unwrapping as far as 4 cm away from the edge of the phantom. There was not a large enough uniform region to determine if the phase would change monotonically with concentration were they more centrally located. While ideally a larger phantom would be used to counteract this problem with the phase non-uniformities, the size of the head coil limits the overall size of the phantom. Patient images that fail to have complete phase unwrapping may limit the capacity of radiologists to differentiate between diamagnetic and paramagnetic materials, as it has within this phantom. The default SWAN filtered phase images themselves have not been reported on extensively in the literature. However, similar sequences from other vendors have demonstrated significant phase aliasing in lesions when the phase is processed with a high pass filter (144, 231).

In comparison to the SWAN filtered phase images, both the PDF and QSM signal correlated much better with material concentration for all material types. The signal within PDF images is

proportional to the local magnetic field changes (relative to the main magnetic field) caused by the presence of the phantom; in comparison, the QSM signal is equal to the inherent magnetic susceptibility of the materials in a given voxel. Because the presence of a material with a large susceptibility causes changes in the local magnetic field, they are closely related. However, due to the dipole moment of a susceptibility source, there are phase differences in the surrounding material that are caused by the susceptibility source some distance away. The non-local phase effects can lead to artifacts around the vials in the PDF images (Figure 4.5d) that are removed during QSM processing (Figure 4.5f). Therefore, the overall image quality of the QSM may be higher than that of the PDF.

Problems with phase unwrapping also impacted portions of the PDF and QSM processing pipeline in specific circumstances. In one iron(III) chloride sample with relatively high susceptibility, the PDF presented with a phase shift of 2π in one of the three acquisitions. This translated to a measured susceptibility in the lesion model where the magnitude of the susceptibility was correct, but the sign was negative. The issue was traced back to an error in the phase unwrapping of the initial field map, which affected both the PDF and QSM. Since lesions with lower and higher concentrations of the material were successfully unwrapped, we assume that this is a problem only at specific susceptibility levels that cause aliasing in the field map frequency. In the literature, it has been documented that acute hemorrhage featuring primarily deoxyhemoglobin has a maximum susceptibility of approximately 1.60 ppb (232); in comparison, this lesion had an estimated susceptibility of 2.50 ppb. In phantoms, we will be able to develop an algorithm to correct this issue. However, since the composition of lesions within the body is not known a priori, it will be difficult to implement in patient exams without additional testing. Adjusting the pulse sequence parameters may be a better long term solution to avoid phase aliasing within the expected frequency range.

We found very good agreement in the QSM across acquisitions. In phantom RF1, the largest standard deviation across acquisitions—in all but those samples with uncorrected phase wraps—was 31.3 ppb. One study performed QSM in two normal volunteers that were scanned at 10 different sites, and in the tissues evaluated, the intra-subject coefficient of variation was under 10% (233). Since that study only evaluated healthy patients, they measured a maximum susceptibility of approximately 0.14 ppm; in comparison, the highest susceptibility in this study (without phase aliasing) was 2.54 ppm to represent an acute or chronic hemorrhage (233). The variance in our study increased with higher iron levels, so in patients with lesions, the coefficient of variation may increase.

In phantom RF2, we investigated whether we could predict the susceptibility of a lesion by summing the calibration curve-derived susceptibility of multiple materials. This simple phantom experiment demonstrated that even in a controlled environment, the susceptibility of multiple materials is not an additive quantity. Since the susceptibility is proportional to the number of free electrons in a material, mixing materials increases the chance of interactions that will bind free electrons, hence modifying the susceptibility properties. An example of the phenomenon is that while we would expect that mixing diamagnetic hydroxyapatite with paramagnetic iron dextran would lower the overall susceptibility slightly, depending on the concentrations mixed; there can be a difference of over 50% (Table 4.3). Meanwhile, mixing iron dextran and iron(III) chloride did not result in large deviations from the predicted susceptibility. Since we cannot estimate the susceptibility in a controlled phantom environment, we must take caution when comparing phantom data to human data. The iron concentrations that provide a specific susceptibility in phantoms may not translate precisely to human data due to the difference in tissue background.

There are several limitations to this phantom study. First, the ratio of Fe^{2+} to Fe^{3+} in the human hemoglobin samples could not be controlled since it was in contact with room air in its packaging. Hemosiderin, the primary component of chronic hemorrhage was also not available for testing. As previously discussed, the phantoms also are not a perfect substitute for human tissue. We did not perform T1- or T2-mapping to determine how biosimilar the background material was to brain tissue because we were primarily focused on modeling the T2* effects found in hemorrhagic lesions.

Lesion Differentiation in Human Subjects with DECT and PS-MRI

5.1 Introduction

The correct characterization of intracranial low-density calcification and hemorrhage is a challenging clinical problem that may have a direct impact on both diagnosis and clinical management. We have identified two promising methods for distinguishing between these two lesion categories: dual-energy CT (DECT) and quantitative susceptibility mapping (QSM). DECT provides material differentiation through interrogation of the lesion by more than one x-ray spectra, in effect allowing the photoelectric effect and Compton scattering components of attenuation to be determined. In comparison, the goal of QSM is to map the magnetic susceptibility of tissue, for which diamagnetic calcium should return a negative susceptibility while paramagnetic blood products lead to a positive susceptibility measurement. There have been multiple studies in the literature regarding the differentiation of calcific and hemorrhagic lesions in the brain (45, 137, 205, 206). However, there have been no studies to date comparing these two complimentary modalities, nor have there been prospective clinical trials of these new technologies. Both modalities have the potential to provide uniquely valuable clinical information about these lesion types through two independent physical mechanisms: magnetic susceptibility and x-ray attenuation properties. This chapter details a prospective imaging trial in patients with brain lesions with the goal of identifying and characterizing intracranial calcifications and hemorrhage *in vivo*.

5.2 Methods

5.2.1 Study Population

Up to 100 evaluable adult patients with lesions at least 1.0 cm in diameter indicated by foci of susceptibility on conventional MR or lesions on routine CT were to be recruited into this trial,

which was approved by the local Institutional Review Board. Subjects in the subset of the data presented here entered the trial between October 2016 and February 2018.

Table 5.1: Study inclusion and exclusion criteria. Additional contraindications to MRI can be found in Appendix 1

Inclusion Criteria	Exclusion Criteria
> 18 years of age	Failure to obtain consent
Foci of susceptibility ≥ 1 cm in size on T2*-weighted GRE of the brain	Contraindications to MRI <ul style="list-style-type: none"> • Incompatible implanted device • Claustrophobia
<u>OR</u>	
SECT lesion ≥ 1 cm in size and < 100 HU	Positive urine pregnancy test

5.2.2 Study Design

Study subjects were recruited from the set of MD Anderson patients undergoing T2*-weighted GRE imaging as part of routine clinical MRI of the brain. These studies were imported into screening software developed in house (see Appendix 2) on a daily basis. The software enabled the user to cycle through all patient datasets sequentially; trained study personnel marked images with a likely focus of susceptibility greater than 1 cm in at least one dimension for a neuroradiologist to review at a later time. Patients also could be referred to the study by a radiologist or their physician if they had a lesion of unknown composition greater than 1 cm in any dimension and a measured attenuation of under 100 HU on clinical SECT. This size threshold was chosen to qualify a patient for the trial because DECT analysis becomes less accurate as lesion size decreases below 1.0 cm, based on a preliminary study performed by our group (136). That study showed that for lesions with attenuations below 100 HU, differentiation of calcific and hemorrhagic lesions was not possible when the lesion size reached 0.5 cm in diameter; however, due to the limitations of the phantom design, we were unable to define a precise size threshold under which DECT did not provide additional information over SECT. Because lesions presenting with susceptibility on clinical T2*-weighted

GRE often appear larger than they would on pulse sequences that are less vulnerable to susceptibility artifacts, such as fast spin echo sequences, using 1 cm as a threshold on GRE images allowed for the inclusion of some slightly smaller lesions as measured by CT to qualify patients for the study. Furthermore, while a patient was required to have at least one lesion over 1.0 cm in diameter on T2*-weighted GRE, many patients had additional lesions present that were smaller that were also available for analysis.

From this subset of patients initially screened into the trial, the study radiologist (Dr. Dawid Schellingerhout) selected subjects with lesions of unknown composition for potential recruitment by a research nurse. The research nurses excluded patients if they declined to participate, were deceased or had entered hospice care, had an implanted device incompatible with 3.0 T MRI, had the lesion of interest resected, were no longer receiving care at our institution, or if they required an interpreter (due to lack of access at our small research center). All others were recruited to the study, with informed consent documented.

After screening and study enrollment by research staff, all patients (n = 52, 29 male and 23 female, aged 25 – 78 years [mean age \pm standard deviation: 59.1 \pm 12.8 years]) underwent non-contrast SECT, non-contrast DECT, and non-contrast MRI at the MD Anderson Center for Advanced Biomedical Imaging. Since many of the patients were recruited following screening MR, we expected that some lesions would have a SECT attenuation value greater than 100 HU. Therefore, following image registration of the PS-MRI and CT examinations, the analysis was separated into two arms (Figure 5.1):

- 1) Lesions with SECT attenuation \geq 100 HU, for which SECT can be considered a gold standard for the diagnosis of calcification, and

- 2) Lesions with SECT attenuation < 100 HU, where no existing gold standard is available, and for which analysis would be informed by the phantom analysis and concordance/discordance of the QSM and DECT analysis.

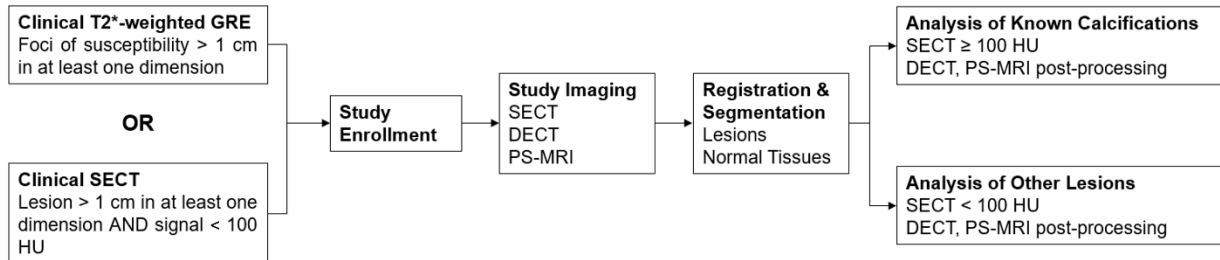


Figure 5.1: Study flowchart showing flow from screening to study enrollment and imaging, to the analysis of individual lesions in subsets of known calcifications and unclassified lesions.

5.2.3 SECT and DECT Imaging

SECT and DECT were acquired on a fast kVp-switching capable system (Discovery HD750 CT; General Electric Healthcare, Waukesha, WI). The SECT scan was identical to the clinical routine brain CT performed at our institution; the DECT protocol was informed by the work of Nute et al. (136), which indicated that accuracy improved with higher rotation times and CTDI_{vol}. These protocols are displayed in Table 5.2. Multiple image sets were reconstructed from the DECT exam. Material images with a calcium/water basis pair were generated (136).

Table 5.2: Study SECT and DECT imaging protocols. The scan range, image thickness, beam width, and field-of-view (FOV) were held constant between the two examinations.

Technique Parameter	SECT	DECT
<i>Scan Type</i>	Helical	Helical GSI
<i>Area</i>	Maxillary Teeth to Vertex	Maxillary Teeth to Vertex
<i>kVp</i>	120	80/140
<i>mA</i>	220	600
<i>Rotation Time (s)</i>	0.8s	0.9
<i>Pitch</i>	0.531	0.531
<i>CTDI_{vol} (mGy)</i>	65.2	132.6
<i>Image Thickness (mm)</i>	0.625	0.625
<i>Interval (mm)</i>	0.625	0.625
<i>Beam Width (mm)</i>	20	20
<i>Scan FOV</i>	Head	Head
<i>Display FOV (mm)</i>	250	250

5.2.4 MR Imaging

Imaging was performed on a 3.0-T MRI system (MR 750, General Electric Healthcare) with an 8-channel head coil. A three-dimensional (3D) T1-weighted ultrafast gradient echo with magnetization preparation (IR-FSPGR) was acquired for anatomical reference. A T2*-weighted GRE was acquired for comparison of the signal level for comparison to the clinical MR. A 3D susceptibility-weighted angiography (SWAN) sequence was acquired to examine the background phase—which is automatically reconstructed—in each material, and a 3D multi-echo fast gradient recalled echo (MFGRE) was acquired to assess signal changes with increasing echo time (TE) and calculate QSM images. Scan parameters are located in Table 5.3

5.2.5 Phase-Sensitive MRI Post-Processing

The first echo of the MFGRE (TE approximately 4.5 ms) was loaded into 3D Slicer to create a mask of the brain for Quantitative Susceptibility Mapping (QSM). The cerebrum, brain stem, and cerebellum were manually masked, and the resulting logical image set was loaded into

Matlab (R2016a; MathWorks, Natick, MA) for QSM processing along with the real and imaginary DICOM images from the MFGRE. QSM processing was performed using Morphology-Enabled Dipole Inversion, which included phase unwrapping and background phase removal using Projection onto Dipole Fields as preparatory steps (167, 234, 235). QSM reconstruction took approximately one hour per iteration, with an average of six iterations on a 2.8 GHz Dual-Core Opteron Processor 8220 (Advanced Micro Devices, Santa Clara, CA) with up to 128 GB of RAM available.

Table 5.3: MRI acquisition details for the patient trial, including repetition time (TR), inversion time (TI), receive bandwidth (BW), field-of-view (FOV), acquisition matrix

Sequence	IR-FSPGR	T2*-weighted GRE	3D SWAN	3D MFGRE
<i># of Echo Times</i>	1	1	6	12
<i>TE (ms) [min, max]</i>	2.1	15	23.3 ^a	[4.7, 61.4]
<i>TR (ms)</i>	5.7	600	37.6	65.2
<i>TI (ms)</i>	400	-	-	-
<i>Flip Angle</i>	20°	20°	15°	20°
<i>BW (kHz)</i>	128	128	128	128
<i>FOV (mm)</i>	220	220	220	220
<i>Phase FOV (% of FOV)</i>	80	75	80	80
<i>Matrix</i>	256 x 256	256 x 256	320 x 224	416 x 320
<i>Slice Thickness (mm)</i>	1.4	5	1.4	1.4
<i>Scan Time</i>	4:27	2:00	2:49	6:46

^a SWAN provides images that are a weighted average of the six echoes. The average TE is listed here.

5.2.6 Image Registration and Segmentation

Image registration and segmentation were performed in 3D Slicer (Version 4.6, Brigham and Women's Hospital, Boston, MA). All images were co-registered to the axial 3D T1-weighted MRI (due to its geometric accuracy) with an affine transformation (236). Foci of susceptibility were segmented on the first echo of the registered MFGRE (TE = 4.5 ms) to minimize blooming of the lesion. Known calcifications were identified on the registered SECT as those lesions with a mean attenuation greater than 100 HU, including physiologic calcifications in the pineal

gland, choroid plexus, and falx. Suspected calcifications less than 100 HU were also identified on the CT. A circular ROI was placed in the lateral ventricle as a control on the QSM images.

The ROI locations defined in 3D Slicer were saved and loaded into Matlab. Automated processing in Matlab was utilized to apply the ROIs to each registered image set for a given patient. For each ROI location and image type, the software saved the voxel data, calculated the ROI mean and standard deviation, and median.

5.2.7 Reference Standard

The current clinical standard for classification of brain lesions as either hemorrhagic or calcific is to assign all lesions with SECT attenuation greater than 100 HU as calcification.

Subsequently, both clinical and imaging features are used to make a probabilistic determination of hemorrhage or calcification for lesions under the 100 HU threshold. The following examples represent a brief, non-comprehensive demonstration of the clinical thinking that was used to define this clinical reference standard:

- Lesions that exhibited susceptibility on T2*-weighted GRE but were located in the pineal gland, choroid plexus, or dura mater were assigned as calcification if there were no other signs of bleeding on CT or MRI (237).
- For lesions in the brain parenchyma, the lesion was labeled as hemorrhage if it was iso- or hypo-intense on CT and exhibited significant blooming on T2*-weighted GRE compared to the 3D T1-weighted IR-FSPGR sequence or met the other criteria defined in Table 2.2.
- For lesions suspected of hemorrhage with hyperintensity on CT, the clinical history was examined to see if hemorrhage was clinically likely. For example, a history of known hemorrhagic metastases or recent treatment of a lesion with stereotactic radiotherapy were presumed to be hemorrhagic.

This clinical reference standard was applied to all lesions by our study neuroradiologist (DS, 18 years experience), making use of imaging data available from the study and prior routine brain studies, as well as clinical information available from the electronic medical record (such as a history of recent surgery or radiation). Clinical MR brain imaging at our institution included, but was not limited to, T1-weighted, T2-weighted, and T2 FLAIR pulse sequences. CT imaging prior to the study exam was not available for all patients.

5.2.8 SECT Analysis

Lesion data were collected on the SECT. Histogram analysis was performed to assess the current clinical ability of CT to differentiate between calcific and hemorrhagic lesions. Receiver Operating Characteristic (ROC) analysis was performed utilizing the clinically accepted threshold of 100 HU to differentiate between hemorrhage and calcification.

5.2.9 DECT Analysis

Lesion data were collected for a calcium/water two material decomposition. ROC analysis was performed on the water(calcium) and calcium(water) data individually compared to the reference standard. Logistic regression with 5-fold cross validation was performed in Matlab on the water(calcium) and calcium(water) with the initial clinical reference standard used as the classification metric to determine the probability that specific calcium and water measurements were indicative of either hemorrhage or calcification. The logistic fit equation is given by the equation below,

$$\ln\left(\frac{p(x_w, x_c)}{1 - p(x_w, x_c)}\right) = \beta_0 + \beta_w x_w + \beta_c x_c \quad \text{Equation 5.1}$$

where x_w represents the water(calcium) means and x_c represents the calcium(water) means.

β_0 , β_w , and β_c are the fitted coefficients for the logit model resulting from the logistic regression (238). Receiver operating characteristic (ROC) analysis was performed to determine the

sensitivity, specificity, and area under the ROC curve (AUC) for the DECT diagnostic task. The optimal cutoff for the ROC analysis was determined using the Youden index (J) (239):

$$J = \max(\text{Specificity} + \text{Sensitivity} - 1) \quad \text{Equation 5.2}$$

Diagnostic accuracy was calculated relative to the reference standard.

5.2.10 QSM Analysis

Measurements were made in the cerebrospinal fluid (CSF) of each patient, and the mean susceptibility recorded within each patient because CSF is primarily water, which has a known susceptibility ($\chi = -9.05$ ppm) (204). A Shapiro-Wilk test was performed on the CSF measurements to determine if the distribution of the measured susceptibility was gaussian. The QSM of a lesion was considered to be positive for hemorrhage if the measured susceptibility was greater than the group sample mean of the CSF measurements across patients, the lesion was considered hemorrhagic. If the lesion's susceptibility was lower than that of the group CSF sample mean, the lesion was considered to be calcific. ROC analysis was also performed to assess the performance of QSM for the differentiation of calcific and hemorrhagic lesions with an optimal cutoff at the Youden index (Equation 5.2). Diagnostic accuracy for each modality will be considered relative to the reference standard.

5.2.11 Statistical Analysis

McNemar's test was used to compare the binary DECT and QSM classifications—calcification or hemorrhage—for all lesions overall and within each subgroup (SECT < 100 HU and SECT ≥ 100 HU) to test for consistency in classification between the two modalities (240). The level of the concordance was assessed using Cohen's Kappa statistic (241).

The marginal utility of both DECT and QSM will be determined by comparing the ROC analysis of the individual modalities to the ROC characteristics of SECT alone (242, 243). The optimal thresholds for each modality were chosen from ROC analysis of the whole dataset.

5.3 Results

5.3.1 Study Population

Screening data is shown in Figure 5.2, including the total number of unique patients viewed by study personnel, the number of patients having a preliminary lesion marked, and the number of patients approved by the study's neuroradiologist for recruitment. Of the 754 patients deemed eligible for the study based on clinical T2*-weighted GRE imaging, a total of 702 were either excluded, declined to participate, or were unable to be contacted. A total of 52 patients were scanned from October 2016 to February 2018. Two patients were excluded from this analysis due to image artifacts due to motion in the MFGRE pulse sequence used to generate the QSM images. Within this population, there were a total of 328 total foci of susceptibility identified; the initial clinical classification used as a reference standard indicated 189 calcifications and 139 hemorrhagic lesions in total.

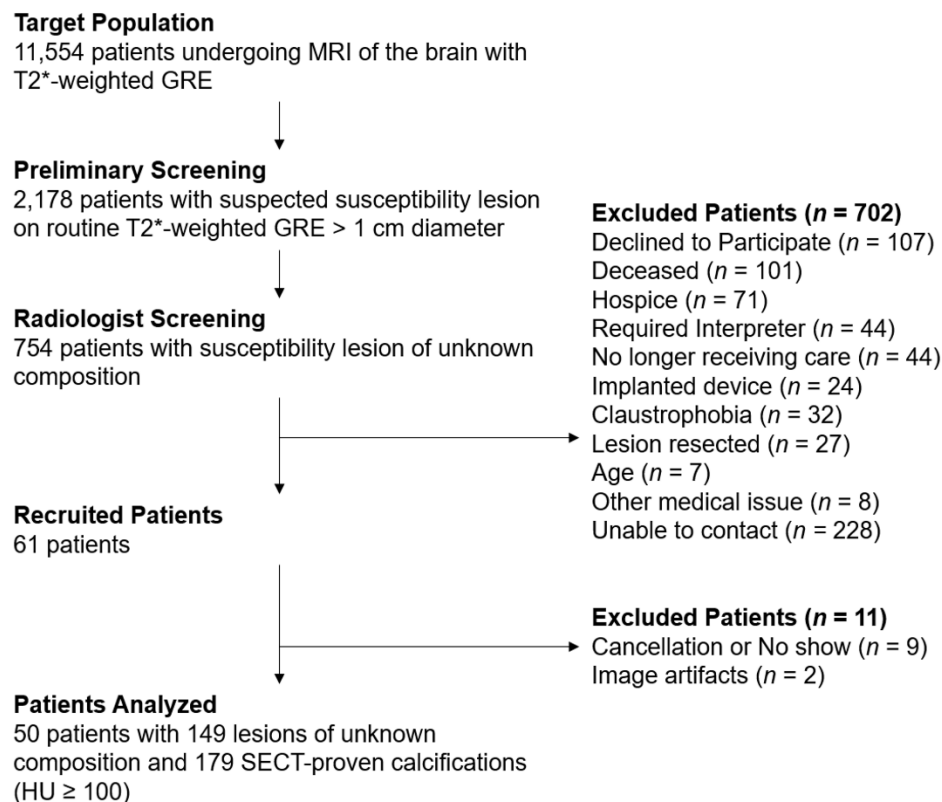


Figure 5.2: Subject accrual flow chart

5.3.2 SECT Analysis

There were a total of 179 lesions with a SECT attenuation greater than or equal to 100 HU. A histogram with kernel density estimates demonstrates the distribution of SECT HU for the hemorrhage and calcification groups as defined by the reference standard (Figure 5.3).

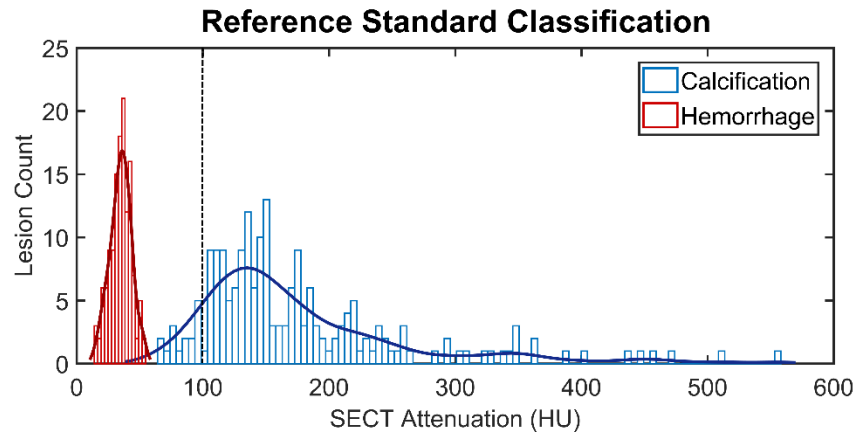


Figure 5.3: SECT values for lesions classified as hemorrhage and calcification by the reference standard. The dotted black line marks the current established threshold for differentiating between calcification and hemorrhage on SECT (100 HU). Note that applying this threshold rigidly would misclassify multiple calcific lesions as hemorrhagic, based on initial clinical classification.

While the kernel density estimates in Figure 5.3 overlap, the hemorrhage with the highest attenuation measured 53.7 HU; the calcification with the lowest attenuation measured 67.5 HU. As a result, any threshold between 53.7 and 67.5 HU would effectively separate the hemorrhage and calcification present in this dataset. The ROC analysis returned an optimal threshold of 67.5 HU, at which the accuracy, sensitivity, and specificity were all 100%. However, using a threshold of 100 HU, which is currently utilized clinically, has an accuracy of 95.1%, sensitivity of 100%, and specificity of 91.8%

5.3.3 DECT Analysis

ROC analyses of the calcium(water) and water(calcium) data returned optimal thresholds of 11.76 mg Ca/mL and 1030.7 mg H₂O/mL, respectively. The calcium(water) images provided better discrimination between the hemorrhagic and calcific lesions than the water(calcium) images (Figure 5.4). Combining the data from both DECT image types, the logistic regression of the calcium(water) and water(calcium) data returned the linear combination coefficients found in Table 5.4. The calcium(water) was the only statistically significant parameter in the fit. The calcium density is the primary predictor, which can be seen visually in Figure 5.6a, in which a line that represents the optimal threshold between the calcific or hemorrhagic lesions has been superimposed on a scatter plot. The threshold that optimized the Youden index (Equation 5.2) for the logit model was a linear metric ($\beta_0 + \beta_w x_w + \beta_c x_c$) of -2.68 (Figure 5.6b). The mean and standard deviation for each lesion type as defined in the model are in Table 5.5 for SECT, water(calcium), and calcium(water) image types, and the 2 x 2 classification matrices are in Figure 5.5. The overall accuracy of this model was 99.7% (327/328) amongst the entire dataset (Figure 5.5, Table 5.10), 100% (179/179) amongst SECT-proven calcifications, and 99.3% (148/149) amongst lesions with SECT < 100 HU. The sensitivity and specificity in the full dataset were 99.3% (134/135) and 100.0% (193/193).

Table 5.4: DECT logistic regression. The equation for the fit is given in Equation 5.1. A p-value of less than 0.05 represents the statistical significance of the parameter within the model (indicated by *).

	Coefficient	t Statistic	p-value
<i>Intercept</i> (β_0)	-122.900	-1.77	0.077
<i>Water(Calcium)</i> (β_w)	0.112	1.66	0.096
<i>Calcium(Water)</i> (β_c)	0.549	4.23	< 0.001*

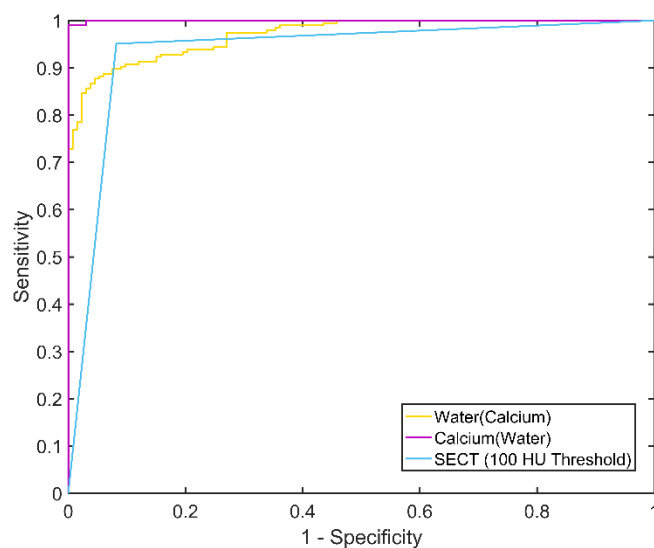


Figure 5.4: ROC curves for Water(Calcium) and Calcium(Water) data compared to the ROC curve for SECT with a threshold of 100 HU.

Table 5.5: Mean SECT, water(calcium), and calcium(water) measurements for lesions classified as hemorrhage and calcification in the DECT-based logistic regression.

<i>DECT Classification</i>	Hemorrhage (n = 133)		Calcification (n = 195)	
	<i>Mean</i>	<i>Standard Deviation</i>	<i>Mean</i>	<i>Standard Deviation</i>
<i>SECT (HU)</i>	34.9	8.3	177.6	86.1
<i>Water(Calcium) (mg/mL)</i>	1021.9	7.0	1048.7	16.7
<i>Calcium(Water) (mg/mL)</i>	5.2	2.1	44.7	24.4

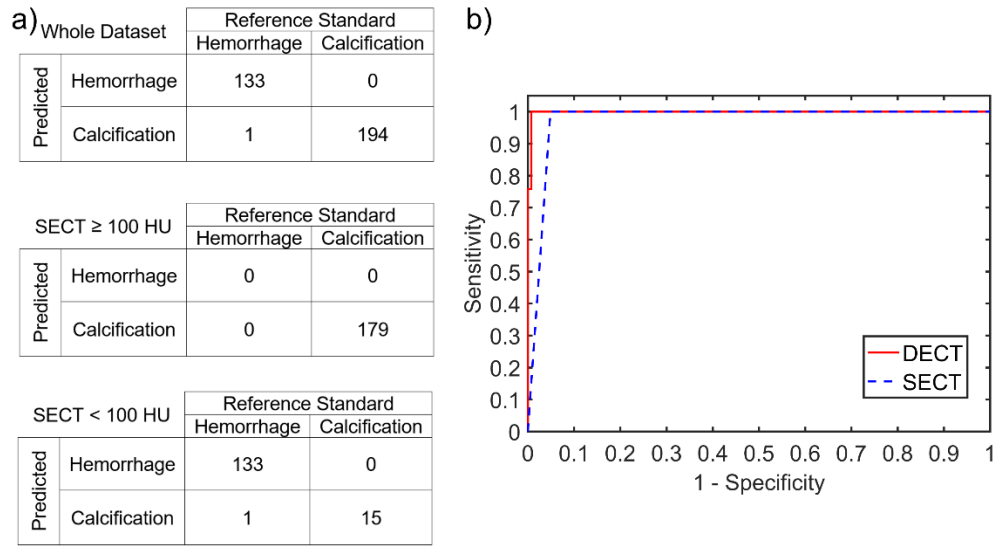


Figure 5.5: a) Classification matrices for the DECT-based logistic model compared to the reference standard and b) the ROC curve for the DECT and SECT classification schemes.

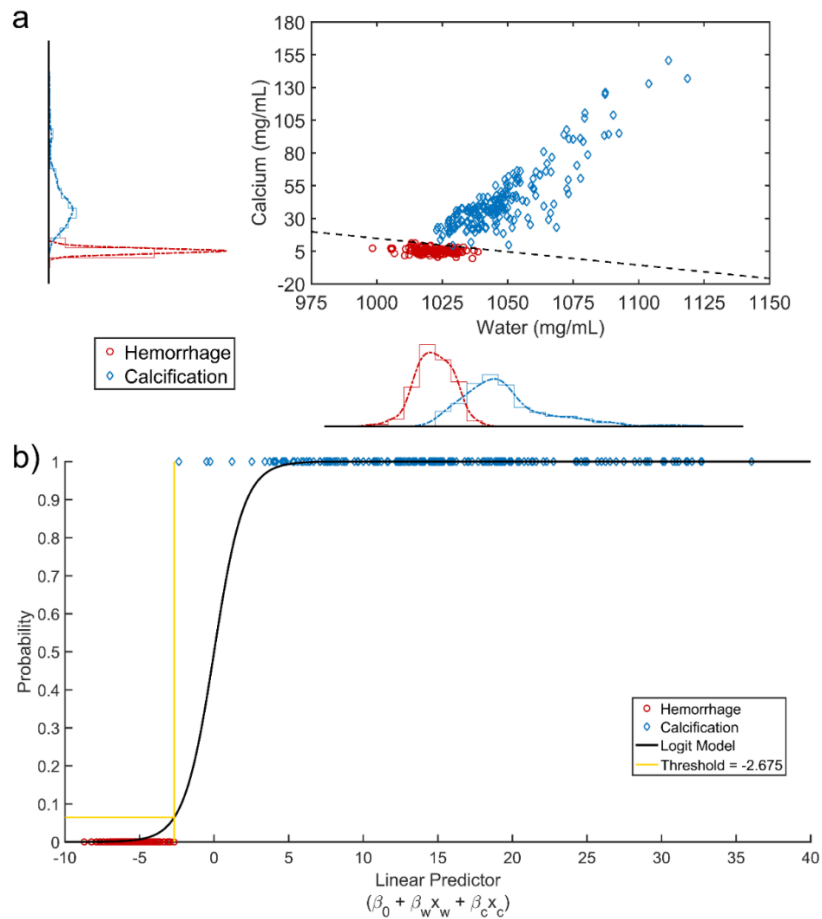


Figure 5.6: DECT water(calcium) and calcium(water) data classified by the reference standard. a) A scatter plot of the water(calcium) and calcium(water) means for all 328

lesions. The dotted black line represents the optimal threshold between calcification and hemorrhage in the logistic model, where a linear combination of the water and calcium data is equal to -2.675. b) The logistic regression compared to the reference standard.

5.3.4 QSM Analysis

Across the 50 patients studied, the mean susceptibility of CSF was 27.5 ± 10.1 ppb (Figure 5.7), and normality was confirmed with a Shapiro-Wilk test ($p = 0.71$). Of the 328 susceptibility lesions identified, by QSM, 192 lesions were classified as calcifications (-109 ± 129 ppb) and 136 as hemorrhage (730 ± 457 ppb) using the mean QSM of CSF as a threshold, for a total accuracy of 98.5% (323/328). However, a threshold set at 37.6 ppb (CSF mean plus one standard deviation) satisfies the Youden index (Figure 5.8). The means and standard deviations of the SECT and QSM for each classification are in Table 5.6, and scatterplots are showing the relationship between SECT and susceptibility are shown in Figure 5.9. Compared to the reference standard, the diagnostic accuracy using the 37.6 ppb threshold was 99.4% (326/328) in the whole dataset, 100% (149/149) in lesions with SECT < 100 HU, and 98.9% (177/179) in lesions with SECT \geq 100 HU. The sensitivity and specificity were 98.5% (133/135) and 100% (193/193) in the whole dataset, 100% (133/135) and 100% (14/14) for lesions under 100 HU, and specificity was 100% (179/179) in lesions greater than 100 HU. In this final category, sensitivity could not be calculated because there were no cases positive for hemorrhage.

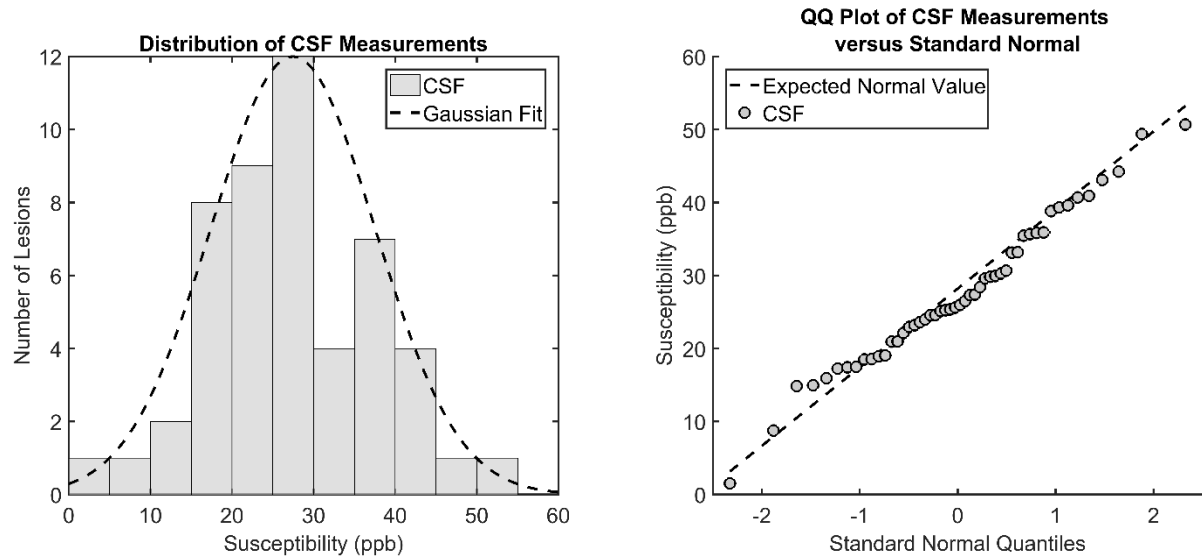


Figure 5.7: Histogram of the CSF susceptibility measurements for 50 patients with a Gaussian fit (left). A quantile-quantile plot is shown on the right to display the deviation of individual measurements from the displayed normal distribution (right). A Shapiro-Wilk test did not reject the null hypothesis that the distribution was Gaussian ($p = 0.71$).

Table 5.6: Mean SECT and QSM measurements for lesions classified as hemorrhage and calcification based on a threshold of 37.6 ppb.

	Hemorrhage (n = 135)		Calcification (n = 193)	
	<i>Mean</i>	<i>Standard Deviation</i>	<i>Mean</i>	<i>Standard Deviation</i>
<i>SECT (HU)</i>	36.8	18.5	177.7	86.4
<i>QSM (ppb)</i>	741.8	445.8	-117.6	97.9

a) Whole Dataset

		Reference Standard	
		Hemorrhage	Calcification
Predicted	Hemorrhage	133	2
	Calcification	0	193

SECT \geq 100 HU

		Reference Standard	
		Hemorrhage	Calcification
Predicted	Hemorrhage	0	2
	Calcification	0	177

SECT < 100 HU

		Reference Standard	
		Hemorrhage	Calcification
Predicted	Hemorrhage	133	0
	Calcification	0	16

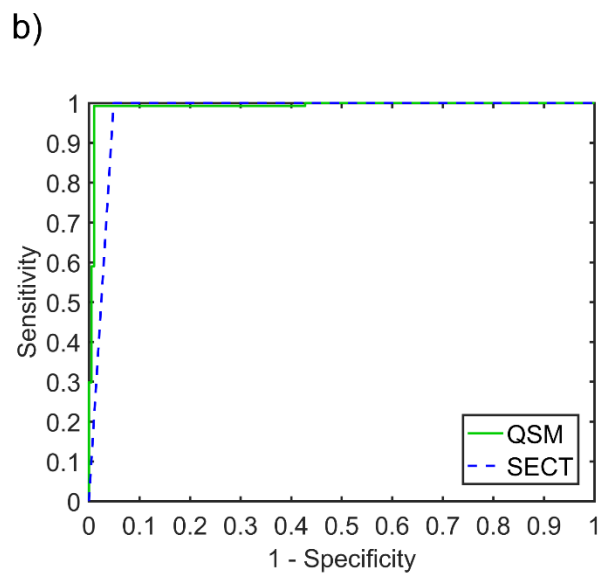


Figure 5.8: a) Classification matrices for the QSM-based logistic model compared to the reference standard and b) the ROC curve for the QSM and SECT classification schemes.

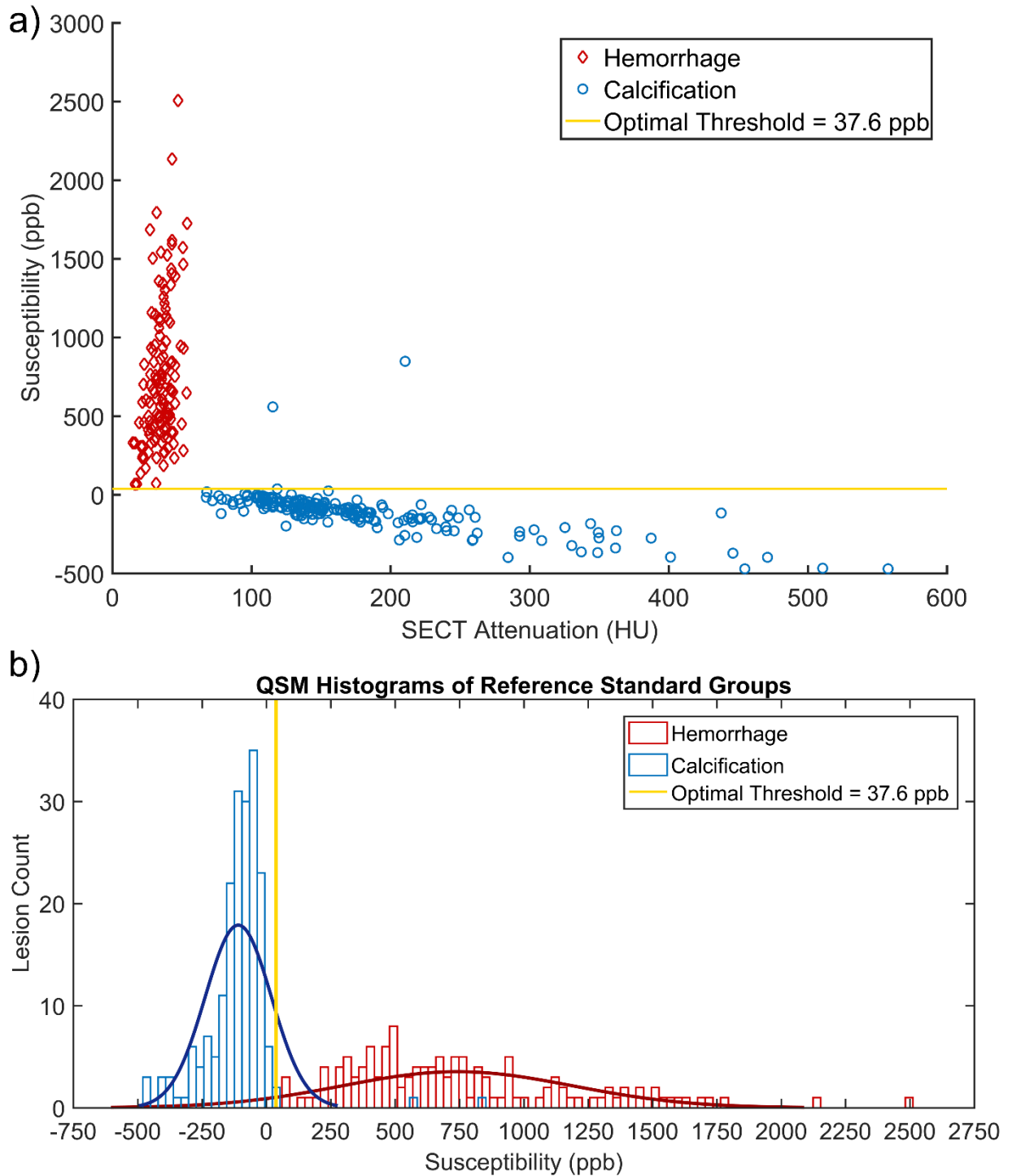


Figure 5.9: a) Mean QSM for each lesion versus the SECT attenuation in HU. Note that two lesions measure both over 100 HU and well above a susceptibility of 37.6 ppb. These two lesions are known as outliers where calcification is present adjacent to a vein or hemorrhagic lesion. b) Histograms of the QSM mean for calcifications and hemorrhages with kernel density estimates of the distributions. The optimal threshold of 37.6 ppb is shown in yellow in both plots.

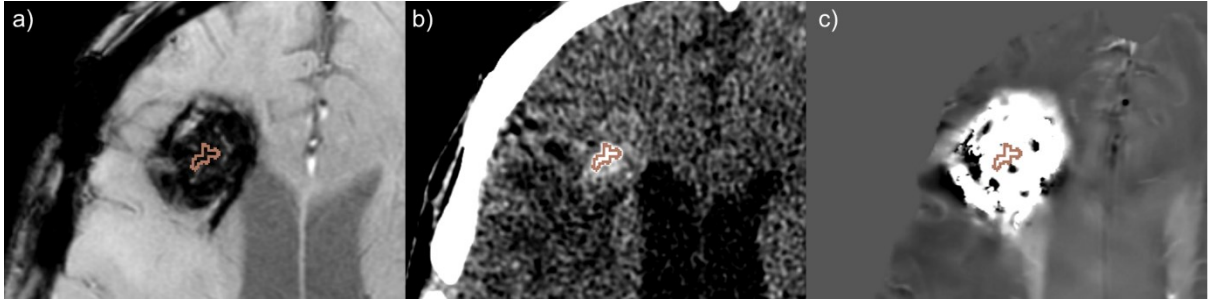


Figure 5.10: A 48-year old female patient with a history of right frontal craniotomy and a lobular mass consistent with cavernoma presenting as a large focus of susceptibility on the MFGRE (TE = 14.5 ms) (a). The SECT (b) demonstrates a densely calcified region within the lesion (red outline) with HU greater than 100. (c) QSM of the lesion shows high magnetic susceptibility throughout the lesion with regions of apparent aliased signal. The calcification does not present with the expected negative susceptibility.

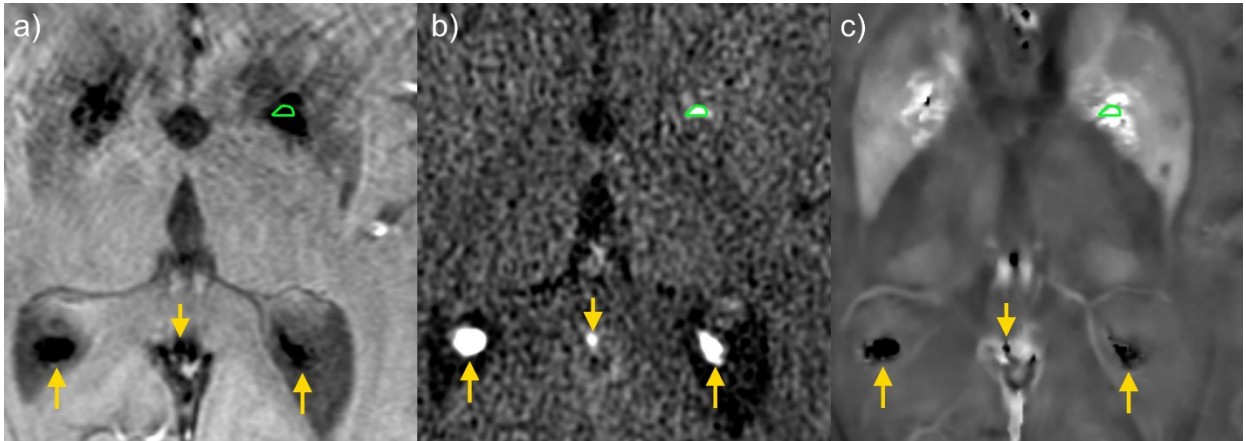


Figure 5.11: A 73-year old female patient with a history of metastatic melanoma with Gamma Knife therapy. (a) The globus pallidus shows mineralization consistent with aging that causes low signal on the MFGRE (TE = 14.5 ms). (b) SECT shows a small calcification (green outline) within the globus pallidus with attenuation over 100 HU. (c) QSM shows consistently high signal in the globus pallidus despite the presence of calcification, but other calcific lesions (yellow arrows) demonstrate the expected negative susceptibility.

5.3.5 Statistical Analysis

The 2 x 2 classification matrices comparing the DECT and QSM classifications for the whole dataset, lesions with SECT < 100 HU, and lesions with SECT ≥ 100 HU are found in Table 5.7 - Table 5.9. For each of these classifications respectively, McNemar's test returned $p = 1.000$, $p = 1.000$, and $p = 0.500$, indicating that QSM and DECT were concordant. κ was

equal to 0.981 and 0.964 for the whole dataset and those lesions under 100 HU; κ could not be computed for lesions over 100 HU because DECT did not indicate the presence of any hemorrhagic lesions. Therefore, concordance between the two modalities was very high, and we can assume that the lesions under 100 HU for which QSM and DECT are in agreement (133 hemorrhagic lesions, 15 calcific lesions) are accurately classified. Accuracy, sensitivity, specificity, positive predictive value (PPV), negative predictive value (NPV), and area under the ROC curve (AUC) are tabulated in Table 5.10.

Table 5.7: Classification matrix for the QSM classifications of all lesions versus the DECT classifications for all lesions

Whole Dataset		QSM	
		Hemorrhage	Calcification
DECT	Hemorrhage	133	1
	Calcification	2	192

Table 5.8: Classification matrix for the QSM classifications of all lesions versus the DECT classifications for lesions with SECT greater than 100 HU.

SECT > 100 HU		QSM	
		Hemorrhage	Calcification
DECT	Hemorrhage	0	0
	Calcification	2	177

Table 5.9: Classification matrix for the QSM classifications of all lesions versus the DECT classifications for lesions with SECT less than 100 HU.

SECT < 100 HU		QSM	
		Hemorrhage	Calcification
DECT	Hemorrhage	133	1
	Calcification	0	15

Table 5.10: Comparison of the ROC analysis for SECT (threshold = 100 HU), DECT, and QSM ROC analyses. Values were calculated for water(calcium) and calcium(water) images in the whole dataset. Dashes represent values that could not be calculated due to division by zero. The AUC for the SECT data was calculated assuming a threshold of 100 HU.

<i>Data Subset</i>	<i>Classification Method</i>	<i>Accuracy</i>	<i>Sensitivity</i>	<i>Specificity</i>	<i>PPV</i>	<i>NPV</i>	<i>AUC</i>
<i>Whole Dataset</i>	SECT (HU)	95.1	100	91.8	89.3	100	0.976
	Water(Calcium)	90.9	92.5	89.7	92.5	89.7	0.970
	Calcium(Water)	99.3	98.5	99.0	98.5	100	0.997
	DECT (Logistic Model)	99.7	99.3	100	100	99.5	0.998
	QSM (ppb)	99.4	100	98.5	100	99.0	0.991
<i>SECT < 100 HU</i>	SECT (HU)	89.3	100	0	89.3	-	
	DECT (Logistic Model)	99.3	99.3	100	100	93.8	
	QSM (ppb)	100	100	100	100	100	
<i>SECT ≥ 100 HU</i>	SECT (HU)	100	-	100	-	100	
	DECT (Logistic Model)	100	-	100	-	100	
	QSM (ppb)	98.9	-	98.9	0	100	

5.4 Discussion

This study evaluated both DECT and QSM for the identification of calcification and hemorrhage *in vivo*. Our initial clinical reference standard was based on a radiologist's interpretation of the lesion based on the available prior clinical MRI imaging (including T2*-weighted GRE and T1- and T2-weighted imaging) and the study exams. This standard was found to be highly concordant with the subsequent quantitative analyses. It is of paramount importance to the interpretation of the results presented here that the study was performed in an outpatient population with chronic lesions. Patients presenting with acute symptomatic lesions in an emergent setting frequently have hemorrhagic lesions of higher attenuation, and we would anticipate that we would see additional overlap in the SECT attenuation of the calcific and hemorrhagic lesions if these patients were included in the trial. As the overlap in attenuation would increase, we would expect that the results, particularly for the DECT analysis, would result in worse differentiation.

We confirmed the efficacy of QSM for the accurate differentiation of diamagnetic and paramagnetic materials (45, 205, 206). DECT calcium(water) and the DECT logistic regression both had higher accuracy compared to SECT with a 100 HU threshold for this lesion classification. As DECT becomes increasingly available clinically, it may provide additional avenues for the diagnosis of hemorrhage, particularly for patients in emergent settings or those with contraindications to MRI.

There are inherent difficulties in determining the reference standard for these lesions because there is no true gold standard under 100 HU on SECT. In cases where no true gold standard exists, it has been established within the statistical literature that agreement statistics between two diagnostic tests provides valuable diagnostic information (244, 245). Because we were differentiating between two diagnostic classes, calcification and hemorrhage, we utilized the methodology developed by McNemar (240). In a two by two contingency table, such as Table 5.7, the concordant results in which both tests agree are ignored in McNemar's test, and instead the null hypothesis is that the probability of discordant measurements that are positive by test 1 and negative on test 2 is equal to those that are positive on test 2 and negative on test 1 (240). Therefore, if the null hypothesis is rejected, the two tests provide different results. In this case, McNemar's test did not reach statistical significance when testing QSM against DECT for the differentiation of chronic hemorrhage and calcification, so we could assume that a lesion that had the same classification by both imaging modalities being tested was an accurate diagnosis.

With access to follow-up imaging for nearly all patients, we were able to establish a clinical reference standard using both CT and MRI. However, this was still based on a conventional understanding of the properties of calcification and hemorrhage on conventional imaging; we

have shown in this work that intracranial calcification can have SECT attenuation values under 100 HU (Figure 5.3). We also considered the results of the DECT and QSM to be accurate if the two modalities were concordant. Prior studies had only diagnosed calcification if the lesion was greater than 100 HU or they had pathologic proof (45, 205, 206). Chen et al. found Morphology-Enabled Dipole Inversion (MEDI) QSM, which was also utilized in this study, to have a sensitivity of 89.5% and specificity of 94.5% for detection of hemorrhage and calcification (45). Our study focused on a slightly different task, in which segmentation was performed on the MFGRE and SECT images. However, by utilizing foci of susceptibility that represented known physiologic calcifications, we were able to demonstrate very high sensitivity and specificity for QSM at 99.4% and 98.5%, respectively, within the whole dataset.

The work of Nute et al. was the first to utilize DECT imaging to differentiate between intracranial calcification and hemorrhage by utilizing several phantom studies (135, 136). We utilized the protocol recommended in said work and a calcium/water material decomposition (136). Despite this study being developed as a corollary of that phantom work, there were several key differences as we translated this work from phantoms into humans. First, we did not investigate the use of multiple image thickness values. It is likely that there would be significant image quality improvements in the DECT images if a thicker image were used, at the expense of losing spatial resolution and being unable to analyze smaller lesions. The second was that we found that the 68 keV data, which formed the z-axis in a 3D feature space, was highly correlated with the calcium(water) data from the patient lesions and could be eliminated from the differentiation algorithm (136). While the SECT attenuation of each lesion was still used as a reference point for reporting purposes, this simplifies the analysis in the long term, which could encourage clinical use.

In comparison to another DECT study differentiating calcific and hemorrhagic lesions, our study had a larger proportion of chronic hemorrhagic lesions since the clinical imaging was conducted on a purely outpatient basis, and was not performed in an emergency room or inpatient setting (137). Additionally, ROC analysis of SECT data showed that an optimal threshold could be found without using DECT to differentiate between chronic hemorrhage and calcification based on density alone. There was a total of 53 lesions that had a mean SECT HU between 40 and 100 HU, and we estimate that 16 of them were calcific based on concordance between the DECT and QSM. Of those 53 lesions within an HU range expected of acute or sub-acute hemorrhage (3, 26, 246), 31 did not have a SECT attenuation higher than 50 HU. The primary disadvantage of this is that chronic hemorrhagic lesions may not be readily visible relative to the brain parenchyma on DECT because they have similar attenuation levels as gray and white matter. Therefore, DECT may be of limited utility for patients that cannot undergo conventional T2*-weighted GRE MRI to identify regions where susceptibility is present. However, results of a previous phantom study from our groups demonstrated that fast-kVp switching CT was able to differentiate between calcific and hemorrhagic lesions of comparable SECT HU above 50 HU (136). The inclusion of acute hemorrhage in future trials will allow us to confirm the results of the phantom study.

Two patients had to be excluded from the study due to motion artifacts that corrupted the MFGRE data used for QSM processing. The pulse sequence used in this study was comprised of 12 echo times, which increased the scan time compared to the SWAN sequence that was utilized in our phantom studies (Chapter 4). The MFGRE sequence is also a three-dimensional pulse sequence, which is inherently more susceptible to motion artifacts throughout the entire scan field of view compared to two-dimensional sequences. For clinical implementation, it would be advantageous to limit the acquisition time in order to lower the chance of non-diagnostic images that could not undergo additional processing. There are many possible

avenues to consider in order to achieve this goal. The number echoes could be lowered to six or eight, and the spatial resolution could be reduced compared to this research sequence. Overall, this indicates that DECT, with acquisition times under 30 seconds, may be a valuable alternative for differentiating calcific and hemorrhagic lesions in patients that are unable to remain still for long periods of time due to their medical condition during an MR exam.

QSM remains time intensive at approximately one hour per iteration for an average of six iterations. This time could be lowered significantly by utilizing servers with higher processor speeds than those available for use in this study. Decreasing the spatial resolution of the MFGRE pulse sequence, particularly the number of images per slab, would also reduce the computation time required for the QSM. Except for two calcifications which were adjacent to known hemorrhage or venous structures, QSM proved to be highly sensitive in identifying both hemorrhage and calcification. The QSM processing in the MEDI algorithm includes the option for using a spherical mean value to help acquire the true susceptibility in brain parenchyma. This can minimize the appearance of subtle artifacts that may remain after MEDI processing by averaging data in a sphere surrounding a specific voxel but may cause additional volume averaging near anatomical edges. While lesion edges were generally avoided when placing ROIs in this study, it may have contributed to the errors seen near chronic hemorrhage with very high susceptibility (Figure 5.10, Figure 5.11). The lesions that were misclassified were both small calcifications surrounded by high positive susceptibility regions. Because the magnitude of the magnetic susceptibility in iron-based lesions (including mineralization in deep gray matter) is much higher than that of calcification, any averaging present may result in small calcific lesions being masked by adjacent iron deposition. Adjusting the spherical mean value diameter setting may be of interest to clinicians as this method gains wider acceptance in the clinic in order to optimize the post processing for a given application to balance the visualization of small calcifications and minimization of artifacts.

There were several other limitations in this study. The first is that screening was performed nearly entirely on T2*-weighted GRE MRI, which is highly sensitive to chronic hemorrhage. Because most patients entered into the study did not have a head CT available for comparison, there was no way to guarantee that lesions were a) visible on CT and b) within the desired 40 – 100 HU range. Because the lesions were not necessarily visualized on SECT or DECT, segmentation of the lesions of interest (outside known calcifications) was performed on the MFGRE. Some disadvantages of using the MFGRE for this purpose include lower spatial resolution than the SECT and the potential for blooming artifact. Blooming, in particular, would cause an ROI to be larger than the actual lesion and could degrade the DECT results by including normal brain tissue surrounding the lesion within the volume of interest. The second limitation is that the study was performed at an ambulatory clinical research center rather than in an emergent or inpatient setting. The study location further skewed the study towards cases of chronic hemorrhage because the majority of patients with acute hemorrhage were too ill to undergo the imaging required for the study. This ultimately meant that ROC analysis was able to find a SECT threshold that had slightly higher accuracy than the DECT in this dataset. We know from clinical experiences at other institutions that this would not be the case were acute hemorrhage more prevalent in the study (137).

Future work will include continued patient accrual through September 2018 or until 100 patients have been scanned. We plan on investigating whether DECT monoenergetic images may further assist in the differentiation of hemorrhage and calcification. Additionally, we have a multi-modality dataset that can also be used to determine the optimal monoenergetic energy for comparisons to SECT, investigate the extent of blooming artifact compared to the quantitative susceptibility of lesions, and further quantify the magnetic susceptibility of normal tissues within the brain. This extensive dataset may enable further comparisons in this dataset to DECT

material decompositions utilizing iron as in the material decomposition. In addition, this work justifies a future clinical trial which would investigate the differentiation of acute hemorrhage and calcifications in an emergent setting.

6.1 Summary of Findings

In this dissertation, we explored the application of DECT and Phase-Sensitive MRI (PS-MRI) techniques for the classification of intracranial calcific and hemorrhagic lesions. On conventional T2*-weighted MRI, both these lesion types are indicated by the presence of dark spots in the image that result from the presence of a material with a magnetic susceptibility different from the surrounding normal tissue. Calcium is diamagnetic while most iron-based compounds are paramagnetic, so utilizing the MRI phase in susceptibility-weighted pulse sequences is a promising technique for differentiating the two lesion types.

In Chapter 3, we validated phantom materials that modeled the signal properties of calcific and hemorrhagic lesions on a multi-echo GRE pulse sequence. T2*, the time it takes for a material's spins to dephase when field inhomogeneities are present, was a quantity that we could use to compare our phantom materials to the biological T2* values for calcification and hemorrhage in the literature. We investigated a total of seven materials (two calcium-based and five iron-based) for use in an MR phantom. Four materials were chosen for use in the final two phantoms based on their T2* values: hydroxyapatite, iron dextran, iron(III) chloride, and human lyophilized hemoglobin powder. Our lab developed hydroxyapatite agarose gels for use in a DECT phantom (135), but few studies were available in the literature which utilized calcium-based MRI phantoms (208, 215, 247). Because of this work, we determined that powdered hydroxyapatite embedded in agarose does adequately model the T2* decay properties of low-density intracranial calcifications. Similarly, we determined that three iron-based compounds—iron dextran, iron(III) chloride, and human hemoglobin—had T2* values comparable to that of

hemorrhagic lesions and iron-laden deep gray matter, with $T2^*$ between approximately 5 and 35 ms (209-211).

After demonstrating that we could model the appearance of hemorrhage and calcification on $T2^*$ -weighted GRE magnitude images in phantoms, we began to assess the feasibility of differentiating between the two iron- and calcium-based models with PS-MRI (Chapter 4). The phantoms developed in Chapter 3 provided a simple physics model for testing different PS-MRI methods. The first method tested in phantoms was the automatically-processed filtered phase image from the SWAN pulse sequence. We found that these phase images did not have sufficient phase unwrapping, and, as a result, the phase did not correlate well with increasing concentration of either diamagnetic or paramagnetic materials (Figure 4.3). The second method tested was Projection onto Dipole Fields (PDF), which results in a background subtracted phase image. These images were of higher quality than the SWAN phase images, and we could visually discriminate between calcification and hemorrhage. There was a high correlation between the phase and all materials except iron(III) chloride. Additionally, there was some shading around samples with high positive susceptibility that would be a confounder for clinical diagnosis of calcification and hemorrhage (Figure 4.5d). Finally, the PDF image was used as an input for Quantitative Susceptibility Mapping (QSM) in which the background subtracted phase (which provides a map of the local magnetic field) was used to solve an inverse problem that returns the distribution of magnetic susceptibility within the phantom. The QSM processing was able to eliminate some of the errors in the iron(III) chloride samples found in the PDF phase images. The improvement in the QSM of the iron(III) chloride over the PDF is likely due in part to the additional spherical mean value averaging that helps to arrive at the true susceptibility within a reasonably uniform region. Additionally, the shading surrounding several lesion models in the PDF images was resolved in the QSM. Overall, QSM had the highest correlation between material concentration and susceptibility, and the images are easily

interpretable—diamagnetic materials returned negative susceptibility while paramagnetic materials had a positive susceptibility.

Given the results of Chapter 4, we focused on the ability of SECT, DECT, and QSM to differentiate between calcific and hemorrhagic lesions in vivo (Chapter 5). The human trial accrued a total of 52 patients with 328 lesions. Of those lesions, 179 were classified as calcification definitively by SECT ($HU \geq 100$). Overall, a clinically-derived reference standard identified 195 likely calcifications (14 under 100 HU) and 133 hemorrhages. Both SECT and DECT were able to identify known calcifications with 100% accuracy. QSM classified two definitive calcifications incorrectly; one was located near a vein which masked the calcification, and the other was surrounded by likely hemorrhage. Below a SECT threshold of 100 HU, QSM was 100% accurate compared to a clinically-derived reference standard. While DECT (and SECT with an optimized differentiation threshold) narrowly remained the most accurate modality for identifying hemorrhage and calcification in this dataset, it must be qualified by the fact that our dataset did not include any hemorrhage with an attenuation between 53 HU and 100 HU on SECT, and no overlap in HU between the hemorrhagic and calcific lesions was present.

6.2 Advances in Knowledge

This work provided several advances in knowledge and utilized a unique study design which examined two imaging modalities to arrive at a consensus on the diagnosis of hemorrhage and calcification. The first advance was the creation of an MR phantom with calcific and hemorrhagic lesions available for direct comparison with phase-sensitive MRI post-processing algorithms. Overall, there are very few phantoms described in the MR literature that specifically included calcium as a material of interest (208, 215, 247). Valdés Hernández et al. did directly compare iron and calcium in a phantom using calcium carbonate and superparamagnetic iron oxide nanoparticles in alginate beads, which is a gel similar to agarose (215). They utilized the

phantom to differentiate between calcification and hemorrhage models using only T1-weighted and T2-weighted magnitude image features. However, their lesion models were approximately 1-3 mm in diameter, which would not have provided an adequate volume for quantitative measurements within the lesion models (215). More importantly, they were unable to control the exact concentration of their gels. Utilizing phase-based image processing such as QSM allows us to interrogate the imaging data for a quantity that directly correlates with the concentration of these material types as well as providing thresholds for the accurate differentiation of calcification and hemorrhage.

We also validated several materials that could potentially simulate hemorrhage on MRI. There are several quantities of interest that we would ideally like to match in order to simulate these lesions adequately in phantoms. The first, which we investigated extensively, was the T2* value associated with various concentrations of materials. This quantity defines the exponential decay of the signal in a multi-echo T2*-weighted GRE sequence as the echo time (TE) increases. This has been extensively reported in the literature for many tissue types (209-212). The second quantity of interest is the magnetic susceptibility, which should increase gradually with increasing iron content to mimic most iron-laden tissues. We validated that our materials, particularly iron dextran, behaved very similarly to human hemoglobin (primarily in the form of methemoglobin). While most studies utilize superparamagnetic iron oxide nanoparticles (SPIOs) in phantoms, they are very expensive relative to iron dextran (which can be acquired through most chemical suppliers), and the ratio of susceptibility to iron concentration is incredibly high, outside of the biologically-expected range, due to the superparamagnetic properties of the nanoparticles (see Section 2.4.3). Therefore, very small differences in SPIO concentration could cause a very large shift in the susceptibility, and errors in the physical measurement of the compound would have an unduly large impact on the phantom data.

The design of our patient study is also unique, and—to our knowledge—we are the first group to attempt an investigation of intracranial lesions specifically under 100 HU. While DECT and QSM have been used to differentiate between calcification and hemorrhage *in vivo* in individual retrospective studies (137, 205, 206), there have been no studies attempting to compare the two modalities directly and prospectively. Because we acquired non-contrast SECT in the same session as non-contrast DECT and phase-sensitive MRI, we could compare the conventional methods of identifying calcification to that of more recent image processing methodologies. We included naturally occurring calcifications in our analysis. This allowed us to analyze calcific lesions within nearly every patient, and the degree of calcification in these normal tissues (i.e., the pineal gland and choroid plexus) returned highly varied attenuation levels, definitively demonstrating the presence of calcification under the 100 HU SECT threshold currently used clinically.

Along with other studies in the literature, we have been able to help establish the range of susceptibility values expected within chronic hemorrhagic lesions. This is important moving forward so that pulse sequences that will be used for QSM processing can be optimized to work for a wide variety of patients. While we did not optimize our pulse sequence for visualization of the vasculature, we were able to easily visualize and identify hemorrhagic metastases as well as calcific lesions under 100 HU on SECT.

6.3 Limitations

There are several major limitations to the methodologies employed in this study. The first is that the samples in the phantom were cylindrical, and therefore resulted in orientation dependence on the susceptibility-weighted MRI sequences. It would be advantageous to develop spherical molds of various sizes to eliminate this orientation dependence; it would also allow for the vials themselves to be eliminated from the phantom design. While the vials did not cause artifacts

within the QSM images, removing them would minimize the number of abrupt boundaries in the susceptibility map and may better represent the shape of most lesions within the brain.

One of the main limitations to potential clinical translation discovered during this work is the time required for QSM processing of large datasets. A patient dataset took approximately six hours to reconstruct. However, this reconstruction was performed on a server with eight 2.8 GHz Dual-Core Opteron 8220 (Advanced Micro Devices, Santa Clara, CA) processors, which were released in 2007. Given modern processing speeds, reconstruction times should be approximately 1 hour, provided sufficient RAM is available on the system. While this process was performed offline for this study, the MEDI algorithm has been licensed to MR manufacturers and may become commercially available in the near future.

Finally, the patient population enrolled in the clinical trial was heavily weighted towards patients with chronic hemorrhage, as discussed extensively in Section 5.4. While this represents the majority of the outpatients with hemorrhagic lesions at our oncology-focused institution, it is not representative of what may be seen in an emergent or inpatient setting, particularly at hospitals that are more likely to treat hemorrhagic stroke or traumatic brain injury. Including patients with acute hemorrhage in the study would allow us to study the true differentiation of hemorrhage and calcification with SECT attenuation levels between 60 and 100 HU in a more representative patient population. However, it would be difficult to acquire all of the imaging for this study in one imaging session. Given the potential for temporal evolution of acute hemorrhage and/or surgical intervention, the temporal matching of the CT and MRI exams would be of even greater importance and be much more difficult to achieve without compromising care for these patients.

6.4 Future Work

There are multiple avenues for research to be pursued using this dataset—both phantom and human—as an extension of this work. The phantom data provides a reference for many different iron-based materials that are similar to materials found within the body. By utilizing phantoms akin to those created throughout the course of this work, we can further investigate image quality concerns that may arise during QSM processing, such as phase aliasing. By replicating these image quality issues in phantoms, we can test additional algorithms to detect and correct for potential errors. The phantoms may also be used as a reference to begin iron quantification studies using QSM and DECT. We can use the phantom data that has already been acquired, along with the patient data, to assess the accuracy of QSM when performed with fewer echoes or other pulse sequences, such as the ultrashort echo time sequence acquired alongside the other susceptibility-weighted sequences (248).

Within the patient dataset, one research area in which our dataset is particularly suited is in comparing image quality and quantitative metrics between SECT and DECT in both normal tissue and lesions. There are no existing guidelines for translating diagnostic thresholds from years of experience with SECT to the new paradigm of DECT. While some vendors provide a mixed image which may be a reasonably close match to a conventional 120 kVp SECT, other vendors may recommend using monoenergetic images as a replacement for SECT. Therefore, it is paramount that we are able to either find monoenergetic energies for which various tissue compartments have mean CT numbers equal to the 120 kVp SECT Hounsfield Unit, or that we find an algorithm that can convert a SECT threshold to its monoenergetic equivalent.

We acquired several pulse sequences as a part of the clinical trial that were not explicitly described in this dissertation. Several may be utilized in other studies for differentiation of calcification and hemorrhage. We acquired an Ultrashort Echo Time (UTE) sequence which

can provide signal even within the bony anatomy, and may assist in the identification of dense calcification which has a very low proton density and, consequently, a low signal on conventional MRI sequences. We also have acquired a synthetic MR sequence which can be processed into T1-weighted, T2-weighted, and Proton Density-weighted image series as well as quantitative maps of T1 and T2. We plan on investigating how results from these two sequences correlate with the data acquired with QSM.

Ultimately, we would like to see both DECT and QSM adopted for appropriate brain imaging in the clinic. We have extensively studied quantitative differentiation of calcific and hemorrhagic lesions on a fast kVp switching DECT system, but to adapt this protocol to other systems, it would be useful to repeat some of the imaging performed by Nute et al. to optimize the workflow (136). Using images from our current study, we could also perform a reader study to determine if chronic hemorrhagic lesions can be visualized on DECT without registration to an MR image. Following these steps, implementing DECT for routine brain scans either in the inpatient or outpatient settings would require that we reduce the CTDI_{vol} (currently 132.6 mGy). To counteract the increase in noise caused by lowering the dose, we would also increase the image thickness to 3.75 mm in an attempt to maintain reasonable signal-to-noise ratios. Finally, we would need to develop the workflow so that all required DECT images (calcium, water, SECT equivalent) would be reconstructed automatically and sent to PACS for radiologists' viewing.

Implementing QSM in a clinical environment may be more technologically challenging than introducing DECT. First, the MFGRE sequence we used had an acquisition time near 7 minutes in patients. This would need to be shortened for clinical acceptance, and so we would likely need to decrease the number of echoes acquired and potentially adjust the spatial resolution. Trained staff would be required to initiate QSM processing, which requires

significant computational power to complete in a reasonable amount of time. This may become easier as several vendors, including General Electric, have licensed the MEDI QSM software for implementation on their workstations. However, lesions close to the bone-tissue boundary may be left out of the automated selection of brain tissue, and the images would need to undergo careful quality assurance before being available for radiologists to read.

In summary, our major findings were that DECT and QSM improved on the current clinical SECT threshold of 100 HU for differentiating between hemorrhagic and calcific lesions in a prospective clinical trial. In the future, we would like to pursue an additional clinical trial of patients with acute hemorrhage in an emergent setting.

Contraindications to MR Imaging

Subjects and employees must report the presence of the following devices or conditions because they may be contraindications to MR, as reported in Appendix II of the American College of Radiology Guidance Document on MR Safe Practices (249):

- Heart pacemaker or defibrillator
- Neuro- or bio-stimulator
- Cochlear implants
- Cerebral aneurysm clips
- Intravascular coils/filter/stents
- Any metal in the eyes
- Any ocular implant
- Artificial heart valve
- Surgical clips or staples
- Implanted drug pump
- Joint replacements
- Limb prosthesis
- Body piercing
- Hearing aids
- Internal electrodes/wires
- Implants held by magnets
- Bullet fragments/shrapnel
- Existing catheters/ports
- Eyelid spring
- Tissue expander
- Penile implant
- Intrauterine contraceptive device
- Rods/screws/plates
- Any other implanted device
- Medication patch
- Tattoos
- Halo vest
- Spinal fixation device or spinal fusion procedure
- Surgical mesh
- Brachytherapy radioactive seeds

Additionally, all metallic objects must be removed from the subject's person before their entering the MRI suite. Items specifically indicated by the American College of Radiology (249) include, but are not limited to:

- Hearing aids
- Pagers
- Cell phones
- Keys
- Hair pins/Barrettes
- Watches
- Safety pins
- Paper clips
- Metallic money clips
- Credit cards or any card with a magnetic strip
- Coins
- Pens
- Pocket knives
- Nail clippers
- Steel-toed shoes
- Tools
- Dentures or false teeth
- Eyeglasses
- Clothing with metal fasteners or zippers
- Jewelry, including body piercings
- Any other loose, metallic items

Clinical Trial Screening Procedure and Software



Figure 8.1: Clinical trial screening software example.

The screening software, developed using a combination of Python, Javascript, and Standard Query Language (SQL), was a web-based application that pulled all T2*-weighted GRE MRI of the head from the Picture Archiving and Communication System (PACS). The daily screening was performed in which study personnel cycled through all of the series for a given day to identify foci of susceptibility with at least one axis longer than 1.0 cm, such as the two lesions shown in the patient image in Figure 8.1. The numeric references in the figure above represent the following:

1. Patient Image

Patient datasets are displayed in Area 1 (Figure 1). The white box in the upper left-hand corner of the image represents an area of 1cm x 1cm for reference. Users may scroll

through images by hovering the mouse over this image and using the up/down arrow keys or the scroll wheel on the mouse.

2. *Patient Information*

Relevant patient information is displayed in Area 2 (Figure 1). These include the MRN, Patient Name, Dataset number (out of total acquired that day), Series Description, and Image Number within the series.

3. *Image Selection and Commenting*

Images of interest may be “marked” for later review by clicking the “Mark Image” button in Area 3 (Figure 1). A comment may be entered before imaging marking by entering text into the empty box left of the “Mark Image” button. Patients may be selected as potential study recruits by clicking “Recruit Patient.”

4. *Cycle Button and Cycle Speed*

Users may cycle through the patient series by clicking “Cycle” (Area 4, Figure 1). Cycle speed may be adjusted in the box to the left. Alternatively, users may hover the mouse over the patient image and press “CTRL” on the keyboard to start and stop cycling.

5. *Marked Image Table*

Marked images appear along with patient information in Area 5 (Figure 2) along with any user comments and the MDA Username of the user that marked the image.

6. *Potential Recruit Table*

Patients that are eligible to be recruited to the study will be collected in Area 6 (Figure 2).

7. *Patient Image Buttons*

Clicking on these images (Area 7, Figure 2), will automatically open the image in the main image viewer.

8. *Open Study Button*

Opens a dialog box that allows the user to open a specific patient image series (Area 8, Figure 2).

9. Copy MRN Button

Automatically copies the patient MRN for entry into Epic or iSite. A dialog box will appear to confirm that the data was copied successfully.

10. Date Selection

Clicking on the date (Area 10, Figure 2) brings up a calendar that allows the user to look at prior screening days. Click submit to go to images from that date.

11. Table Controls

The buttons located in Area 11 (Figure 2) control various table functions. "Refresh" reloads the tables. "Open Table In New Window" opens both tables in a full screen view with the recruiting table at the top. "Prelim Screening Complete" sends an e-mail to Dr. Schellingerhout noting that screening has been completed and is ready for review.

"Send All Recruiting Emails" sends an e-mail to study staff, including the research nurses, containing the recruiting table and links to individual patient data pages.

Lesions were marked when they were greater than 1.0 cm in length unless they represented one of the following known imaging artifacts or lesion types:

1. Sinuses

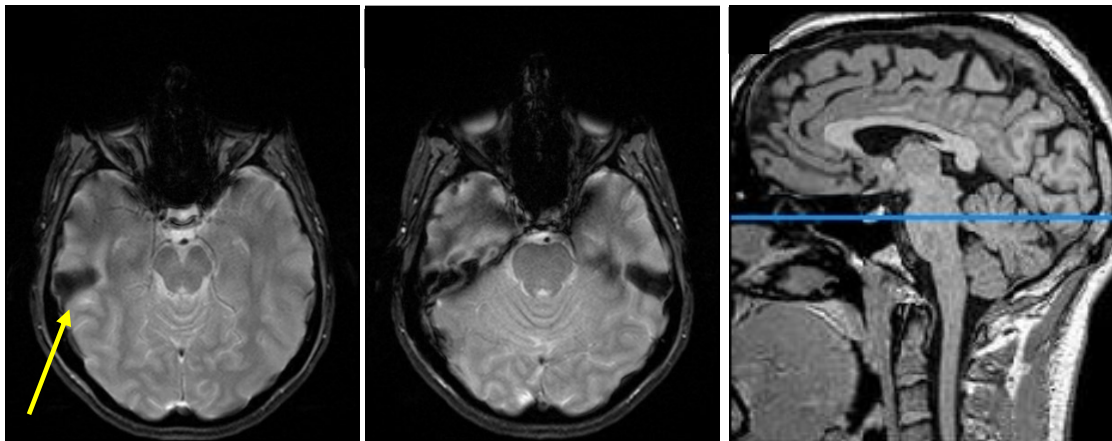


Figure 8.2: Dark lesion appearing in the right hemisphere (left, arrow). The next image in the series (middle) shows that both sides are symmetric. An example of the sagittal anatomy on T1-weighted imaging (<https://www.imaaios.com/en/e-Anatomy/Head-and-Neck/Brain-MRI-3D>) with the level of the "lesions" shown

2. Dura Mater Calcifications

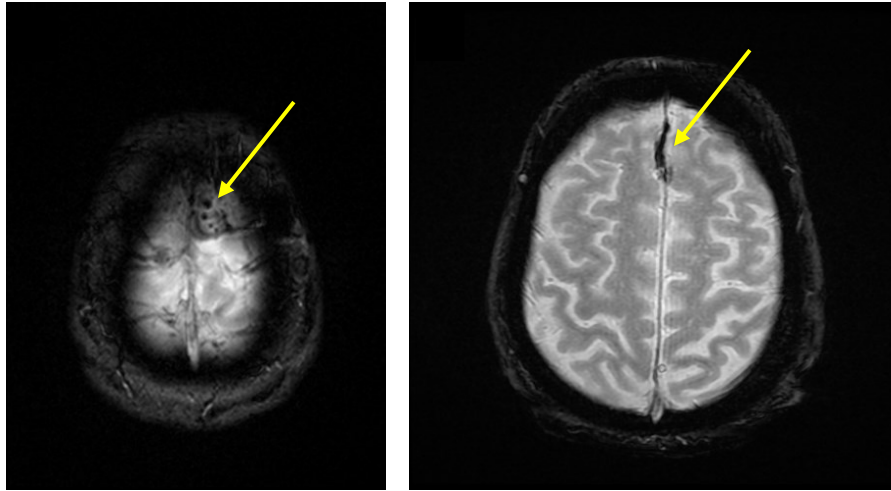


Figure 8.3: A calcification in the dura mater inside the skull (A) and separating the cerebral hemispheres (falx cerebri, B). These known calcifications can appear as dark lines along part or all of the falx cerebri.

3. Basal Ganglia Mineralization

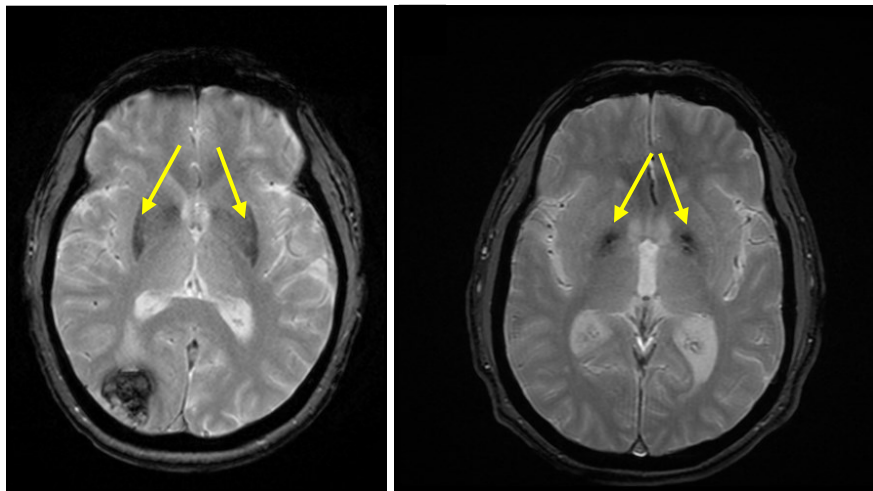


Figure 8.4: Iron deposition in the putamen (left, arrows) and globus pallidus (right, arrows) in the basal ganglia.

4. Pineal Gland Calcification

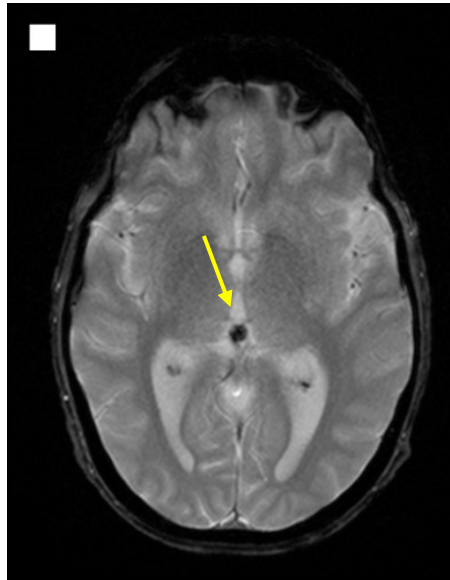


Figure 8.5: Pineal gland calcification located centrally in the image.

5. Choroid Plexus Calcifications

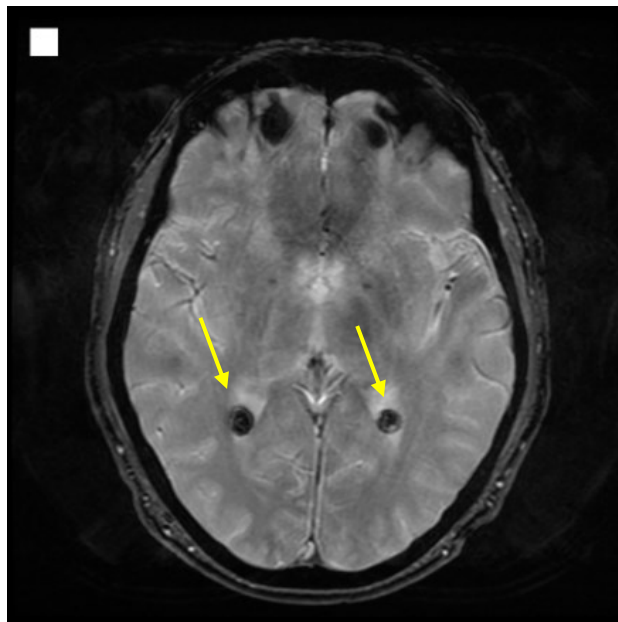


Figure 8.6: Choroid Plexus (arrows) mineralization. Usually found on the same slice or near the z-location of the pineal gland.

6. *Dentate Nuclei*

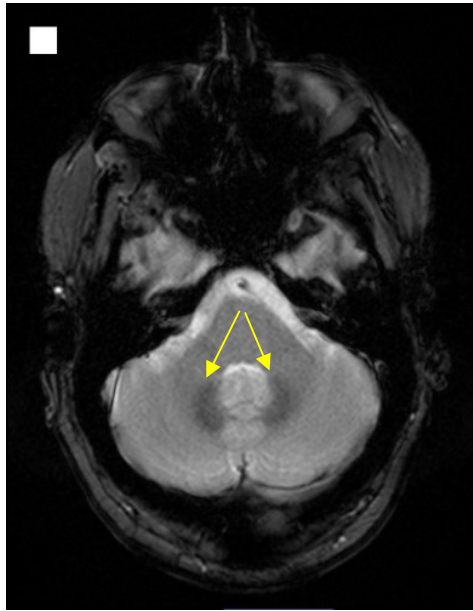


Figure 8.7: Iron deposition found in the Dentate Nuclei (arrows) in the cerebellum. This can appear darker, similar to the basal ganglia examples.

1. Go, J. L., and C. S. Zee. 1998. Unique CT imaging advantages. Hemorrhage and calcification. *Neuroimaging Clin N Am* 8: 541-558.
2. Bockenheimer, S. 2002. Diagnostic and interventional neuroradiology : a multimodality approach. K. Sartor, ed. Thieme, Stuttgart; New York. 160-169.
3. Parizel, P. M., S. Makkat, E. Van Miert, J. W. Van Goethem, L. van den Hauwe, and A. M. De Schepper. 2001. Intracranial hemorrhage: principles of CT and MRI interpretation. *Eur Radiol* 11: 1770-1783.
4. Haller, S., M. W. Vernooij, J. P. A. Kuijter, E. M. Larsson, H. R. Jager, and F. Barkhof. 2018. Cerebral Microbleeds: Imaging and Clinical Significance. *Radiology* 287: 11-28.
5. Rordorf, G., and C. McDonald. 2013. Spontaneous Intracerebral Hemorrhage: Pathogenesis, clinical features, and diagnosis. UpToDate, Waltham, MA.
6. Singer, R. J., C. S. Ogilvy, and G. Rordorf. 2012. Vascular malformations of the central nervous system. UpToDate, Waltham, MA.
7. Weber, F., and H. Knopf. 2006. Incidental findings in magnetic resonance imaging of the brains of healthy young men. *J Neurol Sci* 240: 81-84.
8. Simard, J. M., F. Garcia-Bengochea, W. E. Ballinger, Jr., J. P. Mickle, and R. G. Quisling. 1986. Cavernous angioma: a review of 126 collected and 12 new clinical cases. *Neurosurgery* 18: 162-172.
9. Zabramski, J. M., T. M. Wascher, R. F. Spetzler, B. Johnson, J. Golfinos, B. P. Drayer, B. Brown, D. Rigamonti, and G. Brown. 1994. The natural history of familial cavernous malformations: results of an ongoing study. *J Neurosurg* 80: 422-432.
10. Kondziolka, D., L. D. Lunsford, and J. R. Kestle. 1995. The natural history of cerebral cavernous malformations. *J Neurosurg* 83: 820-824.

11. Labauge, P., L. Brunereau, S. Laberge, and J. P. Houtteville. 2001. Prospective follow-up of 33 asymptomatic patients with familial cerebral cavernous malformations. *Neurology* 57: 1825-1828.
12. Batra, S., D. Lin, P. F. Recinos, J. Zhang, and D. Rigamonti. 2009. Cavernous malformations: natural history, diagnosis and treatment. *Nat Rev Neurol* 5: 659-670.
13. Moriarity, J. L., M. Wetzel, R. E. Clatterbuck, S. Javedan, J. M. Sheppard, K. Hoenig-Rigamonti, N. E. Crone, S. N. Breiter, R. R. Lee, and D. Rigamonti. 1999. The natural history of cavernous malformations: a prospective study of 68 patients. *Neurosurgery* 44: 1166-1171; discussion 1172-1163.
14. Nimjee, S. M., C. J. Powers, and K. R. Bulsara. 2006. Review of the literature on de novo formation of cavernous malformations of the central nervous system after radiation therapy. *Neurosurg Focus* 21: e4.
15. Jain, R., P. L. Robertson, D. Gandhi, S. K. Gujar, K. M. Muraszko, and S. Gebarski. 2005. Radiation-induced cavernomas of the brain. *AJNR Am J Neuroradiol* 26: 1158-1162.
16. Cutsforth-Gregory, J. K., G. Lanzino, M. J. Link, R. D. Brown, Jr., and K. D. Flemming. 2015. Characterization of radiation-induced cavernous malformations and comparison with a nonradiation cavernous malformation cohort. *J Neurosurg* 122: 1214-1222.
17. Gastelum, E., K. Sear, N. Hills, E. Roddy, D. Randazzo, N. Chettout, C. Hess, J. Cotter, D. A. Haas-Kogan, H. Fullerton, and S. Mueller. 2015. Rates and characteristics of radiographically detected intracerebral cavernous malformations after cranial radiation therapy in pediatric cancer patients. *J Child Neurol* 30: 842-849.
18. Burn, S., R. Gunny, K. Phipps, M. Gaze, and R. Hayward. 2007. Incidence of cavernoma development in children after radiotherapy for brain tumors. *J Neurosurg* 106: 379-383.

19. Strenger, V., P. Sovinz, H. Lackner, H. J. Dornbusch, H. Lingitz, H. G. Eder, A. Moser, and C. Urban. 2008. Intracerebral cavernous hemangioma after cranial irradiation in childhood. Incidence and risk factors. *Strahlenther Onkol* 184: 276-280.
20. Lew, S. M., J. N. Morgan, E. Psaty, D. R. Lefton, J. C. Allen, and R. Abbott. 2006. Cumulative incidence of radiation-induced cavernomas in long-term survivors of medulloblastoma. *J Neurosurg* 104: 103-107.
21. Di Giannatale, A., G. Morana, A. Rossi, A. Cama, L. Bertoluzzo, S. Barra, P. Nozza, C. Milanaccio, A. Consales, and M. L. Garre. 2014. Natural history of cavernous malformations in children with brain tumors treated with radiotherapy and chemotherapy. *J Neurooncol* 117: 311-320.
22. Vinchon, M., P. Leblond, S. Caron, I. Delestret, M. Baroncini, and B. Coche. 2011. Radiation-induced tumors in children irradiated for brain tumor: a longitudinal study. *Childs Nerv Syst* 27: 445-453.
23. Flemming, K. D., M. J. Link, T. J. Christianson, and R. D. Brown, Jr. 2012. Prospective hemorrhage risk of intracerebral cavernous malformations. *Neurology* 78: 632-636.
24. Washington, C. W., K. E. McCoy, and G. J. Zipfel. 2010. Update on the natural history of cavernous malformations and factors predicting aggressive clinical presentation. *Neurosurg Focus* 29: E7.
25. Salman, R. A.-S., J. M. Hall, M. A. Horne, F. Moultrie, C. B. Josephson, J. J. Bhattacharya, C. E. Counsell, G. D. Murray, V. Papanastassiou, V. Ritchie, R. C. Roberts, R. J. Sellar, and C. P. Warlow. 2012. Untreated clinical course of cerebral cavernous malformations: a prospective, population-based cohort study. *The Lancet Neurology* 11: 217-224.
26. Kidwell, C. S., and M. Wintermark. 2008. Imaging of intracranial haemorrhage. *Lancet Neurol* 7: 256-267.

27. Zimmerman, R. A., and L. T. Bilaniuk. 1982. Age-related incidence of pineal calcification detected by computed tomography. *Radiology* 142: 659-662.
28. Modic, M. T., M. A. Weinstein, A. D. Rothner, G. Erenberg, P. M. Duchesneau, and B. Kaufman. 1980. Calcification of the choroid plexus visualized by computed tomography. *Radiology* 135: 369-372.
29. Whitehead, M. T., C. Oh, A. Raju, and A. F. Choudhri. 2015. Physiologic pineal region, choroid plexus, and dural calcifications in the first decade of life. *AJNR Am J Neuroradiol* 36: 575-580.
30. Makariou, E., and A. D. Patsalides. 2009. Intracranial calcifications. *Applied Radiology* 38: 48-48.
31. Vonofakos, D., H. Marcu, and H. Hacker. 1979. Oligodendrogliomas: CT patterns with emphasis on features indicating malignancy. *J Comput Assist Tomogr* 3: 783-788.
32. Reiche, W., I. Grunwald, K. Hermann, M. Deinzer, and W. Reith. 2002. Oligodendrogliomas. *Acta Radiol* 43: 474-482.
33. Swartz, J. D., E. N. Faerber, N. Singh, and M. S. Polinsky. 1983. CT demonstration of cerebral subcortical calcifications. *J Comput Assist Tomogr* 7: 476-478.
34. Karimi, M., F. Habibzadeh, and V. De Sanctis. 2003. Hypoparathyroidism with Extensive Intracerebral Calcification in Patients with β -Thalassemia Major. *Journal of Pediatric Endocrinology and Metabolism* 16: 883-886.
35. Fujita, T. 2004. [Mechanism of intracerebral calcification in hypoparathyroidism]. *Clin Calcium* 14: 55-57.
36. Gardeur, D., A. Palmieri, and R. Mashaly. 1983. Cranial computed tomography in the phakomatoses. *Neuroradiology* 25: 293-304.
37. Wu, J., B. Tarabishy, J. Hu, Y. Miao, Z. Cai, Y. Xuan, M. Behen, M. Li, Y. Ye, R. Shoskey, E. M. Haacke, and C. Juhasz. 2011. Cortical calcification in Sturge-Weber

- Syndrome on MRI-SWI: relation to brain perfusion status and seizure severity. *J Magn Reson Imaging* 34: 791-798.
38. Zaki, S. A., and V. Lad. 2011. Sturge-Weber syndrome with bilateral facial nevus and early cerebral calcification. *J Pediatr Neurosci* 6: 114-115.
 39. Kauffman, W. M., C. J. Sivit, C. R. Fitz, T. A. Rakusan, K. Herzog, and R. S. Chandra. 1992. CT and MR evaluation of intracranial involvement in pediatric HIV infection: a clinical-imaging correlation. *AJNR Am J Neuroradiol* 13: 949-957.
 40. Jenkins, J. R. 1991. Computed tomography of intracranial tuberculosis. *Neuroradiology* 33: 126-135.
 41. Wasay, M., B. A. Kheleani, M. K. Moolani, J. Zaheer, M. Pui, S. Hasan, S. Muzaffar, R. Bakshi, and A. R. Sarawari. 2003. Brain CT and MRI findings in 100 consecutive patients with intracranial tuberculoma. *Journal of neuroimaging : official journal of the American Society of Neuroimaging* 13: 240-247.
 42. Del Brutto, O. H., G. Arroyo, V. J. Del Brutto, M. Zambrano, and H. H. Garcia. 2017. On the relationship between calcified neurocysticercosis and epilepsy in an endemic village: A large-scale, computed tomography-based population study in rural Ecuador. *Epilepsia* 58: 1955-1961.
 43. Koeller, K. K., and E. J. Rushing. 2005. From the archives of the AFIP: Oligodendroglioma and its variants: radiologic-pathologic correlation. *Radiographics* 25: 1669-1688.
 44. Fernandez-Bouzas, A., H. Ramirez Jimenez, J. Vazquez Zamudio, M. Alonso-Vanegas, and R. Mendizabal Guerra. 1992. Brain calcifications and dementia in children treated with radiotherapy and intrathecal methotrexate. *J Neurosurg Sci* 36: 211-214.
 45. Chen, W., W. Zhu, I. Kovanlikaya, A. Kovanlikaya, T. Liu, S. Wang, C. Salustri, and Y. Wang. 2014. Intracranial calcifications and hemorrhages: characterization with quantitative susceptibility mapping. *Radiology* 270: 496-505.

46. Tsuchiya, K., K. Makita, S. Furui, and K. Nitta. 1993. MRI appearances of calcified regions within intracranial tumours. *Neuroradiology* 35: 341-344.
47. Gamsu, G., G. de Geer, C. Cann, N. Muller, and A. Brito. 1987. A preliminary study of MRI quantification of simulated calcified pulmonary nodules. *Invest Radiol* 22: 853-858.
48. Cohen, A. T., V. F. Tapson, J. F. Bergmann, S. Z. Goldhaber, A. K. Kakkar, B. Deslandes, W. Huang, M. Zayaruzny, L. Emery, F. A. Anderson, Jr., and E. Investigators. 2008. Venous thromboembolism risk and prophylaxis in the acute hospital care setting (ENDORSE study): a multinational cross-sectional study. *Lancet* 371: 387-394.
49. Cohen, A. T., A. Katholing, S. Rietbrock, L. Bamber, and C. Martinez. 2017. Epidemiology of first and recurrent venous thromboembolism in patients with active cancer. A population-based cohort study. *Thrombosis and haemostasis* 117: 57-65.
50. van Es, N., M. Di Nisio, G. Cesarman, A. Kleinjan, H. M. Otten, I. Mahe, I. T. Wilts, D. C. Twint, E. Porreca, O. Arrieta, A. Stepanian, K. Smit, M. De Tursi, S. M. Bleker, P. M. Bossuyt, R. Nieuwland, P. W. Kamphuisen, and H. R. Buller. 2017. Comparison of risk prediction scores for venous thromboembolism in cancer patients: a prospective cohort study. *Haematologica* 102: 1494-1501.
51. Khorana Alok, A., W. Francis Charles, E. Culakova, M. Kuderer Nicole, and H. Lyman Gary. 2007. Frequency, risk factors, and trends for venous thromboembolism among hospitalized cancer patients. *Cancer* 110: 2339-2346.
52. Ay, C., D. Dunkler, C. Marosi, A.-L. Chiriac, R. Vormittag, R. Simanek, P. Quehenberger, C. Zielinski, and I. Pabinger. 2010. Prediction of venous thromboembolism in cancer patients. *Blood* 116: 5377.
53. Altschuler, E., H. Moosa, R. G. Selker, and F. T. Vertosick, Jr. 1990. The risk and efficacy of anticoagulant therapy in the treatment of thromboembolic complications in patients with primary malignant brain tumors. *Neurosurgery* 27: 74-77.

54. Strowd, R. E., 3rd, M. A. Knovich, and G. J. Lesser. 2012. The therapeutic management of bleeding and thrombotic disorders complicating CNS malignancies. *Curr Treat Options Oncol* 13: 451-464.
55. Magnus, N., E. D'Asti, D. Garnier, B. Meehan, and J. Rak. 2013. Brain neoplasms and coagulation. *Semin Thromb Hemost* 39: 881-895.
56. Flemming, K. D., M. J. Link, T. J. Christianson, and R. D. Brown Jr. 2013. Use of antithrombotic agents in patients with intracerebral cavernous malformations. *J Neurosurg* 118: 43-46.
57. Schneble, H. M., A. Soumare, D. Herve, D. Bresson, J. P. Guichard, F. Riant, E. Tournier-Lasserre, C. Tzourio, H. Chabriat, and C. Stapf. 2012. Antithrombotic therapy and bleeding risk in a prospective cohort study of patients with cerebral cavernous malformations. *Stroke* 43: 3196-3199.
58. Gattringer, T., A. Pichler, N. Homayoon, K. Niederkorn, C. Enzinger, and F. Fazekas. 2013. Symptomatic bleeding from an intracerebral cavernoma after intravenous thrombolysis for ischemic stroke. *J Neurol* 260: 1417-1419.
59. Pozzati, E., M. Zucchelli, A. F. Marliani, and L. A. Riccioli. 2006. Bleeding of a familial cerebral cavernous malformation after prophylactic anticoagulation therapy. Case report. *Neurosurg Focus* 21: e15.
60. Flemming, K. D., M. J. Link, T. J. Christianson, and R. D. Brown, Jr. 2013. Use of antithrombotic agents in patients with intracerebral cavernous malformations. *Journal of neurosurgery* 118: 43-46.
61. Erdur, H., J. F. Scheitz, S. Tutuncu, J. B. Fiebach, M. Endres, D. J. Werring, and C. H. Nolte. 2014. Safety of thrombolysis in patients with acute ischemic stroke and cerebral cavernous malformations. *Stroke* 45: 1846-1848.

62. Kalender, W. A., W. H. Perman, J. R. Vetter, and E. Klotz. 1986. Evaluation of a prototype dual-energy computed tomographic apparatus. I. Phantom studies. *Med Phys* 13: 334-339.
63. Vetter, J. R., W. H. Perman, W. A. Kalender, R. B. Mazess, and J. E. Holden. 1986. Evaluation of a prototype dual-energy computed tomographic apparatus. II. Determination of vertebral bone mineral content. *Med Phys* 13: 340-343.
64. Avrin, D. E., A. Macovski, and L. E. Zatz. 1978. Clinical application of Compton and photo-electric reconstruction in computed tomography: preliminary results. *Invest Radiol* 13: 217-222.
65. Chiro, G. D., R. A. Brooks, R. M. Kessler, G. S. Johnston, A. E. Jones, J. R. Herdt, and W. T. Sheridan. 1979. Tissue signatures with dual-energy computed tomography. *Radiology* 131: 521-523.
66. Millner, M. R., W. D. McDavid, R. G. Waggener, M. J. Dennis, W. H. Payne, and V. J. Sank. 1979. Extraction of information from CT scans at different energies. *Med Phys* 6: 70-71.
67. Alvarez, R. E., and A. Macovski. 1976. Energy-selective reconstructions in X-ray computerized tomography. *Phys Med Biol* 21: 733-744.
68. Johnson, T. R., B. Krauss, M. Sedlmair, M. Grasruck, H. Bruder, D. Morhard, C. Fink, S. Weckbach, M. Lenhard, B. Schmidt, T. Flohr, M. F. Reiser, and C. R. Becker. 2007. Material differentiation by dual energy CT: initial experience. *Eur Radiol* 17: 1510-1517.
69. McCollough, C. H., S. Leng, L. Yu, and J. G. Fletcher. 2015. Dual- and Multi-Energy CT: Principles, Technical Approaches, and Clinical Applications. *Radiology* 276: 637-653.
70. Bushberg, J. T., J. A. Seibert, E. M. Leidholdt, and J. M. Boone. 2011. *The essential physics of medical imaging*. Wolters Kluwer Health/Lippincott Williams & Wilkins, Philadelphia :.

71. Primak, A. N., J. C. Ramirez Giraldo, X. Liu, L. Yu, and C. H. McCollough. 2009. Improved dual-energy material discrimination for dual-source CT by means of additional spectral filtration. *Med Phys* 36: 1359-1369.
72. Primak, A. N., J. C. Giraldo, C. D. Eusemann, B. Schmidt, B. Kantor, J. G. Fletcher, and C. H. McCollough. 2010. Dual-source dual-energy CT with additional tin filtration: Dose and image quality evaluation in phantoms and in vivo. *AJR Am J Roentgenol* 195: 1164-1174.
73. Li, B., G. Yadava, and J. Hsieh. 2011. Quantification of head and body CTDI(VOL) of dual-energy x-ray CT with fast-kVp switching. *Med Phys* 38: 2595-2601.
74. Xu, D., D. A. Langan, X. Wu, J. D. Pack, T. M. Benson, J. E. Tkaczky, and A. M. Schmitz. 2009. Dual energy CT via fast kVp switching spectrum estimation. *Proc SPIE Int Soc Opt Eng* 7258: Physics of Medical Imaging, 72583T.
75. Ananthakrishnan, L., P. Rajiah, R. Ahn, N. Rassouli, Y. Xi, T. C. Soesbe, M. A. Lewis, R. E. Lenkinski, J. R. Leyendecker, and S. Abbara. 2017. Spectral detector CT-derived virtual non-contrast images: comparison of attenuation values with unenhanced CT. *Abdom Radiol (NY)* 42: 702-709.
76. Ehn, S., T. Sellerer, D. Muenzel, A. A. Fingerle, F. Kopp, M. Duda, K. Mei, B. Renger, J. Herzen, J. Dangelmaier, B. J. Schwaiger, A. Sauter, I. Riederer, M. Renz, R. Braren, E. J. Rummeny, F. Pfeiffer, and P. B. Noel. 2018. Assessment of quantification accuracy and image quality of a full-body dual-layer spectral CT system. *J Appl Clin Med Phys* 19: 204-217.
77. Pelgrim, G. J., R. W. van Hamersvelt, M. J. Willemink, B. T. Schmidt, T. Flohr, A. Schilham, J. Milles, M. Oudkerk, T. Leiner, and R. Vliegenthart. 2017. Accuracy of iodine quantification using dual energy CT in latest generation dual source and dual layer CT. *Eur Radiol* 27: 3904-3912.

78. Carmi, R., G. Naveh, and A. Altman. 2005. Material separation with dual-layer CT. *IEEE Nuclear Science Symposium Conference Record* 4: 1876-1878.
79. Euler, A., M. M. Obmann, Z. Szucs-Farkas, A. Mileto, C. Zaehring, A. L. Falkowski, D. J. Winkel, D. Marin, B. Stieltjes, B. Krauss, and S. T. Schindera. 2018. Comparison of image quality and radiation dose between split-filter dual-energy images and single-energy images in single-source abdominal CT. *Eur Radiol*: [Epub ahead of print].
80. Rutt, B., and A. Fenster. 1980. Split-filter computed tomography: a simple technique for dual energy scanning. *J Comput Assist Tomogr* 4: 501-509.
81. Euler, A., A. Parakh, A. L. Falkowski, S. Manneck, D. Dashti, B. Krauss, Z. Szucs-Farkas, and S. T. Schindera. 2016. Initial Results of a Single-Source Dual-Energy Computed Tomography Technique Using a Split-Filter: Assessment of Image Quality, Radiation Dose, and Accuracy of Dual-Energy Applications in an In Vitro and In Vivo Study. *Invest Radiol* 51: 491-498.
82. Almeida, I. P., L. E. Schyns, M. C. Ollers, W. van Elmpt, K. Parodi, G. Landry, and F. Verhaegen. 2017. Dual-energy CT quantitative imaging: a comparison study between twin-beam and dual-source CT scanners. *Med Phys* 44: 171-179.
83. Jacobsen, M. C., D. Schellingerhout, C. A. Wood, E. P. Tamm, M. C. Godoy, J. Sun, and D. D. Cody. 2018. Intermanufacturer Comparison of Dual-Energy CT Iodine Quantification and Monochromatic Attenuation: A Phantom Study. *Radiology* 287: 224-234.
84. Kaemmerer, N., M. Brand, M. Hammon, M. May, W. Wuest, B. Krauss, M. Uder, and M. M. Lell. 2016. Dual-Energy Computed Tomography Angiography of the Head and Neck With Single-Source Computed Tomography: A New Technical (Split Filter) Approach for Bone Removal. *Invest Radiol* 51: 618-623.

85. Kaza, R. K., L. Ananthakrishnan, A. Kambadakone, and J. F. Platt. 2017. Update of Dual-Energy CT Applications in the Genitourinary Tract. *AJR Am J Roentgenol* 208: 1185-1192.
86. Diekhoff, T., T. Kiefer, A. Stroux, I. Pilhofer, R. Juran, J. Mews, J. Blobel, M. Tsuyuki, B. Ackermann, B. Hamm, and K.-G. A. Hermann. 2015. Detection and characterization of crystal suspensions using single-source dual-energy computed tomography: a phantom model of crystal arthropathies. *Investigative radiology* 50: 255-260.
87. Diekhoff, T., K. Ziegeler, E. Feist, T. Kiefer, J. Mews, B. Hamm, and K. G. Hermann. 2015. First experience with single-source dual-energy computed tomography in six patients with acute arthralgia: a feasibility experiment using joint aspiration as a reference. *Skeletal Radiol* 44: 1573-1577.
88. Kiefer, T., T. Diekhoff, S. Hermann, A. Stroux, J. Mews, J. Blobel, B. Hamm, and K. G. Hermann. 2016. Single source dual-energy computed tomography in the diagnosis of gout: Diagnostic reliability in comparison to digital radiography and conventional computed tomography of the feet. *Eur J Radiol* 85: 1829-1834.
89. Diekhoff, T., K. G. Hermann, M. Pumberger, B. Hamm, M. Putzier, and M. Fuchs. 2017. Dual-energy CT virtual non-calcium technique for detection of bone marrow edema in patients with vertebral fractures: A prospective feasibility study on a single- source volume CT scanner. *Eur J Radiol* 87: 59-65.
90. Kidoh, M., D. Utsunomiya, S. Oda, T. Nakaura, Y. Funama, H. Yuki, K. Hirata, M. Hatemura, T. Namimoto, and Y. Yamashita. 2017. CT venography after knee replacement surgery: comparison of dual-energy CT-based monochromatic imaging and single-energy metal artifact reduction techniques on a 320-row CT scanner. *Acta radiologica open* 6: 2058460117693463.

91. Na, D., S. J. Hong, M. A. Yoon, K. S. Ahn, C. H. Kang, B. H. Kim, and Y. Jang. 2016. Spinal Bone Bruise: Can Computed Tomography (CT) Enable Accurate Diagnosis? *Acad Radiol* 23: 1376-1383.
92. Macovski, A., R. E. Alvarez, J. L. Chan, J. P. Stonestrom, and L. M. Zatz. 1976. Energy dependent reconstruction in X-ray computerized tomography. *Computers in biology and medicine* 6: 325-336.
93. Marshall, W. H., Jr., R. Alvarez, A. Macovski, J. Healy, and L. M. Zatz. 1978. Dual kilovoltage at computed tomography: a prereconstruction method for estimation of effective atomic number and electron density. *Neuroradiology* 16: 605-606.
94. Marshall, W. H., Jr., R. E. Alvarez, and A. Macovski. 1981. Initial results with prereconstruction dual-energy computed tomography (PREDECT). *Radiology* 140: 421-430.
95. Maass, C., E. Meyer, and M. Kachelriess. 2011. Exact dual energy material decomposition from inconsistent rays (MDIR). *Med Phys* 38: 691-700.
96. Liu, X., L. Yu, A. N. Primak, and C. H. McCollough. 2009. Quantitative imaging of element composition and mass fraction using dual-energy CT: three-material decomposition. *Med Phys* 36: 1602-1609.
97. Maass, C., M. Baer, and M. Kachelriess. 2009. Image-based dual energy CT using optimized precorrection functions: a practical new approach of material decomposition in image domain. *Med Phys* 36: 3818-3829.
98. Zhao, W., T. Niu, L. Xing, Y. Xie, G. Xiong, K. Elmore, J. Zhu, L. Wang, and J. K. Min. 2016. Using edge-preserving algorithm with non-local mean for significantly improved image-domain material decomposition in dual-energy CT. *Phys Med Biol* 61: 1332-1351.
99. Kaza, R. K., J. F. Platt, and A. J. Megibow. 2013. Dual-energy CT of the urinary tract. *Abdom Imaging* 38: 167-179.

100. Fletcher, J. G., N. Takahashi, R. Hartman, L. Guimaraes, J. E. Huprich, D. M. Hough, L. Yu, and C. H. McCollough. 2009. Dual-energy and dual-source CT: is there a role in the abdomen and pelvis? *Radiol Clin North Am* 47: 41-57.
101. Flohr, T. G., C. H. McCollough, H. Bruder, M. Petersilka, K. Gruber, C. Suss, M. Grasruck, K. Stierstorfer, B. Krauss, R. Raupach, A. N. Primak, A. Kuttner, S. Achenbach, C. Becker, A. Kopp, and B. M. Ohnesorge. 2006. First performance evaluation of a dual-source CT (DSCT) system. *Eur Radiol* 16: 256-268.
102. Chandarana, H., A. J. Megibow, B. A. Cohen, R. Srinivasan, D. Kim, C. Leidecker, and M. Macari. 2011. Iodine quantification with dual-energy CT: phantom study and preliminary experience with renal masses. *AJR Am J Roentgenol* 196: W693-700.
103. Kawai, T., M. Takeuchi, M. Hara, K. Ohashi, H. Suzuki, K. Yamada, Y. Sugimura, and Y. Shibamoto. 2013. Accuracy of iodine removal using dual-energy CT with or without a tin filter: an experimental phantom study. *Acta Radiol* 54: 954-960.
104. Krauss, B., K. L. Grant, B. T. Schmidt, and T. G. Flohr. 2015. The importance of spectral separation: an assessment of dual-energy spectral separation for quantitative ability and dose efficiency. *Invest Radiol* 50: 114-118.
105. Mileto, A., D. Marin, J. C. Ramirez-Giraldo, E. Scribano, B. Krauss, S. Mazziotti, and G. Ascenti. 2014. Accuracy of contrast-enhanced dual-energy MDCT for the assessment of iodine uptake in renal lesions. *AJR Am J Roentgenol* 202: W466-474.
106. De Cecco, C. N., V. Buffa, S. Fedeli, A. Vallone, R. Ruopoli, M. Luzietti, V. Miele, M. Rengo, M. Maurizi Enrici, P. Fina, A. Laghi, and V. David. 2010. Preliminary experience with abdominal dual-energy CT (DECT): true versus virtual nonenhanced images of the liver. *La Radiologia medica* 115: 1258-1266.
107. Toepker, M., T. Moritz, B. Krauss, M. Weber, G. Euller, T. Mang, F. Wolf, C. J. Herold, and H. Ringl. 2012. Virtual non-contrast in second-generation, dual-energy computed tomography: reliability of attenuation values. *Eur J Radiol* 81: 398-405.

108. Duan, X., G. Arbique, J. Guild, Y. Xi, and J. Anderson. 2018. Technical Note: Quantitative accuracy evaluation for spectral images from a detector-based spectral CT scanner using an iodine phantom. *Med Phys*: [Epub ahead of print].
109. Zarzour, J. G., D. Milner, R. Valentin, B. E. Jackson, J. Gordetsky, J. West, S. Rais-Bahrami, and D. E. Morgan. 2017. Quantitative iodine content threshold for discrimination of renal cell carcinomas using rapid kV-switching dual-energy CT. *Abdom Radiol (NY)* 42: 727-734.
110. Marin, D., D. Davis, K. Roy Choudhury, B. Patel, R. T. Gupta, A. Mileto, and R. C. Nelson. 2017. Characterization of Small Focal Renal Lesions: Diagnostic Accuracy with Single-Phase Contrast-enhanced Dual-Energy CT with Material Attenuation Analysis Compared with Conventional Attenuation Measurements. *Radiology* 284: 737-747.
111. Mileto, A., D. Marin, M. Alfaro-Cordoba, J. C. Ramirez-Giraldo, C. D. Eusemann, E. Scribano, A. Blandino, S. Mazziotti, and G. Ascenti. 2014. Iodine quantification to distinguish clear cell from papillary renal cell carcinoma at dual-energy multidetector CT: a multireader diagnostic performance study. *Radiology* 273: 813-820.
112. Schabel, C., B. Patel, S. Harring, P. Duvnjak, J. C. Ramirez-Giraldo, K. Nikolaou, R. C. Nelson, A. E. Farjat, and D. Marin. 2018. Renal Lesion Characterization with Spectral CT: Determining the Optimal Energy for Virtual Monoenergetic Reconstruction. *Radiology*: [Epub ahead of print].
113. Kato, T., K. Uehara, S. Ishigaki, T. Nishashi, A. Arimoto, H. Nakamura, T. Kamiya, T. Oshiro, T. Ebata, and M. Nagino. 2015. Clinical significance of dual-energy CT-derived iodine quantification in the diagnosis of metastatic LN in colorectal cancer. *European journal of surgical oncology : the journal of the European Society of Surgical Oncology and the British Association of Surgical Oncology* 41: 1464-1470.

114. Lam, S., R. Gupta, M. Levental, E. Yu, H. D. Curtin, and R. Forghani. 2015. Optimal Virtual Monochromatic Images for Evaluation of Normal Tissues and Head and Neck Cancer Using Dual-Energy CT. *AJNR Am J Neuroradiol* 36: 1518-1524.
115. Rizzo, S., D. Radice, M. Femia, P. De Marco, D. Origgi, L. Preda, M. Barberis, R. Vigorito, G. Mauri, A. Mauro, and M. Bellomi. 2018. Metastatic and non-metastatic lymph nodes: quantification and different distribution of iodine uptake assessed by dual-energy CT. *Eur Radiol* 28: 760-769.
116. Tawfik, A. M., A. A. Razek, J. M. Kerl, N. E. Nour-Eldin, R. Bauer, and T. J. Vogl. 2014. Comparison of dual-energy CT-derived iodine content and iodine overlay of normal, inflammatory and metastatic squamous cell carcinoma cervical lymph nodes. *Eur Radiol* 24: 574-580.
117. Macari, M., B. Spieler, D. Kim, A. Graser, A. J. Megibow, J. Babb, and H. Chandarana. 2010. Dual-source dual-energy MDCT of pancreatic adenocarcinoma: initial observations with data generated at 80 kVp and at simulated weighted-average 120 kVp. *AJR Am J Roentgenol* 194: W27-32.
118. Gupta, S., N. Wagner-Bartak, C. T. Jensen, A. Hui, W. Wei, P. Lertdilok, A. Qayyum, and E. P. Tamm. 2016. Dual-energy CT of pancreatic adenocarcinoma: reproducibility of primary tumor measurements and assessment of tumor conspicuity and margin sharpness. *Abdom Radiol (NY)* 41: 1317-1324.
119. Benveniste, A. P., S. de Castro Faria, G. Broering, D. M. Ganeshan, E. P. Tamm, R. B. Iyer, and P. Bhosale. 2017. Potential Application of Dual-Energy CT in Gynecologic Cancer: Initial Experience. *AJR Am J Roentgenol* 208: 695-705.
120. Tijssen, M. P., P. A. Hofman, A. A. Stadler, W. van Zwam, R. de Graaf, R. J. van Oostenbrugge, E. Klotz, J. E. Wildberger, and A. A. Postma. 2014. The role of dual energy CT in differentiating between brain haemorrhage and contrast medium after mechanical revascularisation in acute ischaemic stroke. *Eur Radiol* 24: 834-840.

121. Khalilzadeh, O., B. Sabel, Y. Sung, A. Parikh, C. M. Phan, J. Dinkel, A. J. Yoo, J. Romero, and R. Gupta. 2014. Temporal evolution of intraparenchymal hyperdensity after intra-arterial therapy in patients with ischemic stroke: optimal discrimination between hemorrhage and iodinated contrast. *Clin Neuroradiol* 24: 365-371.
122. Phan, C. M., A. J. Yoo, J. A. Hirsch, R. G. Nogueira, and R. Gupta. 2012. Differentiation of hemorrhage from iodinated contrast in different intracranial compartments using dual-energy head CT. *AJNR Am J Neuroradiol* 33: 1088-1094.
123. Gupta, R., C. M. Phan, C. Leidecker, T. J. Brady, J. A. Hirsch, R. G. Nogueira, and A. J. Yoo. 2010. Evaluation of dual-energy CT for differentiating intracerebral hemorrhage from iodinated contrast material staining. *Radiology* 257: 205-211.
124. Grant, K. L., T. G. Flohr, B. Krauss, M. Sedlmair, C. Thomas, and B. Schmidt. 2014. Assessment of an Advanced Image-Based Technique to Calculate Virtual Monoenergetic Computed Tomographic Images From a Dual-Energy Examination to Improve Contrast-To-Noise Ratio in Examinations Using Iodinated Contrast Media. *Invest Radiol* 49: 586-592.
125. Yu, L., J. A. Christner, S. Leng, J. Wang, J. G. Fletcher, and C. H. McCollough. 2011. Virtual monochromatic imaging in dual-source dual-energy CT: radiation dose and image quality. *Med Phys* 38: 6371-6379.
126. Yu, L., S. Leng, and C. H. McCollough. 2012. Dual-energy CT-based monochromatic imaging. *AJR Am J Roentgenol* 199: S9-S15.
127. Postma, A. A., P. A. Hofman, A. A. Stadler, R. J. van Oostenbrugge, M. P. Tijssen, and J. E. Wildberger. 2012. Dual-energy CT of the brain and intracranial vessels. *AJR Am J Roentgenol* 199: S26-33.
128. Mannil, M., J. Ramachandran, I. Vittoria de Martini, S. Wegener, B. Schmidt, T. Flohr, B. Krauss, A. Valavanis, H. Alkadhi, and S. Winklhofer. 2017. Modified Dual-Energy Algorithm for Calcified Plaque Removal: Evaluation in Carotid Computed Tomography

- Angiography and Comparison With Digital Subtraction Angiography. *Invest Radiol* 52: 680-685.
129. Ali, I. T., W. D. Wong, T. Liang, F. Khosa, M. Mian, S. Jalal, and S. Nicolaou. 2018. Clinical Utility of Dual-Energy CT Analysis of Bone Marrow Edema in Acute Wrist Fractures. *AJR Am J Roentgenol* 210: 842-847.
 130. Dareez, N. M., K. H. Dahlslett, E. Engesland, and E. S. Lindland. 2017. Scaphoid fracture: Bone marrow edema detected with dual-energy CT virtual non-calcium images and confirmed with MRI. *Skeletal Radiol* 46: 1753-1756.
 131. Frellesen, C., M. Azadegan, S. S. Martin, K. Otani, T. D'Angelo, C. Booz, K. Eichler, B. Panahi, M. Kaup, R. W. Bauer, T. J. Vogl, and J. L. Wichmann. 2018. Dual-Energy Computed Tomography-Based Display of Bone Marrow Edema in Incidental Vertebral Compression Fractures: Diagnostic Accuracy and Characterization in Oncological Patients Undergoing Routine Staging Computed Tomography. *Invest Radiol*.
 132. Kosmala, A., A. M. Weng, A. Heidemeier, B. Krauss, S. Knop, T. A. Bley, and B. Petritsch. 2018. Multiple Myeloma and Dual-Energy CT: Diagnostic Accuracy of Virtual Noncalcium Technique for Detection of Bone Marrow Infiltration of the Spine and Pelvis. *Radiology* 286: 205-213.
 133. Wichmann, J. L., C. Booz, S. Wesarg, K. Kafchitsas, R. W. Bauer, J. M. Kerl, T. Lehnert, T. J. Vogl, and M. F. Khan. 2014. Dual-energy CT-based phantomless in vivo three-dimensional bone mineral density assessment of the lumbar spine. *Radiology* 271: 778-784.
 134. Wichmann, J. L., C. Booz, S. Wesarg, R. W. Bauer, J. M. Kerl, S. Fischer, T. Lehnert, T. J. Vogl, M. F. Khan, and K. Kafchitsas. 2015. Quantitative dual-energy CT for phantomless evaluation of cancellous bone mineral density of the vertebral pedicle: correlation with pedicle screw pull-out strength. *Eur Radiol* 25: 1714-1720.

135. Nute, J. L., L. Le Roux, A. G. Chandler, V. Baladandayuthapani, D. Schellingerhout, and D. D. Cody. 2015. Differentiation of low-attenuation intracranial hemorrhage and calcification using dual-energy computed tomography in a phantom system. *Invest Radiol* 50: 9-16.
136. Nute, J. L., M. C. Jacobsen, A. Chandler, D. D. Cody, and D. Schellingerhout. 2017. Dual-Energy Computed Tomography for the Characterization of Intracranial Hemorrhage and Calcification: A Systematic Approach in a Phantom System. *Invest Radiol* 52: 30-41.
137. Hu, R., L. Daftari Besheli, J. Young, M. Wu, S. Pomerantz, M. H. Lev, and R. Gupta. 2016. Dual-Energy Head CT Enables Accurate Distinction of Intraparenchymal Hemorrhage from Calcification in Emergency Department Patients. *Radiology* 280: 177-183.
138. Naruto, N., H. Tannai, K. Nishikawa, K. Yamagishi, M. Hashimoto, H. Kawabe, Y. Kamisaki, H. Sumiya, S. Kuroda, and K. Noguchi. 2018. Dual-energy bone removal computed tomography (BRCT): preliminary report of efficacy of acute intracranial hemorrhage detection. *Emergency radiology* 25: 29-33.
139. Hu, X. Y., Z. F. Ge, C. S. Zee, and X. Y. Gong. 2012. Differentiation of white and red thrombus with magnetic resonance imaging: a phantom study. *Chin Med J (Engl)* 125: 1889-1892.
140. Schenck, J. F. 1996. The role of magnetic susceptibility in magnetic resonance imaging: MRI magnetic compatibility of the first and second kinds. *Med Phys* 23: 815-850.
141. Yamada, N., S. Imakita, T. Sakuma, and M. Takamiya. 1996. Intracranial calcification on gradient-echo phase image: depiction of diamagnetic susceptibility. *Radiology* 198: 171-178.
142. Gupta, R. K., S. B. Rao, R. Jain, L. Pal, R. Kumar, S. K. Venkatesh, and R. K. Rathore. 2001. Differentiation of calcification from chronic hemorrhage with corrected gradient echo phase imaging. *J Comput Assist Tomogr* 25: 698-704.

143. Zhu, W. Z., J. P. Qi, C. J. Zhan, H. G. Shu, L. Zhang, C. Y. Wang, L. M. Xia, J. W. Hu, and D. Y. Feng. 2008. Magnetic resonance susceptibility weighted imaging in detecting intracranial calcification and hemorrhage. *Chin Med J (Engl)* 121: 2021-2025.
144. Wu, Z., S. Mittal, K. Kish, Y. Yu, J. Hu, and E. M. Haacke. 2009. Identification of calcification with MRI using susceptibility-weighted imaging: a case study. *J Magn Reson Imaging* 29: 177-182.
145. Bullivant, J. P., S. Zhao, B. J. Willenberg, B. Kozissnik, C. D. Batich, and J. Dobson. 2013. Materials characterization of Feraheme/ferumoxytol and preliminary evaluation of its potential for magnetic fluid hyperthermia. *Int J Mol Sci* 14: 17501-17510.
146. Bernstein, M. A., K. F. King, and X. J. Zhou. 2004. *Handbook of MRI pulse sequences*. Academic Press, Amsterdam; Boston.
147. Haacke, E. M. 1999. *Magnetic resonance imaging : physical principles and sequence design*. Wiley, New York.
148. Haacke, E. M., S. Liu, S. Buch, W. Zheng, D. Wu, and Y. Ye. 2015. Quantitative susceptibility mapping: current status and future directions. *Magn Reson Imaging* 33: 1-25.
149. Lan, T., D. Erdogmus, S. J. Hayflick, and J. U. Szumowski. Phase unwrapping and background correction in MRI. *Proc IEEE*. 239-243.
150. Rauscher, A., M. Barth, J. R. Reichenbach, R. Stollberger, and E. Moser. 2003. Automated unwrapping of MR phase images applied to BOLD MR-venography at 3 Tesla. *J Magn Reson Imaging* 18: 175-180.
151. Maier, F., D. Fuentes, J. S. Weinberg, J. D. Hazle, and R. J. Stafford. 2015. Robust phase unwrapping for MR temperature imaging using a magnitude-sorted list, multi-clustering algorithm. *Magn Reson Med* 73: 1662-1668.
152. Deistung, A., F. Schweser, and J. R. Reichenbach. 2017. Overview of quantitative susceptibility mapping. *NMR Biomed* 30: e3569.

153. Schweser, F., S. D. Robinson, L. de Rochefort, W. Li, and K. Bredies. 2017. An illustrated comparison of processing methods for phase MRI and QSM: removal of background field contributions from sources outside the region of interest. *NMR Biomed* 30: e3604.
154. Liu, T., I. Khalidov, L. de Rochefort, P. Spincemille, J. Liu, A. J. Tsiouris, and Y. Wang. 2011. A novel background field removal method for MRI using projection onto dipole fields (PDF). *NMR Biomed* 24: 1129-1136.
155. Liu, J., D. A. Rudko, J. S. Gati, R. S. Menon, and M. Drangova. 2015. Inter-echo variance as a weighting factor for multi-channel combination in multi-echo acquisition for local frequency shift mapping. *Magn Reson Med* 73: 1654-1661.
156. Koopmans, P. J., R. Manniesing, W. J. Niessen, M. A. Viergever, and M. Barth. 2008. MR venography of the human brain using susceptibility weighted imaging at very high field strength. *MAGMA* 21: 149-158.
157. de Rochefort, L., R. Brown, M. R. Prince, and Y. Wang. 2008. Quantitative MR susceptibility mapping using piece-wise constant regularized inversion of the magnetic field. *Magn Reson Med* 60: 1003-1009.
158. Langham, M. C., J. F. Magland, T. F. Floyd, and F. W. Wehrli. 2009. Retrospective correction for induced magnetic field inhomogeneity in measurements of large-vessel hemoglobin oxygen saturation by MR susceptometry. *Magn Reson Med* 61: 626-633.
159. Yao, B., T. Q. Li, P. Gelderen, K. Shmueli, J. A. de Zwart, and J. H. Duyn. 2009. Susceptibility contrast in high field MRI of human brain as a function of tissue iron content. *Neuroimage* 44: 1259-1266.
160. Neelavalli, J., Y. C. Cheng, J. Jiang, and E. M. Haacke. 2009. Removing background phase variations in susceptibility-weighted imaging using a fast, forward-field calculation. *J Magn Reson Imaging* 29: 937-948.

161. Haacke, E. M., and J. R. Reichenbach. 2011. *Susceptibility weighted imaging in MRI : basic concepts and clinical applications*. Wiley-Blackwell, Hoboken, N.J.
162. Haacke, E. M., S. Mittal, Z. Wu, J. Neelavalli, and Y. C. Cheng. 2009. Susceptibility-weighted imaging: technical aspects and clinical applications, part 1. *AJNR Am J Neuroradiol* 30: 19-30.
163. Haacke, E. M., Y. Xu, Y. C. Cheng, and J. R. Reichenbach. 2004. Susceptibility weighted imaging (SWI). *Magn Reson Med* 52: 612-618.
164. Reichenbach, J. R., M. Essig, E. M. Haacke, B. C. Lee, C. Przetak, W. A. Kaiser, and L. R. Schad. 1998. High-resolution venography of the brain using magnetic resonance imaging. *MAGMA* 6: 62-69.
165. Reichenbach, J. R., and E. M. Haacke. 2001. High-resolution BOLD venographic imaging: a window into brain function. *NMR Biomed* 14: 453-467.
166. Reichenbach, J. R., F. Schweser, B. Serres, and A. Deistung. 2015. Quantitative Susceptibility Mapping: Concepts and Applications. *Clin Neuroradiol* 25 Suppl 2: 225-230.
167. Liu, J., T. Liu, L. de Rochefort, J. Ledoux, I. Khalidov, W. Chen, A. J. Tsiouris, C. Wisnieff, P. Spincemille, M. R. Prince, and Y. Wang. 2012. Morphology enabled dipole inversion for quantitative susceptibility mapping using structural consistency between the magnitude image and the susceptibility map. *Neuroimage* 59: 2560-2568.
168. Lauzon, M. L., C. R. McCreary, D. A. McLean, M. Salluzzi, and R. Frayne. 2017. Quantitative susceptibility mapping at 3 T: comparison of acquisition methodologies. *NMR Biomed* 30: e3492.
169. Liu, Z., Y. Kee, D. Zhou, Y. Wang, and P. Spincemille. 2017. Preconditioned total field inversion (TFI) method for quantitative susceptibility mapping. *Magn Reson Med* 78: 303-315.

170. Schweser, F., A. Deistung, B. W. Lehr, and J. R. Reichenbach. 2011. Quantitative imaging of intrinsic magnetic tissue properties using MRI signal phase: an approach to in vivo brain iron metabolism? *Neuroimage* 54: 2789-2807.
172. Wharton, S., and R. Bowtell. 2010. Whole-brain susceptibility mapping at high field: a comparison of multiple- and single-orientation methods. *Neuroimage* 53: 515-525.
173. Wharton, S., A. Schafer, and R. Bowtell. 2010. Susceptibility mapping in the human brain using threshold-based k-space division. *Magn Reson Med* 63: 1292-1304.
174. Tang, J., S. Liu, J. Neelavalli, Y. C. Cheng, S. Buch, and E. M. Haacke. 2013. Improving susceptibility mapping using a threshold-based K-space/image domain iterative reconstruction approach. *Magn Reson Med* 69: 1396-1407.
175. Schweser, F., A. Deistung, K. Sommer, and J. R. Reichenbach. 2013. Toward online reconstruction of quantitative susceptibility maps: superfast dipole inversion. *Magn Reson Med* 69: 1582-1594.
176. Shmueli, K., J. A. de Zwart, P. van Gelderen, T. Q. Li, S. J. Dodd, and J. H. Duyn. 2009. Magnetic susceptibility mapping of brain tissue in vivo using MRI phase data. *Magn Reson Med* 62: 1510-1522.
177. Li, W., B. Wu, and C. Liu. 2011. Quantitative susceptibility mapping of human brain reflects spatial variation in tissue composition. *Neuroimage* 55: 1645-1656.
178. Li, W., N., F. Yu, H. Han, W. Cao, R. Romero, B. Tantiwongkosi, T. Q. Duong, and C. Liu. 2015. A method for estimating and removing streaking artifacts in quantitative susceptibility mapping. *Neuroimage* 108: 111-122.
179. Bilgic, B., I. Chatnuntawech, A. P. Fan, K. Setsompop, S. F. Cauley, L. L. Wald, and E. Adalsteinsson. 2014. Fast image reconstruction with L2-regularization. *J Magn Reson Imaging* 40: 181-191.

180. Kressler, B., L. de Rochefort, T. Liu, P. Spincemaille, Q. Jiang, and Y. Wang. 2010. Nonlinear regularization for per voxel estimation of magnetic susceptibility distributions from MRI field maps. *IEEE Trans Med Imaging* 29: 273-281.
181. de Rochefort, L., T. Liu, B. Kressler, J. Liu, P. Spincemaille, V. Lebon, J. Wu, and Y. Wang. 2010. Quantitative susceptibility map reconstruction from MR phase data using bayesian regularization: validation and application to brain imaging. *Magn Reson Med* 63: 194-206.
182. Liu, T., J. Liu, L. de Rochefort, P. Spincemaille, I. Khalidov, J. R. Ledoux, and Y. Wang. 2011. Morphology enabled dipole inversion (MEDI) from a single-angle acquisition: comparison with COSMOS in human brain imaging. *Magn Reson Med* 66: 777-783.
183. Liu, T., W. Xu, P. Spincemaille, A. S. Avestimehr, and Y. Wang. 2012. Accuracy of the morphology enabled dipole inversion (MEDI) algorithm for quantitative susceptibility mapping in MRI. *IEEE Trans Med Imaging* 31: 816-824.
184. Schweser, F., K. Sommer, A. Deistung, and J. R. Reichenbach. 2012. Quantitative susceptibility mapping for investigating subtle susceptibility variations in the human brain. *Neuroimage* 62: 2083-2100.
185. He, X., and D. A. Yablonskiy. 2009. Biophysical mechanisms of phase contrast in gradient echo MRI. *Proceedings of the National Academy of Sciences of the United States of America* 106: 13558-13563.
186. Kang, S. H., Y. Li, M. Fukaya, I. Lorenzini, D. W. Cleveland, L. W. Ostrow, J. D. Rothstein, and D. E. Bergles. 2013. Degeneration and impaired regeneration of gray matter oligodendrocytes in amyotrophic lateral sclerosis. *Nat Neurosci* 16: 571-579.
187. Giacomini, P. S., I. R. Levesque, L. Ribeiro, S. Narayanan, S. J. Francis, G. B. Pike, and D. L. Arnold. 2009. Measuring demyelination and remyelination in acute multiple sclerosis lesion voxels. *Arch Neurol* 66: 375-381.

188. Nagesh, V., C. I. Tsien, T. L. Chenevert, B. D. Ross, T. S. Lawrence, L. Junick, and Y. Cao. 2008. Radiation-induced changes in normal-appearing white matter in patients with cerebral tumors: a diffusion tensor imaging study. *Int J Radiat Oncol Biol Phys* 70: 1002-1010.
189. Nazem-Zadeh, M. R., C. H. Chapman, T. L. Lawrence, C. I. Tsien, and Y. Cao. 2012. Radiation therapy effects on white matter fiber tracts of the limbic circuit. *Med Phys* 39: 5603-5613.
190. Chen, W., S. A. Gauthier, A. Gupta, J. Comunale, T. Liu, S. Wang, M. Pei, D. Pitt, and Y. Wang. 2014. Quantitative susceptibility mapping of multiple sclerosis lesions at various ages. *Radiology* 271: 183-192.
191. Langkammer, C., T. Liu, M. Khalil, C. Enzinger, M. Jehna, S. Fuchs, F. Fazekas, Y. Wang, and S. Ropele. 2013. Quantitative susceptibility mapping in multiple sclerosis. *Radiology* 267: 551-559.
192. Wang, S., M. Lou, T. Liu, D. Cui, X. Chen, and Y. Wang. 2013. Hematoma volume measurement in gradient echo MRI using quantitative susceptibility mapping. *Stroke* 44: 2315-2317.
193. Dietrich, O., J. Levin, S. A. Ahmadi, A. Plate, M. F. Reiser, K. Botzel, A. Giese, and B. Ertl-Wagner. 2017. MR imaging differentiation of Fe²⁺ and Fe³⁺ based on relaxation and magnetic susceptibility properties. *Neuroradiology* 59: 403-409.
194. Gho, S. M., J. Shin, M. O. Kim, and D. H. Kim. 2015. Simultaneous quantitative mapping of conductivity and susceptibility using a double-echo ultrashort echo time sequence: Example using a hematoma evolution study. Department of Electrical and Electronic Engineering Institute of BioMed-IT, Energy-IT and Smart-IT Technology, Yonsei University Seoul Republic of Korea.

195. Liu, T., K. Surapaneni, M. Lou, L. Cheng, P. Spincemaille, and Y. Wang. 2012. Cerebral microbleeds: burden assessment by using quantitative susceptibility mapping. *Radiology* 262: 269-278.
196. Liu, J., S. Xia, R. Hanks, N. Wiseman, C. Peng, S. Zhou, E. M. Haacke, and Z. Kou. 2016. Susceptibility Weighted Imaging and Mapping of Micro-Hemorrhages and Major Deep Veins after Traumatic Brain Injury. *J Neurotrauma* 33: 10-21.
197. Liu, W., K. Soderlund, J. S. Senseney, D. Joy, P. H. Yeh, J. Ollinger, E. B. Sham, T. Liu, Y. Wang, T. R. Oakes, and G. Riedy. 2016. Imaging Cerebral Microhemorrhages in Military Service Members with Chronic Traumatic Brain Injury. *Radiology* 278: 536-545.
198. Eskreis-Winkler, S., K. Deh, A. Gupta, T. Liu, C. Wisnieff, M. Jin, S. A. Gauthier, Y. Wang, and P. Spincemaille. 2015. Multiple sclerosis lesion geometry in quantitative susceptibility mapping (QSM) and phase imaging. *J Magn Reson Imaging* 42: 224-229.
199. Wisnieff, C., S. Ramanan, J. Olesik, S. Gauthier, Y. Wang, and D. Pitt. 2015. Quantitative susceptibility mapping (QSM) of white matter multiple sclerosis lesions: Interpreting positive susceptibility and the presence of iron. *Magn Reson Med* 74: 564-570.
200. Haacke, E. M., J. Tang, J. Neelavalli, and Y. C. Cheng. 2010. Susceptibility mapping as a means to visualize veins and quantify oxygen saturation. *J Magn Reson Imaging* 32: 663-676.
201. Liu, C., W. Li, K. A. Tong, K. W. Yeom, and S. Kuzminski. 2015. Susceptibility-weighted imaging and quantitative susceptibility mapping in the brain. *J Magn Reson Imaging* 42: 23-41.
202. Acosta-Cabronero, J., M. J. Betts, A. Cardenas-Blanco, S. Yang, and P. J. Nestor. 2016. In Vivo MRI Mapping of Brain Iron Deposition across the Adult Lifespan. *J Neurosci* 36: 364-374.

203. Santin, M. D., M. Didier, R. Valabregue, L. Yahia Cherif, D. Garcia-Lorenzo, P. Loureiro de Sousa, E. Bardinet, and S. Lehericy. 2017. Reproducibility of R2 * and quantitative susceptibility mapping (QSM) reconstruction methods in the basal ganglia of healthy subjects. *NMR Biomed* 30: e3491.
204. Duyn, J. H., and J. Schenck. 2017. Contributions to magnetic susceptibility of brain tissue. *NMR Biomed* 30: e3546.
205. Deistung, A., F. Schweser, B. Wiestler, M. Abello, M. Roethke, F. Sahm, W. Wick, A. M. Nagel, S. Heiland, H. P. Schlemmer, M. Bendszus, J. R. Reichenbach, and A. Radbruch. 2013. Quantitative susceptibility mapping differentiates between blood depositions and calcifications in patients with glioblastoma. *PLoS One* 8: e57924.
206. Schweser, F., A. Deistung, B. W. Lehr, and J. R. Reichenbach. 2010. Differentiation between diamagnetic and paramagnetic cerebral lesions based on magnetic susceptibility mapping. *Med Phys* 37: 5165-5178.
207. Berberat, J., R. Grobholz, L. Boxheimer, S. Rogers, L. Remonda, and U. Roelcke. 2014. Differentiation between calcification and hemorrhage in brain tumors using susceptibility-weighted imaging: a pilot study. *AJR Am J Roentgenol* 202: 847-850.
208. Fatemi-Ardekani, A., C. Boylan, and M. D. Noseworthy. 2009. Identification of breast calcification using magnetic resonance imaging. *Med Phys* 36: 5429-5436.
209. Langkammer, C., N. Krebs, W. Goessler, E. Scheurer, F. Ebner, K. Yen, F. Fazekas, and S. Ropele. 2010. Quantitative MR imaging of brain iron: a postmortem validation study. *Radiology* 257: 455-462.
210. Rossi, M., H. Ruottinen, I. Elovaara, P. Ryymin, S. Soimakallio, H. Eskola, and P. Dastidar. 2010. Brain iron deposition and sequence characteristics in Parkinsonism: comparison of SWI, T(2)* maps, T(2)-weighted-, and FLAIR-SPACE. *Invest Radiol* 45: 795-802.

211. Tan, H., T. Liu, Y. Wu, J. Thacker, R. Shenkar, A. G. Mikati, C. Shi, C. Dykstra, Y. Wang, P. V. Prasad, R. R. Edelman, and I. A. Awad. 2014. Evaluation of iron content in human cerebral cavernous malformation using quantitative susceptibility mapping. *Invest Radiol* 49: 498-504.
212. Roy, B., S. Verma, R. Awasthi, R. K. Rathore, R. Venkatesan, S. A. Yoganathan, J. K. Das, K. N. Prasad, and R. K. Gupta. 2011. Correlation of phase values with CT Hounsfield and R2* values in calcified neurocysticercosis. *J Magn Reson Imaging* 34: 1060-1064.
213. Mustafi, D., X. Fan, B. Peng, S. Foxley, J. Palgen, and G. M. Newstead. 2015. Using MRI to detect and differentiate calcium oxalate and calcium hydroxyapatite crystals in air-bubble-free phantom. *Physica medica : PM : an international journal devoted to the applications of physics to medicine and biology : official journal of the Italian Association of Biomedical Physics (AIFB)* 31: 1075-1079.
214. Hardy, P. A., W. Kucharczyk, and R. M. Henkelman. 1990. Cause of signal loss in MR images of old hemorrhagic lesions. *Radiology* 174: 549-555.
215. Valdes Hernandez M del, C., A. Glatz, A. J. Kiker, D. A. Dickie, B. S. Aribisala, N. A. Royle, S. Munoz Maniega, M. E. Bastin, I. J. Deary, and J. M. Wardlaw. 2014. Differentiation of calcified regions and iron deposits in the ageing brain on conventional structural MR images. *J Magn Reson Imaging* 40: 324-333.
216. Deverdun, J., F. Molino, N. Menjot de Champfleury, and E. Le Bars. 2017. Validation of a quantitative susceptibility mapping acquisition and reconstruction pipeline using a new iron sucrose based MR susceptibility phantom. *Journal of neuroradiology. Journal de neuroradiologie* 44: 269-272.
217. Simchick, G., Z. Liu, T. Nagy, M. Xiong, and Q. Zhao. 2018. Assessment of MR-based R2* and quantitative susceptibility mapping for the quantification of liver iron concentration in a mouse model at 7T. *Magn Reson Med*: [Epub ahead of print].

218. Pauling, L., and C. D. Coryell. 1936. The Magnetic Properties and Structure of Hemoglobin, Oxyhemoglobin and Carbonmonoxyhemoglobin. *Proceedings of the National Academy of Sciences* 22: 210.
219. Bren, K. L., R. Eisenberg, and H. B. Gray. 2015. Discovery of the magnetic behavior of hemoglobin: A beginning of bioinorganic chemistry. *Proceedings of the National Academy of Sciences* 112: 13123.
220. Dietrich, O., J. Levin, S. A. Ahmadi, A. Plate, M. F. Reiser, K. Botzel, A. Giese, and B. Ertl-Wagner. 2017. MR imaging differentiation of Fe(2+) and Fe(3+) based on relaxation and magnetic susceptibility properties. *Neuroradiology* 59: 403-409.
221. Jiang, H., J. Wang, J. Rogers, and J. Xie. 2017. Brain Iron Metabolism Dysfunction in Parkinson's Disease. *Molecular neurobiology* 54: 3078-3101.
222. Sofic, E., P. Riederer, H. Heinsen, H. Beckmann, G. P. Reynolds, G. Hebenstreit, and M. B. Youdim. 1988. Increased iron (III) and total iron content in post mortem substantia nigra of parkinsonian brain. *Journal of neural transmission* 74: 199-205.
223. Gardner, B., B. V. Dieriks, S. Cameron, L. H. S. Mendis, C. Turner, R. L. M. Faull, and M. A. Curtis. 2017. Metal concentrations and distributions in the human olfactory bulb in Parkinson's disease. *Scientific reports* 7: 10454.
224. Langkammer, C., F. Schweser, N. Krebs, A. Deistung, W. Goessler, E. Scheurer, K. Sommer, G. Reishofer, K. Yen, F. Fazekas, S. Ropele, and J. R. Reichenbach. 2012. Quantitative susceptibility mapping (QSM) as a means to measure brain iron? A post mortem validation study. *NeuroImage* 62: 1593-1599.
225. 2015. INFed (Iron Dextran Injection, USP) Safety Data Sheet. Actavis, ed, Parsippany-Troy Hills, NJ.
226. Berger, M., J. Hubbell, S. Seltzer, J. Chang, J. Coursey, R. Sukumar, D. Zucker, and K. Olsen. March 1998. XCOM: Photon Cross Section Database. Version 1.5 ed. National Institute of Standards and Technology.

227. Kato, H., M. Kuroda, K. Yoshimura, A. Yoshida, K. Hanamoto, S. Kawasaki, K. Shibuya, and S. Kanazawa. 2005. Composition of MRI phantom equivalent to human tissues. *Med Phys* 32: 3199-3208.
228. Hattori, K., Y. Ikemoto, W. Takao, S. Ohno, T. Harimoto, S. Kanazawa, M. Oita, K. Shibuya, M. Kuroda, and H. Kato. 2013. Development of MRI phantom equivalent to human tissues for 3.0-T MRI. *Med Phys* 40: 032303.
229. Wen, Y., D. Zhou, T. Liu, P. Spincemaille, and Y. Wang. 2014. An iterative spherical mean value method for background field removal in MRI. *Magn Reson Med* 72: 1065-1071.
230. Stüber, C., M. Morawski, A. Schäfer, C. Labadie, M. Wähnert, C. Leuze, M. Streicher, N. Barapatre, K. Reimann, S. Geyer, D. Spemann, and R. Turner. 2014. Myelin and iron concentration in the human brain: A quantitative study of MRI contrast. *NeuroImage* 93: 95-106.
231. Wu, Z., S. Li, J. Lei, D. An, and E. M. Haacke. 2010. Evaluation of traumatic subarachnoid hemorrhage using susceptibility-weighted imaging. *AJNR Am J Neuroradiol* 31: 1302-1310.
232. Chang, S., J. Zhang, T. Liu, A. J. Tsiouris, J. Shou, T. Nguyen, D. Leifer, Y. Wang, and I. Kovanlikaya. 2016. Quantitative Susceptibility Mapping of Intracerebral Hemorrhages at Various Stages. *Journal of magnetic resonance imaging : JMRI* 44: 420-425.
233. Wang, R., G. Xie, M. Zhai, Z. Zhang, B. Wu, D. Zheng, N. Hong, T. Jiang, B. Wen, and J. Cheng. 2017. Stability of R2* and quantitative susceptibility mapping of the brain tissue in a large scale multi-center study. *Sci Rep* 7: 45261.
234. Liu, T., J. Liu, L. de Rochefort, P. Spincemaille, I. Khalidov, J. R. Ledoux, and Y. Wang. 2011. Morphology enabled dipole inversion (MEDI) from a single-angle acquisition: comparison with COSMOS in human brain imaging. *Magn Reson Med* 66: 777-783.

235. Liu, T., C. Wisnieff, M. Lou, W. Chen, P. Spincemaille, and Y. Wang. 2013. Nonlinear formulation of the magnetic field to source relationship for robust quantitative susceptibility mapping. *Magn Reson Med* 69: 467-476.
236. Lin, J. S., D. T. Fuentes, A. Chandler, S. S. Prabhu, J. S. Weinberg, V. Baladandayuthapani, J. D. Hazle, and D. Schellingerhout. 2017. Performance Assessment for Brain MR Imaging Registration Methods. *AJNR Am J Neuroradiol* 38: 973-980.
237. Huisman, T. A. G. M. 2005. Intracranial hemorrhage: ultrasound, CT and MRI findings. *Eur Radiol* 15: 434-440.
238. Austin, P. C., and J. Merlo. 2017. Intermediate and advanced topics in multilevel logistic regression analysis. *Statistics in Medicine* 36: 3257-3277.
239. Yin, J., and L. Tian. 2014. Joint confidence region estimation for area under ROC curve and Youden index. *Stat Med* 33: 985-1000.
240. McNemar, Q. 1947. Note on the sampling error of the difference between correlated proportions or percentages. *Psychometrika* 12: 153-157.
241. Cohen, J. 1960. A Coefficient of Agreement for Nominal Scales. *Educ Psychol Meas* 20: 37-46.
242. Zweig, M. H., and G. Campbell. 1993. Receiver-operating characteristic (ROC) plots: a fundamental evaluation tool in clinical medicine. *Clinical chemistry* 39: 561-577.
243. Obuchowski, N. A. 2003. Receiver Operating Characteristic Curves and Their Use in Radiology. *Radiology* 229: 3-8.
244. Katki, H. A., Y. Li, D. W. Edelstein, and P. E. Castle. 2012. Estimating the agreement and diagnostic accuracy of two diagnostic tests when one test is conducted on only a subsample of specimens. *Statistics in medicine* 31: 10.1002/sim.4422.
245. Lachenbruch, P. A., and C. J. Lynch. 1998. Assessing screening tests: extensions of McNemar's test. *Stat Med* 17: 2207-2217.

246. Kidwell, C. S., J. A. Chalela, J. L. Saver, S. Starkman, M. D. Hill, A. M. Demchuk, J. A. Butman, N. Patronas, J. R. Alger, L. L. Latour, M. L. Luby, A. E. Baird, M. C. Leary, M. Tremwel, B. Ovbiagele, A. Fredieu, S. Suzuki, J. P. Villablanca, S. Davis, B. Dunn, J. W. Todd, M. A. Ezzeddine, J. Haymore, J. K. Lynch, L. Davis, and S. Warach. 2004. Comparison of MRI and CT for detection of acute intracerebral hemorrhage. *JAMA* 292: 1823-1830.
247. Tsuruda, J. S., and W. G. Bradley. 1987. MR detection of intracranial calcification: a phantom study. *AJNR Am J Neuroradiol* 8: 1049-1055.
248. Lu, X., Y. Ma, E. Y. Chang, Q. He, A. Searleman, A. von Drygalski, and J. Du. 2018. Simultaneous quantitative susceptibility mapping (QSM) and R2* for high iron concentration quantification with 3D ultrashort echo time sequences: An echo dependence study. *Magn Reson Med* 79: 2315-2322.
249. Expert Panel on MR Safety, E. Kanal, A. J. Barkovich, C. Bell, J. P. Borgstede, W. G. Bradley, Jr., J. W. Froelich, J. R. Gimbel, J. W. Gosbee, E. Kuhni-Kaminski, P. A. Larson, J. W. Lester, Jr., J. Nyenhuis, D. J. Schaefer, E. A. Sebek, J. Weinreb, B. L. Wilkoff, T. O. Woods, L. Lucey, and D. Hernandez. 2013. ACR guidance document on MR safe practices: 2013. *J Magn Reson Imaging* 37: 501-530.

Megan Carol Jacobsen was born in Rochester, Minnesota in 1989, the daughter of William and Vicki Jacobsen. Following her graduation from Rochester Century High School in 2007, she enrolled at Concordia College in Moorhead, Minnesota. She graduated *magna cum laude*, receiving a Bachelor of Arts degree in Honors Physics and Mathematics in May 2011. In August 2012, she entered the Medical Physics program at the University of Texas MD Anderson Cancer Center UTHealth Graduate School of Biomedical Sciences to pursue a Ph.D. Her research interests included developing applications of dual-energy computed tomography. Following her graduate studies, she will be joining the University of Texas MD Anderson Cancer Center's residency fellowship in Imaging Physics.

Permanent Contact Information:

Megan.Jacobsen11@gmail.com